University of Strathclyde

Department of Naval Architecture, Ocean and Marine Engineering

Numerical Investigation of a New Micro-Patterned Surface Inspired by Shark Skin

By

Yansheng Zhang

A thesis presented in fulfilment of the requirements for the degree of Doctor of Philosophy

2019

Declaration

This thesis is the result of the author's original research. It has been composed by the author and has not been previously submitted for examination which has led to the award of a degree.

The copyright belongs to the author under the terms of the United Kingdom Copyright Acts as qualified by University of Strathclyde Regulation 3.50. Due acknowledgement must always be made of the use of any material contained in, or derived from, this thesis.

Signed: *Date:*

Acknowledgements

Firstly, I would like to express my sincere gratitude to my first advisor Prof. Osman Turan for the continuous support of my Ph.D. study and related research, for his patience, motivation, and immense knowledge. His guidance helped me in all the time of research and writing of this thesis. I could not have imagined having a better advisor and mentor for my Ph.D. study. I would like to especially express my appreciation for the opportunities Osman provided for me to get access to the High-performance computing (HPC) for numerical simulations, to be involved in the towing test in Kelvin Hydrodynamics Laboratory, and antifouling test of Catalina in Rhu Marina, without which I would not be possible to conduct this research and improve my academic skills.

Besides my advisor, I would like to thank my elder colleagues for their guidance and all the useful discussions at the beginning stage of my Ph.D. study, which helps me to adjust to the research life from an undergraduate student. A very special gratitude goes out to all my friends who have helped and supported me in so many different ways in the process and to whom I am greatly indebted to.

I am grateful to our last department's postgraduate research administrator, Mrs. Thelma Will, for her kindly advice and support for my administrative problems and also current postgraduate research administrator, Susan Pawson, for her assistance and support. Moreover, I am grateful to the laboratory and technical staff in Kelvin Hydrodynamic Laboratory for their instructions and practical suggestions.

Finally, I would like to express my utmost gratitude and appreciation to my parents: Bo Zhang, Fangqiu Xu, whose strength and determination has always encouraged me. Without their love and support, it would not have been possible for me to complete this research.

Contents

List of Figures

List of Tables

Abstract

Concerning the environmental challenge caused by the shipping industry, particularly diesel exhaust and toxic biocide-based anti-fouling system, the author proposed a new micro-patterned surface as a promising ship coating system, which is inspired by the shark skin surface. The new surface pattern combines the core working pattern of two existing surface technologies: Riblet and Sharklet AF^{TM}, and is expected to possess both drag-reduction and anti-fouling performance.

Computational Fluid Dynamics (CFD) is employed as the main approach in this work to examine the drag-reduction performance of the new surface pattern. The RANS engineering turbulence model, Realizable K-Epsilon Two-Layer (RKE 2L), is used by the author to simulate the new design surface in the turbulent channel flow. The specific RKE 2L turbulence model is firstly used for the drag-reduction investigation of the riblet surface and is validated by a case study of symmetric v-groove riblet surface. The drag-reduction performance of the new surface pattern is directly justified by comparing the skin friction of new surface and reference smooth surface, and indirectly justified by observing the upwards velocity shift in the log layer. Finally, a parametric study is conducted for the new surface pattern to explore the drag-reduction mechanism and the optimization direction.

To understand the riblet coating's practical impact on the full-scale ship, the similarity law scaling method is adjusted and written into the in-house code to extend the drag-reduction results from channel flow scale to full ship length scale. Moreover, a three-step procedure is proposed by the author to provide naval architects a guidance to derive the suitable riblet coating size where maximum riblet drag-reduction performance can be achieved in the most of voyage time. Finally, five real-world case ship types and relevant speed distribution are considered to predict the riblet coating's impact, which is quantified by the drag-reduction percentage and fuel savings.

The author believes that the shark skin inspired micro-patterned surface would pave a basement for the road to new innovative energy efficient approaches for the shipping industry.

Nomenclature

A	Slope of logarithmic velocity law
B_1, B_2, B_3	Intercepts of logarithmic law
B_2'	Derivative of B_2 with respect to $\ln k^+$
B_2''	Derivative of B_2' with respect to $\ln k^+$
$B_{1,s}$	B_1 for smooth surface
C^+	Log law constant
C_F	Coefficient of total resistance
C_{f_smooth}	Coefficient of flat plate resistance
C_{f_riblet}	Coefficient of riblet plate resistance
CV1, CV2, CV3	Control volumes
C_μ	Critical model coefficient
$C_{\epsilon 1}$, $C_{\epsilon 2}$, $C_{\epsilon 3}$, C_M	Model coefficients
D_1, D_2	Velocity profile constants
f_c	Curvature correction factor
f_2, f_μ	Damping factor
G_b	Buoyancy production
G_k	Turbulent production
h	Rib height
h^+	Nondimensional h
I_1, I_2	Integrals of outer law velocity profiles
J_2	Transitional sublayer factors
k, k_1, k_2	Linear parameters defining roughness
k^+	Roughness Reynolds number
L	Characteristic linear dimension
M	Model coefficient
N_x, N_y, N_z	Number of grid points in three different directions
P	Turbulent energy production
P_k, P_ε	Production terms
R	Spanwise spatial correlation

Re	Reynolds number
Re_τ	Reynolds number based on friction velocity
Re_m	Reynolds number based on mean velocity
R_θ	Reynolds number based on momentum thickness
R_x	Reynolds number based on length
R_F	Frictional resistance
s	Rib spacing
s^+	Nondimensional s
S_w	Wetted surface area
S	Mean strain rate tensor
s_k, s_ε	Source terms
t	Time
T_e	Large eddy time scale
T_0	Specific time-scale
T	Turbulent time scale
u	Mean velocity parallel to the wall
u^+	Nondimensional u
U	Velocity at outer edge of boundary layer
U_c	Centreline velocity of the channel
$\overline{U}$	Bulk velocity of channel flow
U_{ship}	Ship velocity
w'	Spanwise velocity fluctuation
W	Mean vorticity tensor
y	Normal distance from the wall
y^+	Nondimensional y
α	Rib angle
α_1, α_2	Velocity profile constant
β_1, β_2	Velocity profile constant
Υ_M	Compressibility modification
δ	Half channel height
δ_ν	Viscous length scale
ε	Energy dissipation rate

θ	Momentum thickness
κ	Von-Karman constant
ν	Kinematic viscosity of the fluid
ρ	Density of the fluid
σ_k, σ_ε	Model coefficients
τ_y	Total shear stress
τ_w	Wall shear stress
η	Kolmogorov length scale
∇	Differential operator
ΔU^+	Roughness function
CFD	Computational Fluid Dynamics
CDP	Controlled Depletion Polymer
DNS	Direct Numerical Simulation
DR%	Drag reduction percentage
EEDI	Energy Efficiency Design Index
FRC	Foul release coating
GHG	Greenhouse Gas
IBM	Immersed Boundary Method
KCS	KRISO container ship
IMO	International Maritime Organisation
LES	Large Eddy Simulation
LNG	Liquefied natural gas
RANS	Reynolds-Averaged Navier-Stokes
RKE 2L	Realizable K-Epsilon Two Layer
SPC	Self Polishing Copolymer
SEEMP	Ship Energy Efficiency Management Plan
TBT	Tributyltin
VITA	Variable Interval Time Averaging
WALE	Wall-adapting local eddy-viscosity

1. Introduction

1.1 Introduction

This chapter introduces the general perspectives of the subjects discussed in this thesis, indicates the motivations behind the work, details research aims and objectives, and outlines the structure of this thesis.

1.2 General Perspectives

Recent UNCTAD analysis (UNCTAD 2018) indicates that global seaborne transportation is currently increasing largely due to the continued growth in world Gross Domestic Product (GDP). As a result of the economic globalisation, the shipping industry has experienced a tremendous boom since the 1950s and plays an irreplaceable role in the global transportation industry today. The advances in technology also have a great impact on the growth of maritime shipping. Containerisation might be regarded as one of the most influential inventions in the 20th century and has revolutionized the shipping industry. The appearance of this technique not only eliminates wasted space that allows ships to carry many times more cargo but more importantly cuts the unloading time and reduce the demand for labour in port. Nowadays, international shipping has become the most important mode of transport and carries almost over 90% freight for the world trade. The world seaborne trade was estimated at 10.7 billion tons for 2018 (UNCTAD 2018). Currently, more than 50,000 merchant ships, which are registered in over 150 nations and manned by over a million seafarers, are sailing at sea every day and transport all sorts of cargoes for different industries (ICS 2018).

Although the seaborne transportation is necessary to enable economic development to occur, the rapid growth in maritime shipping also causes non-ignorable effects to the environment. Two particular aspects of the environmental impact induced by the maritime shipping, ship exhaust and biocide-based antifouling coating, are of the interest of current research study.

Because of the fuel economy, robustness, and operation simplicity, the diesel engine is used as the predominant form of the power unit for most modern cargo ships. However, the diesel exhaust (GHG, SO_x, NO_x, etc.) emitted from the ships should be reduced to avoid the catastrophic impact on the environment and human health. Greenhouse Gas (GHG) emissions are the major contributor to global warming and ships alone accounted for 932 million tonnes CO_2 emissions in 2015 (Olmer, Comer et al. 2017). Other air pollutants like SO_2, NO_x also pose a significant threat to human health and lead to 50,000 premature deaths in Europe in 2012 (EEA 2016). A recent research indicates that the proportion of ship emissions for CO_2, NO_x, and SO_2 are respectively 2-3%, 10-15% and 4-9% out of the global anthropogenic emissions (Endresen 2008). But the serious environmental problem caused by shipping did not receive enough attention until Kyoto Protocol treaty is proposed in 1997 in Japan, which was set up to reduce emissions of six Greenhouse Gases (GHG) (Demirel 2015). Some regulations like Energy Efficiency Design Index (EEDI) (IMO 2014) and the Ship Energy Efficiency Management Plan (SEEMP) (IMO 2012) are published to regulate the world fleet for a more energy-efficient ship design and operation.

After the ban of organotin compound tributyltin (TBT), another environmental concern was raised due to an increased usage of alternative toxic biocide-based antifouling systems. The toxic biocides may cause unknown environmental risks and are thus under strict scrutiny. New legislative frameworks: such as 6th Environmental Action Plan, the EU Water Framework Directive, and the Biocidal Products Criteria, have been published to regulate the use of biocide-based antifouling coating but severe economic and ecological consequences still exist unless new environment-friendly alternatives appear.

To solve the environmental challenge caused by the shipping industry, new energy efficient technologies are needed to reduce the ship exhaust emissions and resist marine biofouling in a non-toxic way. Currently, the energy efficiency is normally improved by voyage operation (reduced speed, weather routine), technical approach (engine, propeller, hull optimization, antifouling), and alternative power (solar or wind energy). In this thesis, the main aim is to assess the feasibility of developing a new biomimetic energy-saving ship coating surface which is inspired by shark skin. The new design surface is inspired by two existing techniques: riblet drag-reduction structure and Sharklet AF^{TM} fouling-control surface pattern. Both will be discussed next. In this study, the attempt has been made to incorporate these two techniques into one and maintain their separate working units in order to reproduce their functions.

Riblet Surface

Riblets are micro-textured surface which reduces the frictional drag in the turbulent boundary layer of various flows. This unique riblet structure captured worldwide attention soon after the NASA Langley Group lead by Walsh published the drag-reduction experimental results in the late 1970s (Walsh and Weinstein 1979). Following research work confirmed as much as 6-8% drag-reduction performance of the riblet structure. Today, the innovative surface technique works well in water, air, and other fluids. It is also widely applied in various fields of use: such as Transport (aviation, shipping), sports (air racing, speedy boats), industrial applications (flywheel, pumps), and wind power (rotor blade).

Sharklet Surface

Inspired by the dermal denticles of shark skin, Sharklet Technology designed the unique Sharklet surface pattern to inhibit bacterial growth. Sharklet surface consists of millions of microscopic surface patterns, each of which is comprised of four different surface features and arranged in a distinct diamond structure. The superior resistance of Sharklet AF^{TM} to microorganisms' attachment indicates a potential physical ship anti-fouling method. A successful alternative non-toxic anti-fouling ship coating not only avoids the unknown environmental risks caused by the use of biocides but also helps to reduce diesel exhaust emissions, fuel and maintenance costs. Biofouling, mentioned as the undesired accumulation of microorganisms, plants, animals on the submerged ship structure, especially ship hull, significantly increases the surface roughness, and thus causes an increasing demand for power up to 80% for a heavily fouled hull to propel the ship at the same speed. Moreover, the cost of maintenance to keep the ship hull coating in a clean condition or acceptable level of fouling (slime fouling) is inevitable for all ship owners. If the entire world fleet is assumed to be in well-coated and smooth hull conditions, the savings in fuel each year will be 66 million tonnes (George 2016). The last concern raised by marine fouling is that it introduces invasive aquatic species to a new environment. The invasive species may survive and reproduce population in the host environment, out-competing native species and finally, multiply into pest proportion. These species are causing devastating effects to biodiversity and the damage to the environment is always irreversible.

Research Method

The commercial Computational Fluid Dynamics (CFD) software – STAR-CCM+ was employed in this thesis to study the newly proposed surface topography, especially in the perspective of drag-reduction performance. A parametric study was carried out for the sake of optimizing the design geometry. Some parameters of interest were monitored by post-processing the CFD results, based on which the surface drag-reduction mechanism is analysed. However, due to the micro-scale pattern of the new surface topography, the order of magnitude of the computational domain is much smaller than that of the full-scale ship. Thus, in the perspective of a naval architect, only the CFD studies of the new design surface is not enough to estimate its impact on full-scale ship’s drag-reduction performance.

As a result, the well-known similarity law scaling method proposed by Granville (1958) was adopted in this thesis and an in-house code was developed to make proper estimates of the drag-reduction surface’s impact on the full-scale ship’s drag-reduction performance. The obtained CFD results and general information of target ship such as ship length and ship speed are used as input. The three-step procedure was proposed in this work to provide an approach that is used to find out the optimum riblet coating size that maximizes its drag-reduction performance. General charts of two representative drag-reduction coating surfaces are presented in order to help a naval architect quickly confirm the rough range of the suitable ship coating size. Moreover, efforts have been made to estimate the drag-reduction performance and fuel consumption of some case ship types by employing the real speed distribution information from the literature.

To sum up, this work proposes a unique surface topography that is supposed to possess drag-reduction and fouling-control potential. The specific surface is investigated by the CFD software to assess its hydrodynamic performance. In the perspective of the practical application, a mathematical model is developed to estimate the effects of the drag-reduction surface on full-scale ships and to find the most suitable coating size for a specific drag-reduction surface. Each main chapter presents a novel study to fill the gaps in the literature and hence make a state-of-the-art contribution to the field.

1.3 Motivations behind this Work

- The worldwide environmental concern raised by diesel exhaust emitted from ocean-going ships leads to the birth of relevant legislative frameworks: such as Energy Efficiency Design Index (EEDI), The Ship Energy Efficiency Management Plan, etc. The enforcement of these regulations requires researchers to develop new innovative ship energy-efficiency approaches. Moreover, the increasing usage of alternative biocide-based antifouling systems after the complete ban of TBT-based marine coatings captured the attention of the governments due to the unknown environmental risks. New non-toxic alternative fouling-control systems are needed because severe economic and ecological consequences may well be caused if no acceptable alternatives exist. To the best of this author's knowledge, no specific fouling-control system combines the technologies of riblet structure and Sharklet AF^{TM} surface pattern. For the newly proposed surface topography in this thesis, the hydrodynamic impact of the modification of fouling-control surface pattern on the traditional symmetric v-groove riblet structure should be studied by carrying out scientific research.

- While using the CFD technique to investigate the drag-reduction performance of the new surface topography, it is important to ensure that the selected turbulence model (RKE 2L) is able to accurately reproduce the drag-reduction performance. A validation test of a classical symmetric v-groove riblet drag-reduction structure is thus necessary for a critical research. To the best of this author's knowledge, no specific CFD study of riblet surface exists to employ

RKE 2L turbulence model to investigate riblet’s drag-reduction property. (Chapter 3)

- It is critical to predict the effects of the new surface topography on the skin friction and also the turbulent activities in the near wall region of the turbulent boundary layer. A parametric study of the new surface topography will be of great help to understand how the modification of the surface geometry affects the drag-reduction performance and would be expected to finally lead to an optimum design conclusion. (Chapter 4)

- Although the CFD technique is a suitable method to predict the hydrodynamic performance of the micro-structured new surface topography, current research work using CFD can only be completed in fairly small-scale computational domain due to the cost of computational resources and computational time. In the perspective of practical use, it is important to be able to predict the impact of the drag-reduction surface on a full-scale target, a new mathematical model based on the CFD results of the drag-reduction surface is expected to be established. (Chapter 5)

- Although the similarity law scaling method is a suitable technique to predict the impact of drag-reduction coating surface on the frictional resistance, the procedure seems to be complex for inexperienced users because of the requirements of numerical methods and understanding of the subject. As a result, drag-reduction surface specific charts would therefore be of great benefit. To the best of this author’s knowledge, no specific drag-reduction surface based general chart exists to predict the rough range of the coating size. (Chapter 5)

1.4 Research Aims and Objectives

The main aim of this thesis is to assess the feasibility of developing a new environmentally benign surface pattern that can both reduce ship frictional resistance and inhibit marine biofouling on the ship hull surface. More detailed objectives are also listed below, which indicates the novelty of this research work.

- To develop a new micro-patterned surface that is expected to possess dual function (drag-reduction and fouling-control).

- To establish a plausible CFD model so that a correct frictional resistance of the target plate of the fully-developed turbulent channel flow can be predicted.

- To examine if the Realizable k-epsilon two-layer (RKE 2L) turbulence model is capable of reproducing the drag-reduction performance of the riblet structure.

- To derive the possible drag-reduction mechanism of the classical symmetric v-groove riblet based on the numerically obtained lower-order turbulent statistics, and to justify the findings with existing riblet drag-reduction mechanism.

- To investigate if the new micro-patterned surface possesses drag-reduction property using CFD techniques.

- To conduct a parametric study of the new design surface so that the impact of geometric variation on the drag-reduction performance and near-wall turbulent activities can be better understood.

- To provide an initial estimate of the optimum new design surface geometry.

- To conduct preliminary investigation on the fouling-control performance of the new micro-patterned surface using results obtained from numerical simulations

- To extend the drag-reduction effect from the small channel flow scale to the full ship length scale by employing the similarity law scaling procedure.

- To provide an approach that determines the optimum drag-reduction coating size so that the peak drag-reduction performance could be attained in the most time of sailing.

- To take the existing yearly speed distribution into account and explore the fuel savings and how the drag-reduction coating will perform in a practical sailing condition for various ship types.

1.5 Structure of the Thesis

The structure of this thesis is summarised in Figure 1.1.

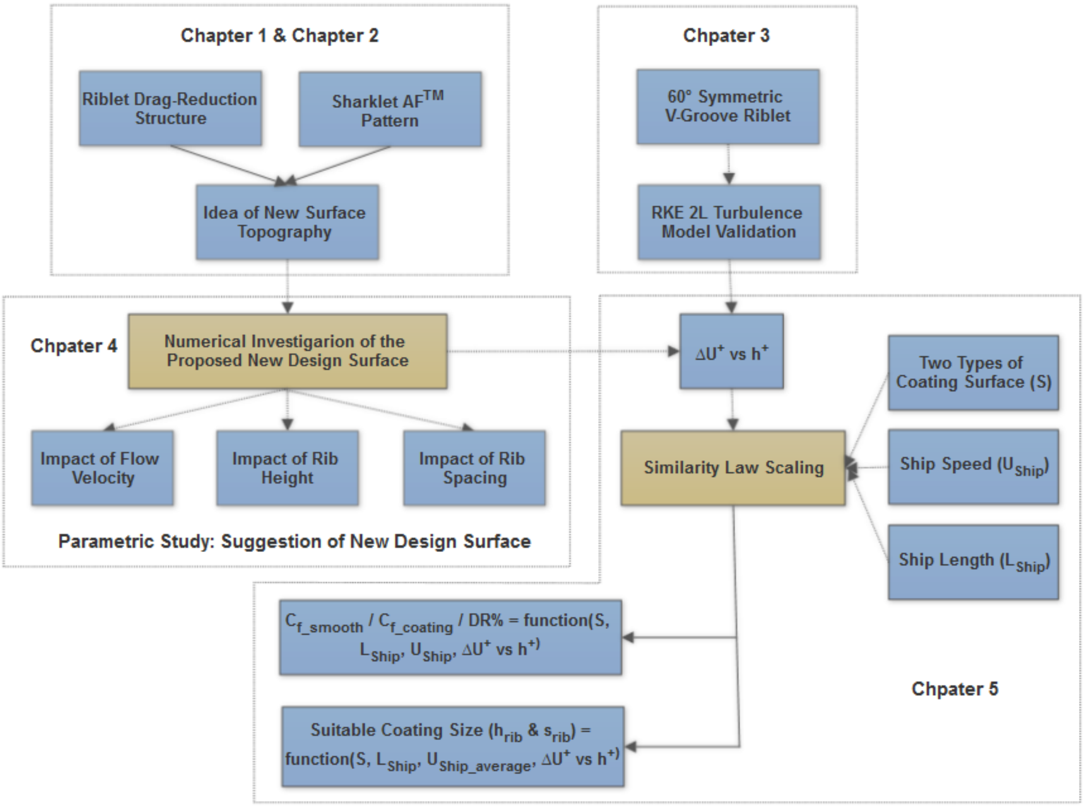

Figure 1.1 Structure of the thesis

- Chapter 2

The literature survey concerning the research topic is presented in this chapter. The research has identified the negative environmental impact of shipping, particularly ship exhaust and biocide-based anti-fouling systems, and current developments in drag-reduction and fouling-control techniques. Shark skin, from which the author got inspiration for the current research, has been introduced in terms of the unique structure and functions. The coherent eddies within the near-wall turbulent boundary layer are introduced to provide more insights into the turbulent environment of current research interest. Finally, two types of surface techniques, riblet drag-reduction surface technology and fouling-control surface technology, are detailed with existing research findings and methods.

- Chapter 3

The validation test of a traditional symmetric v-groove riblet structure was carried out in the fully-developed turbulent channel flow in order to ensure that the selected RKE 2L turbulence model is capable of reflecting the impact of surface topography on the skin friction and near-wall turbulent activities.

- Chapter 4

The new design surface is proposed in this chapter and its hydrodynamic performance is investigated by the validated commercial code for any potential drag-reduction performance. A parametric study with regard to flow velocity, rib height, and rib spacing was conducted to deduce the optimum design of the new surface topography. The impact of the existence of streamwise riblet discontinuity has also been discussed in terms of the drag-reduction performance. Based on the calculated numerical results, the fouling-control performance of new surface is analysed in terms of wall shear stress, which is compared to the smooth surface.

- Chapter 5

The similarity law scaling method was adopted to extend the drag-reduction results from channel scale to full ship length scale. A matching in-house code was developed by the author to achieve automation of numerical calculations. A three-step procedure was proposed to explain the fundamental workflow to derive the optimum drag-reduction coating size for a ship, hypothetically coated with a drag-reduction coating. General charts are presented and expected to serve as a reference dataset to help a naval architect quickly confirm the rough range of a suitable riblet height. Finally, the practical ship speed distribution data of some case ship types is used to predict the two representative coatings' effects on the drag-reduction performance and fuel consumption of a full-scale ship.

- Chapter 6

Following the research aims and objectives proposed at the beginning of the thesis, the achievements and outputs of this research are summarized. The novel contribution of this work in the field of study has also been outlined. The existing difficulties and imperfections throughout the research process are summarized, and recommendations for future work are clarified. The concluding remarks are presented at the end.

1.6 Chapter Summary

The general perspectives, the motivations behind this work, the aims and objectives, and the structure of this thesis were presented in this chapter.

2. Literature Review

2.1 Introduction

Instead of just a routine step taken to fulfil format requirements, the literature review is integral to the whole thesis. The process of the literature review is time-consuming but never stops during the entire Ph.D. period. Consistent investment in scholarly books, research articles, and other relevant sources gradually helped the author to establish a theoretical framework and methodological focus. Through the process of critical thinking, the past work in the field of interest was evaluated, condensed and research direction gradually became clear. Finally, a new research direction, important and needed, is proposed in this thesis to make a contribution to the specific field.

In this chapter, the basic knowledge that is closely connected with the research topic is explained in the following sections. Hereby, a brief organization of the chapter is introduced.

In Section 2.2, the serious environmental impact of two specific ship related problems, diesel exhaust and biocide-based anti-fouling systems, are depicted, and relevant legislative frameworks that have come into force are detailed.

In Section 2.3, a comprehensive introduction of the most recent developments in the fields of the research interest of this thesis, drag-reduction and anti-fouling technique, are given.

In Section 2.4, shark skin, from which the author got the inspiration for the proposed new design surface, is introduced in several perspectives including microstructure of shark skin surface, drag reduction properties, and anti-fouling properties.

In Section 2.5, the basic structure and prominent activities within the near wall turbulent boundary layer are clarified. As a widely-approved unresolved problem in physics, only some of the key features of turbulence is introduced in this section, such as the onset of turbulence, energy cascade, four principle coherent motions that are directly linked to riblet drag-reduction mechanism.

In section 2.6, the cornerstone studies of both riblet structure and fouling-control surface pattern are presented respectively. The significant research findings and main research methods of riblet structure (i.e. experimental and numerical) are reviewed. Several natural and artificial fouling-control surface topographies and theories of fouling-control surface are discussed.

In section 2.7, the concluding remarks of this literature review are listed such that the gaps in the literature are clearly defined.

2.2 Environmental Impact of Ship Exhaust and Anti-Fouling Coatings

Marine Environment Pollution Committee (MEPC), which is IMO’s senior technical body on marine pollution related matters, adopted the first International Convention for the Prevention of Pollution from Ships (MARPOL) in 1973. The anti-pollution convention has been amended many times to adopt a wide range of methods to prevent and control pollution from ships such as oil pollution, atmospheric pollution, sewage, garbage, anti-fouling pollution, and etc.

It should be noted that only atmospheric pollution and antifouling pollution are reviewed here for the interest of this research.

2.2.1 Regulations for Air Pollution from Ships

The diesel exhaust (CO_2, SO_x, NO_x, etc.) generated by burning bunker oil in the marine diesel engines makes a significant contribution to global warming, causes adverse health effects and has been classified by Environmental Protection Agency (EPA) as a likely human carcinogen (EPA 2003). In 1997, a new annex was added to the MARPOL, which aims to minimize airborne emissions from ships and their contribution to local and global air pollution and environmental problems (IMO 2018). Based on the Third IMO GHG Study, approximately 796 million tonnes of CO_2 was emitted in 2012 which is about 2.2% of 2012 total global emissions and this percentage will increase by 50% to 250% by 2050 (IMO 2014). The continuous growing of the international shipping industry and its significant contribution to climate change accelerate the establishment of energy-efficiency regulations to limit the Greenhouse Gas emissions from ships.

With regard to existing energy-efficiency regulations, most of current ships are working on energy-efficiency management plan, some of which focus on improvement of voyage planning, underwater ship components cleaning, and innovative technical solutions. In July 2009, MEPC finalized a package of specific technical and operational reduction measures. In July 2011, the technical and operational measures were firstly made mandatory for all ships irrespective of flag and ownership. In January 2013, regulations such as Energy Efficiency Design Index (EEDI) for new ships and Ship Energy Efficiency Plan (SEEMP) for all ships entered into force and a new chapter entitled Regulations on Energy Efficiency for Ships, was added to Annex VI.

In April 2018, MEPC 72 adopted resolution MEPC.304(72) on Initial IMO Strategy on the reduction of GHG emissions from ships. The Initial Strategy is ambitious and envisages that the total annual GHG emissions will reduce by at least 50% by 2050 compared to 2008.

2.2.2 Environmental Risk of Marine Anti-Fouling Systems

The anti-fouling ship coating, which is an effective tool to keep the ship hull clean and smooth, has been used for thousands of years to help ships travel faster through water and consume less fuel. However, for certain anti-fouling systems, the toxic ingredients released from the biocide-based coating cause detrimental damage to the marine species, habitat, and ecosystem. To some extent, human health is also at risk as a result of the consumption of affected seafood.

As a result, in October 2001, IMO adopted a new international convention entitled International Convention of the Control of Harmful Anti-Fouling Systems on Ships. The new convention will inhibit the use of organotin as ingredients of current antifouling systems and more strict policies will be implemented to scrutinize the use of any potential future use of alternative materials in antifouling systems. The organotin compound tributyltin (TBT) was initially developed by the chemical industry in the 1960s and soon became the most widely used biocide in anti-fouling paints for most seagoing vessels in the 1970s because of its superior anti-fouling performance and less harmful property than the anti-fouling systems at that time: such as DDT and arsenic. (IMO 2002)

However, later environmental studies found that TBT's excellent performance was paid by the sacrifice of the marine environment. The existence and persistence of organotin compounds have been found in the water and sediments which poses threats to marine creatures or even human health by entering the food chain (IMO 2002). The problem caught the attention of the MEPC in 1988, and IMO adopted an Assembly resolution in 1999 that called for a worldwide prohibition on the use of organotin compounds in anti-fouling paints on ships by 1 January 2003, and a complete prohibition by 1 January 2008 (IMO 2018).

It needs to be noted that the increasing application of alternative biocides: such as copper, and accumulation potential of organic biocides may also pose a significant environmental risk. Innovative biocide-free anti-fouling systems are expected to be developed to avoid one harmful substance being replaced with another.

2.3 Energy-Saving Techniques: Drag-Reduction and Anti-Fouling

Driven by the legislative frameworks of ship energy efficiency and anti-fouling systems, new research has been carried out in recent years to satisfy the regulations, and the achievements most relevant to this thesis are detailed in this section.

2.3.1 Drag-Reduction Techniques

The viscous resistance is of great interest to naval architects who design the merchant ships at lower speeds since it is the dominant part of the total resistance. The primary techniques to reduce skin friction of a ship could be categorized into two groups: passive and active, which are summarized in Figure 2.1. The passive methods do not require the addition of mass, momentum or energy into the surrounding water, but some changes to the surface shape, property are typically made to reduce the skin friction. The active methods always require extra space for storage and generation of certain injections, and for some certain techniques, extra energy is needed to propel the injections.

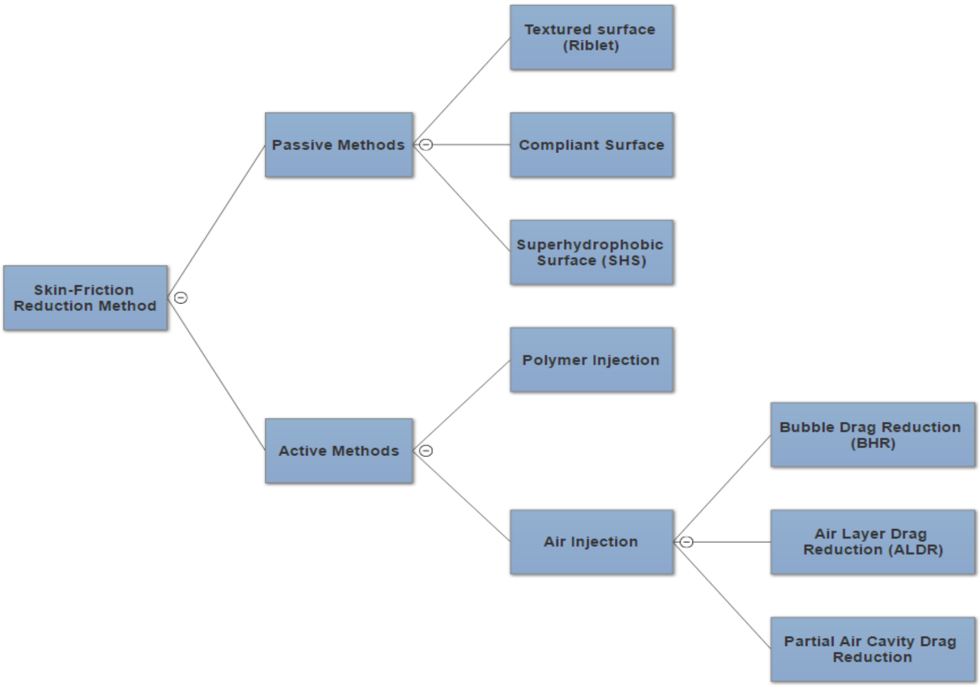

Figure 2.1 Primary skin-friction reduction methods summarized from Perlin, R. Dowling et al. (2016)

It is interesting to indicate that all three passive methods shown above are inspired by creatures: shark skin scales (riblet), dolphins and sharks (compliant surface), and lotus (SHS). Shark skin-inspired riblet structure will be discussed in detail in the following sections. Compliant surfaces work by deforming under the action of the turbulent boundary layer and thus alter the near-wall flow (Perlin, R. Dowling et al. 2016). Superhydrophobic surfaces are generally based on composite materials and works by trapping a certain amount of air above the surface to create boundary slippage and shear-free air-water interface (Guo and Zhou 2013). The drag-reduction property of polymer in the turbulent boundary layer was firstly reported by Toms (1949) and its use in internal flows is well established. However, due to the cost of polymer and its requirements for storage and mixing, its use on external flow has been limited (Perlin, R. Dowling et al. 2016). Instead, air is a preferable alternative that can be injected into the surrounding water to reduce ship frictional resistance and has been applied in three methods: Bubble Drag Reduction, Air Layer Drag Reduction, and Partial Air Cavity Drag Reduction.

2.3.2 Anti-Fouling Systems

After the complete ban of TBT use, the marine anti-fouling technology stepped into the post-TBT era which is under increasingly stringent scrutiny due to the new environmental protection criteria, such as the 6th Environmental Action Plan, the EU Water Framework Directive, and the Biocidal Products Criteria. Therefore, the alternative biocide-based anti-fouling coatings are also not recommended due to the toxicity. At present, there is no overall suitable alternative non-toxic coating technology so that more research needs to be done to fill the technical gap (AMBIO 2010). The recent anti-fouling approaches have been summarized in Figure 2.2.

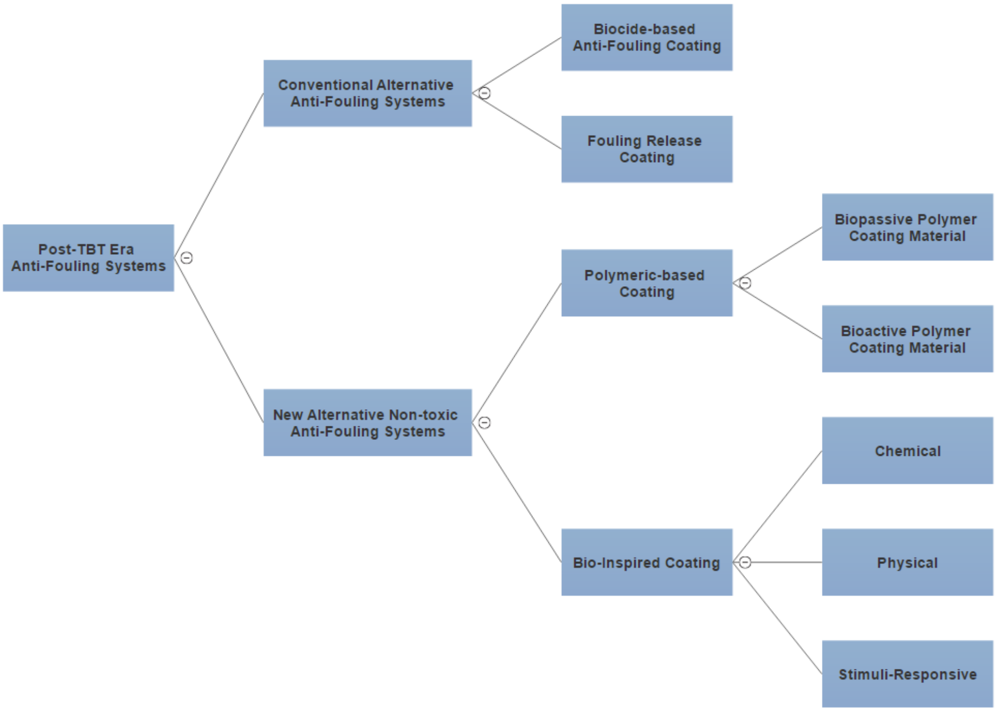

Figure 2.2 Recent fouling-control approaches

Another conventional alternative anti-fouling system is Foul Release Coating (FRC), which functions due to a low surface energy which degrades an organism's ability to generate a strong interfacial bond with the surface. However, certain operational ship speeds (normally larger than 20 knots) and repair difficulty are the main reasons that prevent it to be a universal anti-fouling solution (Chambers, Stokes et al. 2006).

Considering the negative impacts of anti-fouling release systems, such as environmental degradation and bacteria resistance (Martin 2013), new research has been done to develop non-releasing approaches which focus on tethered biocidal agents in polymeric matrix or newly designed polymer structures with anti-fouling properties (Banerjee, Pangule et al. 2011, Charnley, Textor et al. 2011). There are two types of polymeric-based anti-fouling systems: biopassive and bioactive. Benefiting from the hydrophilic well-hydrated polymer coating material, adhesion of bacteria and further microorganism is greatly inhibited by minimizing the absorption of their main nutrient: the protein (Banerjee, Pangule et al. 2011). The polymer that is based on Polyethylene Glycol (PEG) received the most attention because of high inhibition capacity on protein adsorption. However, stability problems, such as oxidative degradation and chain cleavage have been revealed to weaken their resistance ability (Banerjee, Pangule et al. 2011). The bioactive polymer material is actually the covalent attachment of an anti-microbial agent, which functions by killing the microorganisms (Charnley, Textor et al. 2011, Kugel, Stafslien et al. 2011). Among a wide range of biocides or molecules with anti-microbial properties tethered in the substrates, Quaternary Ammonium Compounds (QAC) is the most widely explored due to the unique ability to disrupt the bacterial cell wall (Kugel, Stafslien et al. 2011).

Bio-inspired strategies have led to the creation of a new class of anti-fouling marine coatings and a better understanding of natural fouling defence mechanisms (Kirschner and Brennan 2012). Based on different anti-fouling mechanisms, bio-inspired strategies are divided into three groups: chemical, physical and stimuli-response.

The key to a chemical natural organism defence comes from the production of Natural Product Antifoulants (NPAs) (Chambers, Stokes et al. 2006). Some examples of NPAs are metabolites produced by a wide range of marine organisms, but the limited production amount is the main reason that hampers the development into an industrial scale (Chambers, Stokes et al. 2006). Other examples of NPAs are enzymes and are grouped into four based on the proposed mechanisms as shown in Figure 2.3.

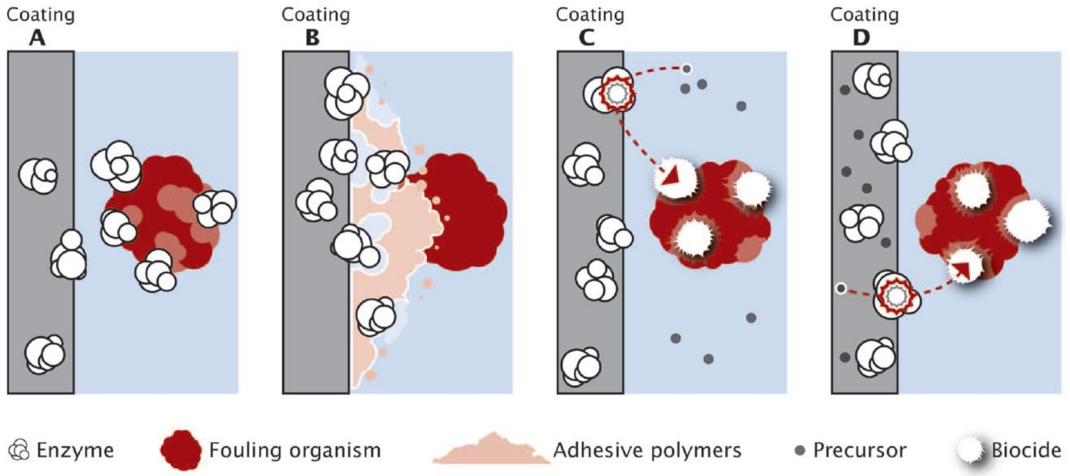

Figure 2.3 Proposed mechanisms of enzymatic antifouling. A = based on direct biocidal antifouling; B = based on adhesive degrading direct antifouling; C = based on indirect antifouling with the substrate in the environment. D = based on indirect antifouling with the substrates provided from the paint. (Olsen, Pedersen et al. 2007)

Direct biocidal enzymatic coating mimics the mechanism of commonly applied biocides actions since the substrate of the enzyme is vital for the survival and wellbeing of the fouling organisms. Adhesive degrading enzymatic coating, many of which are hydrolases and require water for activity, function by preventing settlement or weakening the attachment strength of the newly attached cells or organisms so they are swept away by hydrodynamic forces. For indirect enzymatic coatings, the enzyme is used to provide the biocides actively inhibiting fouling. The difference of two indirect methods is the source of substrates: seawater or coating (Olsen, Pedersen et al. 2007).

As the study of natural anti-fouling strategies goes deeper, researchers realize that natural anti-fouling success is not only achieved by chemical anti-foulants, but also by physical surface textures and topographies that deter marine fouling. Bers and Wahl (2004) conducted an anti-fouling study of epoxy replicas of four different species with a variety of surface textures: the edible crab; the blue mussel; the egg case of the lesser-spotted dogfish; and the brittle star. Experimental results indicated that all these micro-topographies reduced macro/micro-fouling to various extents in field experiments of three to four weeks (Bers and Wahl 2004). Another group of biomimetic topographies is developed from the skin of marine mammals and fishes, like dolphins, whales, and sharks that will be discussed further in Section 2.4, that have specific scales to help it move quickly and efficiently through the water and also resist fouling from its skin (Kirschner and Brennan 2012).

The last bio-inspired anti-fouling system is featured as stimuli-responsive, which is sensitive and adaptive to the surrounding environment or an externally applied stimulus. Self-polishing paints are a bio-inspired solution that exhibits surface renewable similar to pilot whale skin by continuously replenishing a low-energy surface that reduces the adhesion strength of the marine organisms (Kiil, Weinell et al. 2001). Conformal protective coating is another example that mimics the self-renewing pilot whale, the liquid components of these coatings form a viscous layer in response to the PH and salinity of seawater and the skin dissolves after a stable period to remove fouling organisms, which can then be reapplied from a circulatory system near the surface (Ganguli, Mehrotra et al. 2009).

2.4 Inspiration from Sharks

Biomimicry is an approach to the inspiration that will solve human challenges by imitating nature's time-tested patterns and strategies.

Sharks, as one of the oldest species in the world, have evolved to be well adapted to its particular environment after 450 million years' time. Its unique surface microstructure helps it to move faster in the water and effectively resist the colonization of maritime organisms. Two most important techniques covered in this work: riblet structure and anti-fouling pattern by Sharklet AF^{TM} are both inspired by shark skin surface to some extent.

2.4.1 Shark Skin

2.4.1.1 *The General Perspective of the Shark Skin Surface*

The existence of placoid scales are mostly found at the integument of elasmobranch fishes including sharks, skates, and rays (Raschi and Elsom 1986). The unique structure of sharks' placoid scales lead them to be the excellent sea predator that they are today and their main functions could be subdivided into the following four categories as suggested by Reif (1982).

- Protection against injury and abrasion by rocky substrates

Durophagous reef dwellers live on rocky substrate, in reefs, and in caves, with cross-shaped or knob-shaped scales to protect them against abrasion.

- Protection against parasites, epibionts and sometimes predators

Demersal sharks live on sandy and muddy substrate, the squamation often consists of long thorns, and is usually combined with a strong mucus production.

- Drag reduction in fast swimming sharks

Fast off-shore predators have longitudinally aligned ridges on top of the scale crown.

- Providing space for photophores in luminescent sharks

Bio-luminescent mid-water and deep-water sharks have scales which are small thin spines, leaving enough space for the photophores; or they are peculiar scales with concave facets which never erupt through the photophore bearing epidermis

2.4.1.2 *The Microstructure of Shark Skin Surface*

In the late 60s of the 20th century, biologists found a counter-intuitive fact that shark skin is anything but smooth. Subsequent research indicates that shark scales have a characteristic tooth-like micro-structure, called dermal denticles (literally, tiny skin teeth), that cannot be observed by eyes. Normally, shark's dermal denticles consist of a pulp cavity, dentine, and a hard enameloid and are partly embedded in the stratum laxum collagenous layer of the dermis (Lang, Motta et al. 2008). Crowns, the exposed upper part of dermal denticles, are found to overlap with each other and the ridges structure on the crown's surface is aligned with the direction of the water flow. A longitudinal section of a dermal denticle is shown in Figure 2.4 with all biological components depicted.

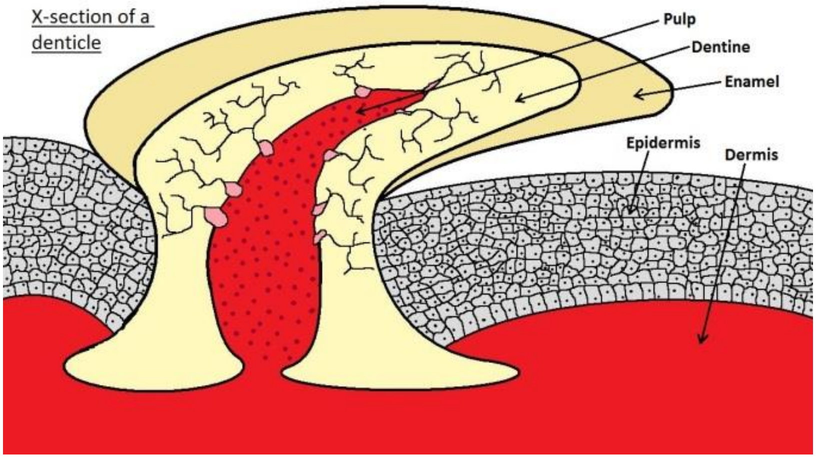

Figure 2.4 Longitudinal section of dermal denticle (Cayman 2015)

Although the basic components of a dermal denticle unit are same, dermal denticles differ a lot from each other in the following aspects: crown shape, crown size, number of ridges, ridge spacing, ridge height, bristle angle. Moreover, the base geometry and size are different interspecifically and ontogenetically at different locations of the body.

2.4.1.3 *Drag-Reduction Property of Dermal-Denticles*

It is hard to clarify how shark scale's hydrodynamic effects are discovered. But the theory of Gary's Paradox might be a possible reason that accelerates the exploration of shark scale's drag reduction function. Gary's paradox generally means the phenomenon that swimming power is not big enough to overcome the sum of many estimated drag values (Webb 1975). As a result, interest for marine creatures such as sharks, dolphins which shows Gary's paradox has been stimulated to investigate if there are any potential drag-reduction mechanisms. The first shark skin related hydrodynamic experiment was carried out by (Johnson 1970), but the result is not that promising. The results indicate that shark has a hydrodynamic drag eight to ten times greater than a dolphin of the same size by towing the dead skins in the tank, which is summarized as the result of the sandpaper-like skin surface by Johnson. There might be several reasons why the incorrect conclusion is drawn by Johnson:

- Improper skin sample; the shark scales vary by different locations and species, the good sample should be taken from fast swimming shark which has finely patterned ridges.

- Improper reference skin; dolphin is also a very unique creature, whose maximum speed could be up to 70 mph. They also possess a special surface structure which might make it possible to keep the flow near to the surface of the body laminar and gives a general reduction of the friction drag by approximately 90% compared to the fully-developed turbulent flow.
- Neglecting the angle of attack; the significance of attack angle lies in their impact to prevent flow separation by producing stronger momentum transfer to increase turbulence (Bechert 1985). Thus, if the angle of attack is not fixed at zero degrees, it might cause a huge increase in skin friction.

Afterwards, Reif (1978, 1982, 1982) and Raschi (1984, 1986) carried out a systematic analysis of placoid scales of various shark species in order to discover the mystery of its unique drag-reduction property.

- Scale size and weight increases ontogenetically on nearly all species.
- Each crown typically possesses from one to eight longitudinally-oriented ridges, or keels. The number of keels varies both interspecifically and ontogenetically.
- The drag reduction type scale is notably lighter and, despite a more closely packed arrangement, results in a substantially lighter integument.
- For the drag-reduction type scale, the dimension of ridging is maintained close to optimal values throughout the individual's ontogeny.

2.4.1.4 Anti-Fouling Property of Shark Skin Surface

The natural surface micro-topographies could always provide an effective physical strategy for anti-fouling coating systems. Based on the analysis of various marine species, Damodaran and Murthy (2016) suggested several key surface parameters that improve anti-fouling characteristics: low fractal dimension, high skewness of roughness and waviness, higher values of anisotropy, lower values point to higher roughness. The multi-function shark skin is regarded as a promising solution to the improvement of seagoing vessel energy efficiency. The microscopic dermal denticles on shark skin not only facilitate its performance in drag reduction, but also in a high efficacy of resisting the attachment, and colonization of microbial organisms from its surface.

The anti-fouling investigation of the real houndshark skin has been conducted by Peng, Lin et al. (2009) with respect to *benthic diatoms* adhesion and *mytilus edulis* attachment. The results showed that after one week's immersion in the seawater with *benthic diatoms,* the *benthic diatoms* adhesion on the dermal denticles of the dead shark skin is much less than that on the bear skin and the adhered benthic diatoms on dermal denticles can be easily washed away in fast-flowing water while the benthic diatoms attached on the bear shark skin cannot be washed away in the same condition. Another anti-fouling test of mussel byssus indicates that the attachment of mussel on shark skin surface is 20 times smaller than that on bear skin, and the byssus coverage on shark skin is only around 5.2% - 7.4% after 96 hours immersion. Experimental observations indicate that although the dimension of dermal denticles and the distance between them seem large enough for the adhesion of benthic diatoms and mussel byssus, this specific shark scale structure could prevent this biofouling greatly. Moreover, Peng indicated that living shark skin has better anti-fouling performance than dead shark skin and concluded this phenomenon as fluid-dynamic reasoning. (Peng, Lin et al. 2009)

Besides the use of real shark skin, researchers also manufactured artificial shark scales to verify the efficiency of a bioinspired surface as an anti-fouling coating. Up to 67% reduction of larvae and spores settlement was observed on soft silicone surfaces with shark scale micro-topographies between 40μm to 200μm in the 3 months' field tests in the North Sea (Meldorf, Germany), which suggests that the combination of the shark scale's flexibility together with surface microstructure leads to a reduction of fouler attachment (Kesel and Liedert 2007). Chen, Zhang et al. (2014) replicated the shark skin surface by rapid UV curable paint and the bio-replicated shark skin exhibits superior anti-fouling performance to the smooth surface after immersing in the open algae pond for 2 weeks. Pu, Li et al. (2016) managed to evaluate the anti-fouling properties of the polydimethylsiloxane (PDMS) surface of biomimetic shark skin by soaking the test surfaces in the Pearl River for approximately 3 months, and the results showed that the adhesion thickness and quantity of algae on biomimetic PDMS surface was smaller than that over the reference smooth surface. Similar to Peng's finding, Pu's result also indicated that there were no residual algae on the surface of biomimetic shark skin after water washing but some residual algae still existed on the smooth surface (Pu, Li et al. 2016).

2.5 Turbulence Boundary Layer Structure

The near-wall turbulent boundary layer is the region, on which riblets impose its impact to perform drag reduction function. As a result, it is essential to clarify the basic structure and prominent activities within this region at the beginning.

Turbulence is widely observed in engineering applications such as internal flow inside the pipe, external flow over moving ships, aircraft and cars. However, it is still a widely-approved unresolved problem in physics. There are pretty a few ways to explain why it is unresolved both physically and mathematically. Hereby, a brief explanation is given here based on the discussion of Won (2013). If a dissipative fluid system is considered, on which initial perturbation is implemented. The state of the system will gradually change and the fluid behaviour will become increasingly irregular and unpredictable when some certain conditions or critical values are reached. Turbulence generally means the similar irregular status of fluid flow, where transition from laminar flow to turbulent flow depends on system-specific constituents and parameters and may give rise to very different states. Currently, no universal physical theory of turbulence has been systematically presented. However, empirical formulas that are valid for certain fluids in a certain range of parameters at low space scales have been proposed. In addition, Navier Stokes equations with a computational cost acceptable extent are used to generate irregular fluid motions that are similar to turbulence.

To understand turbulence, it is necessary to firstly know the onset of turbulence. The incentive of turbulence is relative internal movement due to different velocity. Take pipe flow, for example, the inflow with a certain velocity, U, moves alongside the pipe wall, whose velocity is zero. The margin of two velocities between wall and inflow will be counteracted by the viscosity of the fluid. As a result, Reynolds number, as the guide to determine the relative importance of kinetic energy and viscous damping, could be employed to predict when turbulent flow will occur in a particular situation. The formula is shown as below:

$$Re = \frac{Inertial\ forces}{Viscous\ forces} = \frac{(\rho L^3)\left(\frac{U}{t}\right)}{\mu\left(\frac{U}{L}\right)L^2} = \frac{UL}{\nu} \tag{1}$$

Where

- ρ: density of the fluid
- L: characteristic linear dimension
- U: velocity at outer edge of boundary layer
- t: time
- ν: kinematic viscosity of the fluid

In the 1920s, Lewis F. Richardson proposed that energy transfers from the large scales of motion to small scales, which is normally called energy cascade. The energy cascade description is shown in Figure 2.5.

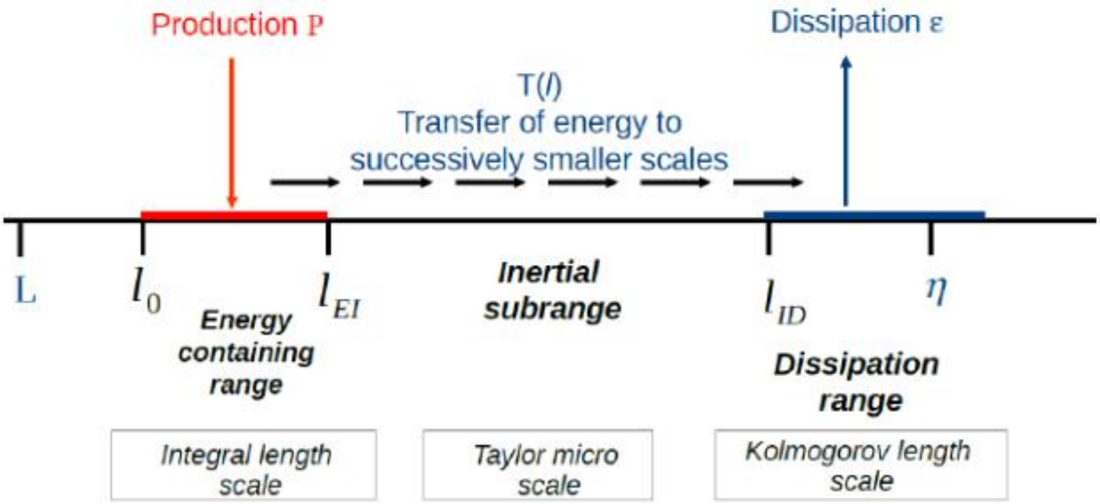

Figure 2.5 Different length scales and ranges in turbulent energy cascade (Saeedipour, Schneiderbauer et al. 2014)

It is known that there are eddies of various scales in the turbulent flow, and could be divided into the following three categories based on their size, as depicted in Figure 2.5:

- Integral length scale
- Taylor length scale
- Kolmogorov length scale

Integral length scale is the largest scales in the energy spectrum. They are carrying most of the energy from the mean flow, which will be transferred to smaller scales. As a result of their large size, the frequency is low and thus integral large scales are highly anisotropic. Taylor length scale is the intermediate between the largest and smallest scales, which is not dissipative but only transfer energy from the largest scales to the smallest. The range is normally called inertial subrange. Kolmogorov length scale is the smallest scales that form the viscous sub-layer range, where energy is imported by nonlinear interactions and also viscous dissipation occurs. In the work of Kolmogorov (1941), he postulated that unlike large-scale eddies that are affected by geometrical and directional information, the statistics of the smallest scales are same for all turbulent flows when Reynolds number is high. In other words, the smallest scales are high frequency and isotropic. As a result, Kolmogorov introduced a new term Kolmogorov length scale as shown below, which is universally and uniquely determined by the kinetic viscosity v and rate of energy dissipation ε.

$$\eta = \left(\frac{\nu^3}{\varepsilon}\right)^{\frac{1}{4}} \tag{2}$$

In terms of the energy cascade, the turbulent flow could be divided into three categories based on their length scale. However, such representations cannot explicitly describe the critical turbulent activities occurring in the boundary layer. Instead, eight most representative coherent behaviours are introduced in the turbulent boundary layer as suggested by Robinson (1991).

- Low-speed streak in the viscous sublayer
- Ejections
- Sweeps
- Vortical structures
- Internal shear layers

- Near-wall pockets
- Backs
- Large-scale motions in the outer layers

The discovery of all these eight types of coherent behaviours above within the turbulent boundary layer is made out of eagerness to understand the physical mechanism behind the facial chaos. The first six coherent behaviours occur in the near wall region ($y+ < 100$), and the last two occur at the outer layer of the boundary layer. The primary coherent motions that are directly relevant to the riblet drag reduction mechanism are the first four motions: low-speed streak, ejections, sweeps, and vortical structures.

Low-speed streak in the viscous sublayer

The first coherent motion is the low-speed streak that is found in the viscous sublayer. Stanford group (Kline and Runstadler 1959, Kline, Reynolds et al. 1967) found that the mean spanwise spacing of low-speed streaks is approximately 100 wall units, and describe that the viscous sublayer consist of both high-speed and low speed fluids that are alternatively elongated. The evidence of low-speed streak in the viscous sublayer breaks the perception that viscous sublayer is almost laminar.

Ejections

The second coherent motion is an ejection. This behaviour always occurs in the buffer layer and is regarded as the main production of turbulence energy together with sweep motions. The significance of these near wall motions is firstly underlined by Laufer (1953), Klebanoff (1954), who obtained statistical quantities of maximum turbulence production, dissipation, diffusion near the edge of the viscous sublayer. Nevertheless, ejection and sweep motions are also observed and respectively described as strong movement of kinetic energy away from the wall and pressure energy towards the wall. Based on substantial research of near-wall region using flow visualization technology and hot film probe, a repeated sequence of motion is observed by Kline, Reynolds et al. (1967), Kim, Kline et al. (1971) as shown in Figure 2.6 and a conceptual description of the mechanism responsible for near-wall turbulence kinetic energy production is established. The conceptual model consists of three stages: (1) low-speed streak craws in the viscous sublayer and gradually moves away from the wall (2) oscillation of streak occurs which forms inflectional streamwise velocity profile (3) flow is suddenly and rapidly ejected into the outer layer.

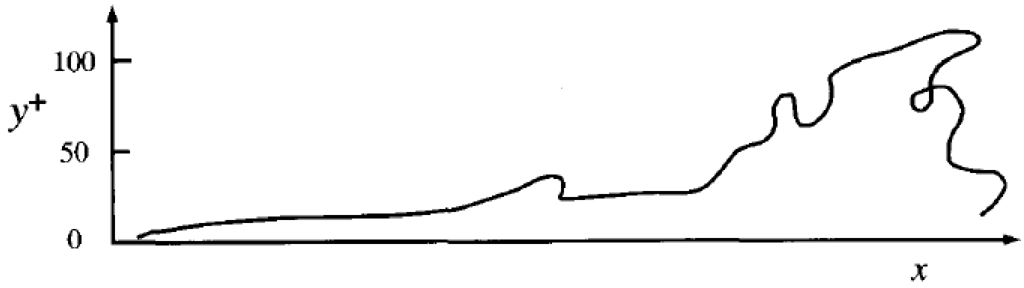

Figure 2.6 A dye streak in a turbulent boundary layer showing the ejection of low-speed near-wall fluid (Kline, Reynolds et al. 1967)

Sweeps

The third coherent motion is a sweep. In terms of the principle of continuity, as low-speed fluid is pumped out of the buffer layer, there should be fluid moving inward from the outside high-speed flow. This inrush fluid is called a sweep. Both ejection and sweep motions could be categorized in the quadrant-splitting technique to account for their contribution to Reynolds shear stress. From the u-v space of velocity fluctuations shown in Figure 2.7, ejection is in quadrant 2 and sweep is in quadrant 4. Both of them produce high positive turbulence energy production since the product uv is negative and $P = -uv\frac{\partial \boldsymbol{U}}{\partial \boldsymbol{y}}$. This is consistent with Grass (1971) that turbulent production is mutual result of both outward ejecting and inward sweeping movements.

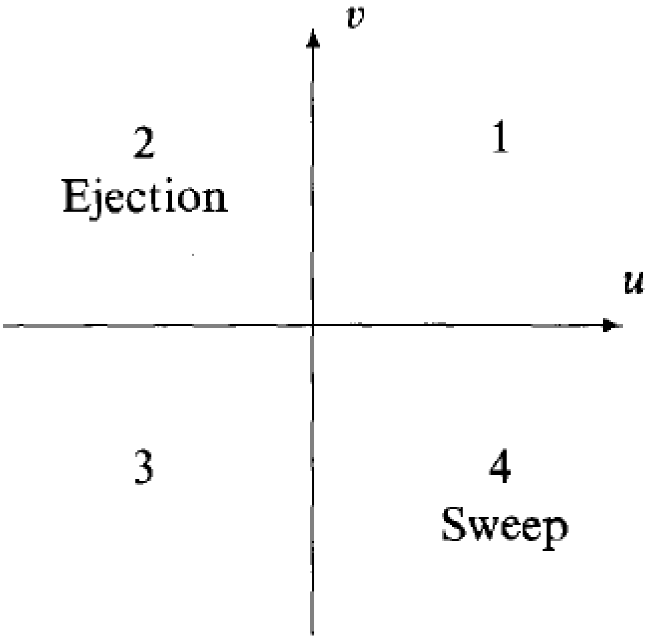

Figure 2.7 The u-v sample space showing the numbering of the four quadrants, and the quadrants corresponding to ejections and sweeps (Pope 2000)

Vortical structures

The fourth coherent motion is vortical structure, which is widely known as loop-like or horseshoes vortical lines. There are streamwise counter-rotating vortices along two legs of the horseshoe's structure, and these streamwise vortices are elongated and mingle as one at a further downstream location. It is suggested by Hinze (1975), Pope (2000) that the vortical structure is responsible for the ejection process of the low-speed streak. The fluid between the rolls, as shown in Figure 2.8, is moving away form the wall and has a relatively smaller axial speed, which is unstable and very likely to be associated with bursting movements (Pope 2000). Hinze (1975) also suggests the instability of the lifted low-speed streak lying in between a pair of counter-rotating vortices. Nevertheless, Hinze (1975) conjectures that the commencement of sweep motion is a joint result of tip vortical movement near the downstream region and the pressure waves generated due to instant vortex/shear-layer breakdown.

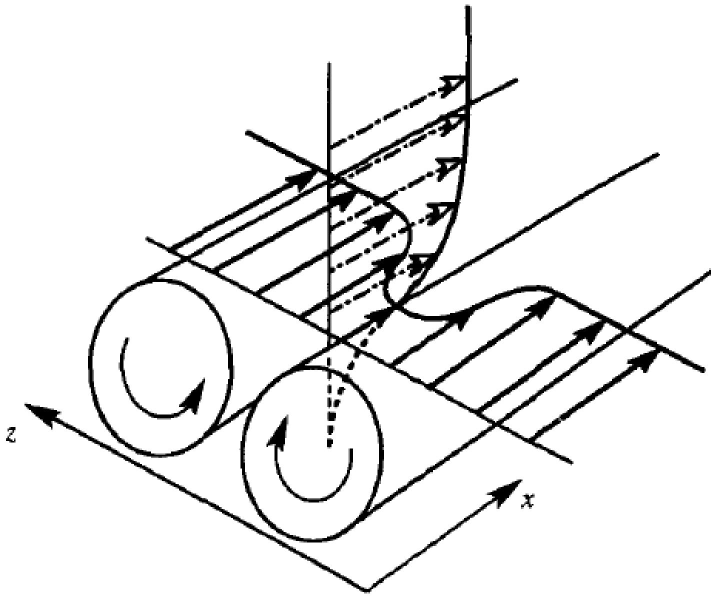

Figure 2.8 A sketch of counter-rotating rolls in the near wall region (Pope 2000)

2.6 Cornerstone Study of the solution

Motivated by the expectancy of developing a new technical solution for ship energy efficiency, the cornerstone study of existing work has been reviewed here that includes two fields of interest: riblet drag-reduction surface, and fouling-control surface pattern.

2.6.1 Riblet

2.6.1.1 *Discovery*

Kramer(1937) may well be the first person who connects the riblet structure and drag-reduction performance in his German patent entitled Device for the Reduction of Friction Drag. The patent suggested that the existence of fine narrowly-spaced wires would delay the flow transition from laminar to turbulent and thus reduce frictional drag because the near-wall turbulent production activities will be weakened, if the wires are mounted in the direction of the flow (Kramer 1961). Unfortunately, his research is discontinued as a result of the Second World War.

Not too much attention was paid to the riblet technology until the 1970s. Walsh et al. (1979, 1980, 1982, 1983, 1984) proposed that longitudinally ridge structure could modify the near wall turbulent structure, which inhibits the growth of the low-speed streak, eliminate the momentum transfer, and thus reduce the skin friction. At almost the same time, Reif (1978) speculated that the ridges on the scales of fast-swimming shark skin surface could reduce drag as it might stabilize the laminar or turbulent boundary layer. Since these initial works, riblet research has developed into a worldwide turbulence-control effort. To some extent, the popularity of riblet research is due to the development of near-wall turbulent structure knowledge and biological investigation of fast-swimming shark skin scales' features.

2.6.1.2 *Methods of Riblet Study*

Since the drag reduction property of riblet structure was discovered in the 1970s, the study of riblet structure became a world-wide topic. The aspiration to explore the cause of drag reduction performance drives people to apply various methods to investigate the mechanism behind the physical structure. Generally, it could be divided into stages:

- Experimental: Flow visualization techniques like dye injection and hydrogen bubble are applied to see how the near wall flow is affected by riblets; Conditional sampling and correlations (e.g. with regards to skewness, flatness) are used to analyze the modification of near-wall turbulent structure like burst frequency, Reynolds stress, turbulence intensity with the help of velocity detection facilities (e.g. with regards to laser Doppler anemometer, hot-wire film, *VITA*)

- Numerical: With the development of computational technology, it is possible to employ Direct Numerical Simulation (DNS), Large Eddy Simulation (LES), and Reynolds-Averaged Navier-Stokes (RANS) simulation methods to model the fully developed turbulent channel to investigate the effects of riblets on the near wall turbulent structure. However, because of the interest of the study focusing on the near wall region ($y^+<100$), the requirement of pretty fine mesh dramatically increase the computational cost of such simulations which demands the use of periodic boundary conditions in the streamwise and spanwise directions, and modelling of simple geometry.

In the following sections, a detailed summary of the main achievements in the field of experimental and numerical investigations is given.

2.6.1.3 *Experimental Studies of Riblet*

Some of the most frequently used measurement and analysis methods are explained here which are skin friction measurement approach, flow visualization approach, and statistical analysis of the near-wall turbulence.

Skin Friction Measurement Approach

Most of the experimental studies of riblet structure are carried out in the wind tunnel or water channel using a sample plate covered with riblet film. As the drag reduction percentage is rather small with no more than 10%, it has a fairly high requirement for measurement approach and machined riblet surface.

To promise a good quality of the result, two primary methods of measurement are used: drag balance and momentum thickness difference.

The drag balance method is mostly used for the wind tunnel test ((Walsh 1982, Walsh and Lindemann 1984, Bechert 1985, Wilkinson S. P. and Lazos 1988) but the result is also affected by the misalignment errors. The other method – momentum thickness difference, is to integrate the boundary layer velocity profile to obtain the momentum thickness, and the change in the momentum thickness is then related to the skin friction. This method is widely used as well ((Gallagher and Thomas 1984, Bacher and Smith 1985, Reidy 1987). However, all the riblet studies that use the change in momentum thickness to determine the drag performance assume zero pressure gradient and zero crossflows. If these two parameters are not negligible, the estimate of riblet thickness changes may be in error.

Concerning the machined riblet surface, the symmetric v-groove riblet structure manufactured by *3M* Company can provide high-quality test films of various sizes. Other riblet geometries like scalloped, blade, and three-dimensional segmented riblets have also been manufactured and tested to examine the drag reduction performance, which are shown in Figure 2.9.

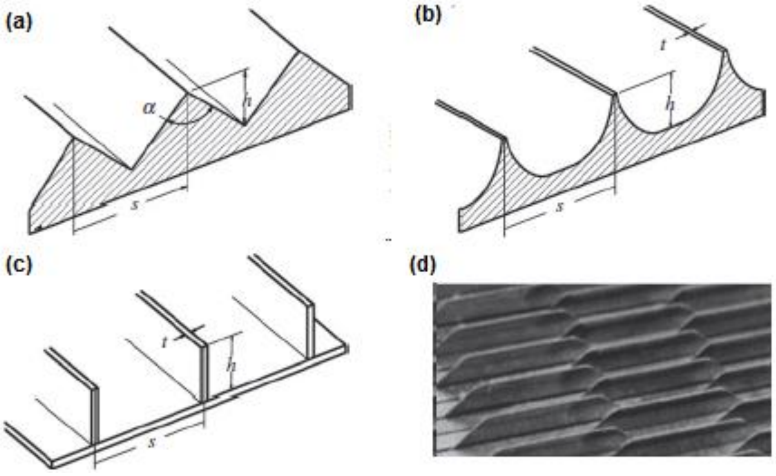

Figure 2.9 (a) Symmetric v-groove riblet (b) Scalloped riblet (c) Blade riblet (d) 3D segmented riblet (Dean and Bhushan 2010)

Flow Visualization Approach

The most direct method to investigate the mechanism of the riblet drag reduction performance might be the flow visualization method. With the help of approaches like dye injection and hydrogen bubble technologies, it is possible to observe how the near wall turbulent structure has been affected by the existence of riblets. Numerous studies (Hooshmand, Youngs et al. 1983, Wallace 1983, Gallagher and Thomas 1984, Bacher and Smith 1985, Anselmet, Fulachier et al. 1986, Savill 1986) have been done in this field, and hereby the widely recognized conclusions are summarized below:

- Lateral motions of the flow are reduced
- The flow in the riblet valley is moving slowly, with low skin friction within the grooves compared to that of smooth surface
- The change in the flow structure is limited to the near wall or sublayer region (y^+<15), the flow in the outer part of the boundary layer remain unaltered.

From the visualization studies, it is found that the near wall turbulent boundary layer of the riblet surface is different from that of a smooth surface.

Statistical Analysis of the Near-Wall Turbulence

In order to understand the mechanism in a more systematic way, some mathematical methods such as skewness, flatness, VITA technology, conditional averaging and correlations are introduced to analyze the near wall turbulent activities of riblet and smooth surface.

- Skewness & Flatness

Skewness is the third moment of velocity fluctuation, and also is symmetry of a signal or the preferred fluctuations of the velocity. Flatness is the fourth moment of velocity fluctuation and indicates the degree of intermittency. In the near wall region, both large positive skewness value and large flatness value are expected. Large positive skewness indicates that the velocity is generally less than the mean, with occasional large excursions to values greater than the mean, which represent the intermittent sweeps of high-speed fluid moving towards the wall. Large flatness indicates short periods of a large deviation from the mean. As the intermittency increases, the flatness factor increases and is thus expected in the near wall region as well.

The data of Pulles (1988), Hooshmand, Youngs et al. (1983), Bacher and Smith (1985) indicate that although the turbulent intensity is reduced, the riblets have no effect on the streamwise fluctuation physics when the riblets are producing drag reductions as indicated by skewness and flatness measurements. A similar result is obtained that the vertical velocity fluctuation has no change regarding skewness and flatness value by Hooshmand (1985) and Pulles (1988). The only difference is in the measurement of the spanwise velocity fluctuation *w'*. Although the skewness of spanwise velocity fluctuation does not change, the flatness of that does increase over the riblets. The data(Wallace 1983, Hooshmand 1985) indicates that the large spanwise fluctuations in *w'* are more intermittent for the riblet surface. This *w'* dampening was also seen in flow visualization as reduced lateral motions of low-speed streaks.

- *VITA* Technique & Conditional Averaging

VITA technique has been the primary method to investigate the burst frequency by quite a few researchers (Walsh 1982, Hooshmand, Youngs et al. 1983, Gallagher and Thomas 1984, Pulles 1988). However, the accuracy of this technique is not so reliable because of the uncertainties of the friction velocity. Hooshmand, Youngs et al. (1983) concluded that *VITA* technique is not appropriate for the determination of burst frequency over the riblets since the obtained result would exhibit either large increase or decrease in the burst frequency based on the friction velocity selected. Afterwards, the problem of friction velocity uncertainty is solved by representing the value of interest (like non-dimensional skin friction, wall distance) with outer flow properties like momentum thickness and free stream velocity. To some extent, the uncertainty is reduced but the result is still dependent on the Reynolds number. To sum up, all the data mentioned above except Gallagher and Thomas (1984) indicate little or no change of burst frequency decrease, only Gallagher and Thomas (1984) report almost 30% decrease of burst frequency.

Conditional averaging of the velocity field is a good means to detect events of bursting that gives more information. Hooshmand, Youngs et al. (1983), Bacher and Smith (1985) and Pulles (1988) have examined conditional averages of the streamwise velocity during a burst. Choi (1989) has done the conditional averaging of skin friction. The work of velocity field conditional averaging indicates that there is no big difference between the smooth and riblet surface except for several small changes. Hooshmand, Youngs et al. (1983) indicated that in the near wall region a suppression of negative fluctuations exists and this may imply a reduction of ejections. They also discovered a small phase shift at y^+=14.7. Bacher and Smith (1985) observed small oscillations and explain it as the streak oscillation that occurs during the bursting process before it lifts off the surface. The biggest achievement in the field of conditional averaging is attributed to the work of Choi, Gadd et al. (1989), who conduct the skin friction conditional averaging with a clear reduction trend.

- Correlation

Compared to burst-detection technology such as *VITA*, correlations have the advantage over *VITA* technique of not depending on threshold levels (Gallagher and Thomas 1984). Even though correlations do not provide information on burst frequencies, but a stronger correlation indicates that a larger number of events have occurred. Triple correlations measured by Gallagher and Thomas (1984) indicates smaller negative correlations over the riblet for y^+<30 while the correlations are same for smooth and riblet surface when y^+=45. Gallagher and Thomas (1984) pointed out that there is a 15-30% increase in correlation length for spanwise spatial correlations R at y^+=15, which is related to the decrease in burst frequency. Moreover, the polymer drag reduction experiment by Fortuna and Hanratty (1972) also indicate an increase in the spanwise scales in the spanwise correlation coefficient of the streamwise velocity gradient.

2.6.1.4 *Numerical Studies of Riblets*

Although significant effort has been made to improve the understanding of the riblet structure in the turbulent channel flow experimentally, there has been no clear conclusion on the lower-order and higher-order statistics of the turbulent flow especially in the vicinity of the wall. Even the channel is simplified to purely flat plane channel flow, there are still disagreements over the turbulent statistics in the experimental studies. Part of the discrepancy might be due to the wide range of Reynolds number in these experiments, but the primary cause of this scatter might be caused by experimental uncertainty, like friction velocity uncertainty referred to in *VITA* technology, involved in measuring turbulence quantities in the near wall region, where relatively high shear occurs and small scales of turbulent motions exist. Thus, the use of numerical simulation to investigate the turbulent channel flow might be a good way to complement experimental data by providing three-dimensional data of velocity and pressure at any point of interest as long as the mesh cell is small enough.

The numerical study of riblet structure has been done in both laminar and turbulent channel flow. For the fully developed turbulent channel, *DNS*, *LES*, *RANS* and even mixing length and one equation turbulence modelling are used to investigate the near wall structure in the turbulent boundary layer. The details of the achievements and conflictions will be outlined here.

Early Stage Study

The early numerical studies of riblet structure employ the mixing-length hypothesis and one equation turbulence model by Khan (1986), Benhalilou, Anselmet et al. (1991), Djenidi, Squire et al. (1991), Li (1992). Khan (1986) might be the first to carry out the numerical computation of riblet structure, which study the turbulent and laminar flow over the v-groove surface at various Reynolds number and riblet sizes. It is concluded that the turbulent flows are accompanied by Prandtl's second kind secondary flows, which form two vortices inside the groove and provide a feedback to the streamwise velocity profile and thereby help viscous forces in reducing the momentum of the fluid inside the groove. However, Khan's conclusion and other's work conducted by one equation model is not widely admitted as it is thought that these models can never provide a way of predicting drag reduction, for arbitrary choice have to be made, or at least choices unrelated to the flow's physics on how to interpret, in the vicinity of the riblet.

Reynolds-Averaged Navier Stokes (RANS) Simulation

Riblet study using RANS turbulence model was mostly carried out by Djenidi, Squire et al. (1991), Djenidi and Antonia (1993), Launder and Li (1993). Djenidi and Antonia (1993) attempted to adapt an already existing k-ε model proposed by Chien (1982) for the calculation of a turbulent boundary layer over a riblet wall. Results from Djenidi and Antonia (1992) showed that the Reynolds shear stress and mean turbulent kinetic energy fit well with experimental measurements, but the drag reduction is significantly underestimated and the return to *2D* as the wall distance increases is not reproduced accurately. Djenidi concluded the imperfect phenomenon as a result of the incorrect use of damping factor ($f_\mu = 1 - e^{(-0.0115y+)}$) because the damping factor introduces the near wall effects by including non-dimensional wall distance y^+, which is associated with friction velocity. Within the grooves, friction velocity is not constant and varies significantly along the groove contour, which is not appropriate to represent the damping effects. Instead, Djenidi proposed to replace f_μ with $\overline{v^2}/k$ since the damping effect on $\overline{uv}$ as the wall is approached is mainly due to the damping of $\overline{v^2}$ rather than to the viscous effect (Launder and Tselepidakis 1990).

Different from Djenidi's work, Launder and Li (1993) doesn't adopt the turbulent viscosity suggested by Chien (1982) which introduce non-dimensional forms of distance into damping function to make the turbulent kinetic energy and shear stress fall to zero sufficiently rapidly as the wall is approached. Instead, the classical isotropic turbulent viscosity model was applied to approximate the turbulent stresses proposed by Launder and Sharma (1974) while the proximity to the wall is sensed only through the local value of turbulent Reynolds number. The obtained results indicate a broadly correct drag reduction level, but there also exist two shortcomings: too little drag reduction achieved below h^+=10 and too large drag reduction obtained above h^+=15.

The possible cause of above imperfections is concluded as an insufficient sensitivity to x-direction inhomogeneous on the level of dissipation and the use of an isotropic viscosity formulation that suppress secondary motions. To solve the second problem, second momentum closure is introduced in the region above the blade riblet tips in place of the eddy viscosity model. The use of this model produces a secondary vortex on either side of the riblet that sweeps high momentum fluid down near the riblet surface thus raising drag around 3%, which does help to make the result more accurate.

In summary, *RANS* modelling of turbulent channel flow could provide an acceptable level of accuracy for the riblet drag reduction problem but still cannot be fully trusted as it cannot completely reproduce all the turbulent structure in the near wall region with the use of isotropic viscosity model. More studies are expected to be done in the future to offer an appropriate and reliable *RANS* model used for riblet channel flow problem for the industrial use.

Large Eddy Simulation (LES)

The idea of *LES* might stem from two aspects: great variability of the large-scale turbulent structure and the almost isotropic, universal character of turbulent flow at small-scale. The first work of *LES* is proposed by Deardorff (1970), whose work uses only 6720 grid points and is able to predict a few features of turbulent channel flow. The result indicates the potential of *LES* for basic studies of turbulence and encourages more efforts in this field. Subsequently, Schumann (1975) carried out a turbulent channel flow with up to 10 times as many grid points as Deardorff and implemented an improved Sub-Grid Scale (SGS) model. However, all these research works have the same problem that not enough attention is paid to the near-wall region of the turbulent boundary layer. And this region is where almost half of the turbulent kinetic energy is produced. Thus, Moin, Reynolds et al. (1978) started the first numerical simulation of turbulent channel flow that computed rather than modelled the near wall flow, which positively indicates some of the well-formed features of the flow in the intermediate of the wall region. This made *LES* method become an effective supplementary tool to study turbulent flow and also encouraged a following more detailed study of *LES* by Moin and Kim (1982).

Generally, *LES* modelling of turbulent flow over the riblet surface in the channel indicates a relatively good fit with experimental results. Yulia Peet, Pierre Sagaut et al. (2007) employed the Code_Saturne (2004) to carry out turbulent channel flow with straight v-groove to prove the validity of *LES* modelling of riblet study. Computational turbulent statistics are compared with Choi, Moin et al. (1993) and a good quantitative agreement is reached for the Smagorinsky model with wall functions. Following the work of Yulia, Mohsen Jahanmiri and Bahraini (2015) also tested the *LES* ability to investigate triangular riblet covered turbulent channel flow by a commercial software – *ANSYS FLUENT*. Differently, they use a new *SGS* model – *WALE* to model the small-scale turbulence and the relatively good result is obtained compared to Choi, Moin et al. (1993).

Direct Numerical Simulation (DNS)

DNS is the most accurate method to investigate the effect of riblet structure on the turbulent near wall region with no compromise like *RANS* and *LES*. *DNS* could produce instantaneous field data without averaging process, and also all scales of interest could be calculated instead of sub-grid scale modelling used in *LES*. As a result, this is the most frequently used method to study the riblet structure effects. However, the only problem of *DNS* is its huge demand for computational resources and only simple geometry under low Reynolds number problems could be solved by *DNS*. It is estimated by Ferziger and Peric (2002) that 512^3 ($\sim 1.35 * 10^8$) or more grid points are needed for DNS simulation of any homogeneous turbulent flow, channel flow, free shear flow, etc. To make the computational cost more clear, the fine mesh refinement of current RANS research work of the new design surface is chosen for comparison, which is shown in Table 2.1.

Table 2.1 Computational cost of turbulent channel flow study by RANS and DNS

Turbulence Model	No. of Mesh Cells	Computational Time (days)	Total Core (hours)	Cost (£)
RANS (Current RKE-2L study)	3.76×10^6	1.5 - 2	768 – 1158	23-35
DNS (Ferziger and Peric 2002)	1.35×10^8	54 – 72	27552 - 41376	827-1241

Notes: 1 core hour will cost £0.03 inc VAT for external users; 24 cores are taken for a current single RANS simulation and 48 cores are assumed for a single DNS simulation; The current estimate is only valid for the simulation conducted in ARCHIE WeSt.

Considering a CFD simulation of turbulent channel flow, DNS study requires roughly 36 times the mesh cells of RANS study, and thus 36 times the total core hours. Hereby, 48 cores are assumed for a single DNS simulation and are estimated to take 54-72 days and cost £827-1241 per simulation, which is both financially and time expensive. In the reality, a lot more computer cores will be used for the computational work of DNS but it must be pointed out that the computational efficiency is not linearly associated with the number of computer cores as shown in Figure 2.10.

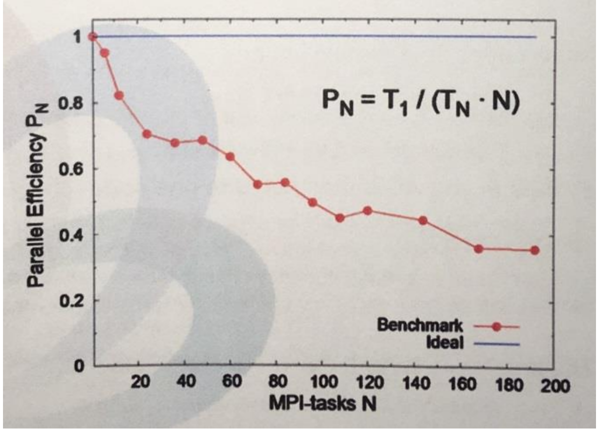

Figure 2.10 Computational efficiency of ARCHIE WeSt (Martin 2018)

As shown above, when the number of computer cores exceeds 120, the parallel efficiency drops to approximately 40% and any simulation that uses more than 120 cores is not recommended. As indicated by Ferziger and Peric (2002), although DNS provides very detailed information about the target flow, the statistisc generated is more than enough for most engineers. In other words, DNS is not cost-effective or suitable to be used as a design tool for the industry. Instead, the engineering RANS turbulence model, RKE 2L, is a suitable alternative to conduct preliminary investigations of the new drag-reduction surface with both acceptable accuracy and computational cost.

Some researchers made an attempt to simplify the governing equations like Chu, Henderson et al. (1992), Chu and Karniadakis (1993). By considering only the flow whose mean velocity remains constant in the streamwise direction and varies arbitrarily in the cross plane, the Navier-Stokes equation is simplified since the only instantaneous flow is 3D and geometry is only *2D*. Generally, DNS for riblets can be divided into two categories: finite methods and spectral methods. Choi, Moin et al.

(1993) employed the finite volume method to study flow over sawtooth riblet. Goldstein, Handler et al. (1995), Chu, Henderson et al. (1992), Chu and Karniadakis (1993) employed a spectral element-Fourier approach to study laminar, transitional and turbulent flow over riblets. It is necessary to mention a popular technique called Immersed Boundary Method (*IBM*) was used to model a riblet covered surface on one wall of a channel bounding fully developed turbulent flow by quite a few researchers including Goldstein, Handler et al. (1995), Goldstein and Tuan (1998), Horsten (2005), and El-Samni, Chun et al. (2007). One unique feature of *IBM* is that no efforts of coordinate transformation need to be made to solve problems with complex geometries in Cartesian based domains. The principle of IBM is that body forces are imposed on the set of grid points at or inside the body surface, which realizes zero fluid velocity boundary condition at the points coinciding with surface locations (El-Samni, Chun et al. 2007).

2.6.2 Fouling-Control Surface Pattern

In terms of marine biofouling, many efforts have been made to study surface chemistry including low surface energy and super-hydrophobic material, which contribute to the effective control of the settlement and adhesion of marine fouling organisms. However, the potential fouling-control benefits that might be brought by surface pattern may not have received enough attention. The micro-topography of surface pattern is closely associated with the attachment process of maritime organisms. Surface topography with suitable scale and texture is very likely to inhibit the colonization of marine micro- and macro-organisms as found in the marine plants and animals such as sharks, crabs, mussels, dogfish eggs, brittle stars, and etc.

Despite the fact that marine organisms span numerous length scales as shown in Figure 2.11, the natural biofouling defence systems discovered from marine creatures always provide the researchers insights into possible biomimetic fouling-control surface topography. Some examples are presented here. The skin of pilot whale (*Globicephala melas*) has an average nanorough surface characterized by a pattern of nanoridge-enclosed pores (average pore size ~0.2 μm^2), which improves its hydrodynamic efficiency and health status by preventing most biofouling organisms from attaching (Baum, Meyer et al. 2002). The shell of the blue mussel *M. galloprovincialis* has a homogeneous ripple like micro-patterned surface (1-2µm) and shows strong fouling deterrence performance (Bers and Wahl 2004). The surface topography of *C. pagurus* effectively resisted macro-fouler, and the surface topography of the eggcase of *Scyliorhinus canicula* and *O. texturata* deters the attachment of micro-fouler (Bers and Wahl 2004).

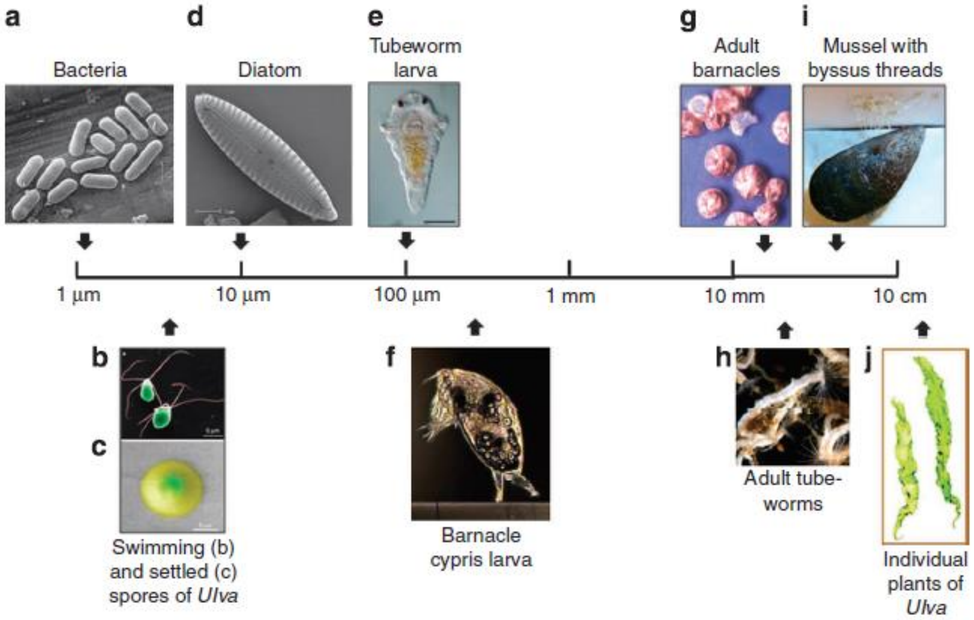

Figure 2.11 Diversity and size scales of a range of representative fouling organisms (Callow and Callow 2011)

2.6.2.1 *Current Artificial Fouling-Control Surface Topography*

Inspired by the unique surface pattern found on the maritime creatures, biomimetic approaches are used and expected to reproduce the fouling deterrence performance that could solve the engineering problems caused by biofouling on medical devices, ships, underwater structures, water treatment systems, food industries, and etc. As a result, some artificial fouling-control surface technologies have been proposed nowadays and they can generally be divided into two groups, which are fine surface topography and coarse surface topography, based on respective species-specific performances.

Fine Surface Topography (Bacteria, Spores of Ulva, Diatom)

- Hierarchical surface topography inspired by rice leaves

Concerning the fact that rice plants thrive in humid and marshy, its specific hierarchical surface topography may effectively inhibit fouling and ensure a normal process of photosynthesis. The conceptual surface topography of rice leaf, engineered hierarchical surface, and SEM image of engineered surface topography are respectively shown below in Figure 2.12.

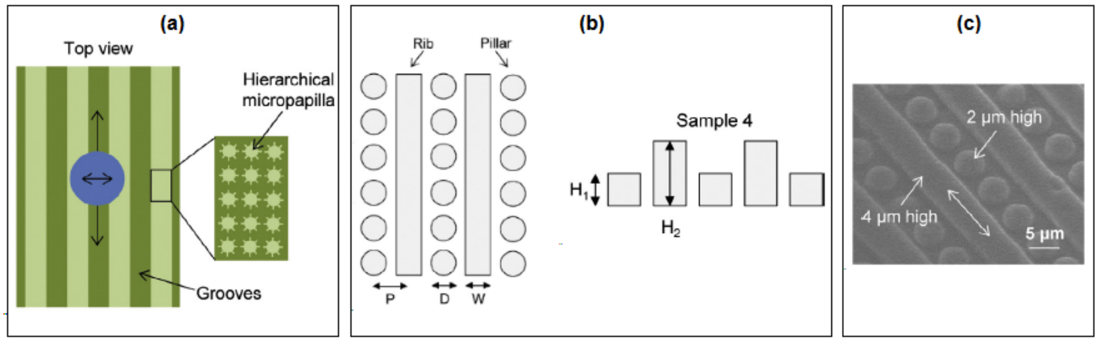

Figure 2.12 (a) Conceptual rice leaf hierarchical surface topography (b) Conceptual model of engineered hierarchical surface (c) Scanning Electron Microscopy (SEM) image of engineered hierarchical surface (Bixler, Theiss et al. 2014)

The hierarchical surface structure of rice is expected to provide the anisotropic flow, super-hydrophobicity, and low adhesion characters. Anisotropic flow is attained by longitudinal grooves with a transverse sinusoidal pattern. Super- hydrophobicity and low adhesion is achieved by the minor surface roughness of micro-papillae superimposed by epicuticular waxy nanobumps. Bioassay experiments have been conducted to understand the antifouling effectiveness of the proposed surface topography. The greatest antifouling performance is observed for the engineered hierarchical surface, as shown in Figure 2.12 with a 33% reduction of *E. coli* coverage at 1/100 concentration (Bixler, Theiss et al. 2014). It needs to be pointed out that the rib's width scale (5µm) of the engineered surface topography is much smaller than that of actual rice leaves' rib width (~160µm). The existence of the rib in engineered surface topography does improve the antifouling performance of the surface compared to that only with pillars. On the other hand, it is unlikely to deduce that the single rib width scale of 5µm may contribute a lot to the antifouling performance of macro-fouler.

- Sharklet AF^{TM} surface technology inspired by shark skin

Sharklet is a plastic sheet product from Sharklet Technologies, whose microstructure surface effectively prevent the colonization and growth of bacteria. The unique surface texture is inspired by dermal denticles of shark skin and developed by Dr. Tony Brennan, material science and engineering professor at the University of Florida. Examining the dermal denticles with scanning electron microscopy, Dr. Brennan found that they are arranged in a distinct diamond pattern with tiny riblets (Sharklet 2018). The specific width-to-height ratio of the ribs are measured by Dr. Brennan, which is also compared with his mathematical model for roughness and shows the potential of preventing microorganisms from settling. Impressive results, up to 85% reduction of green algae settlement on sharklet surface compared to smooth surface, have been observed by initial tests conducted by Sharklet company. The pattern of dermal denticles and Sharklet is shown in Figure 2.13.

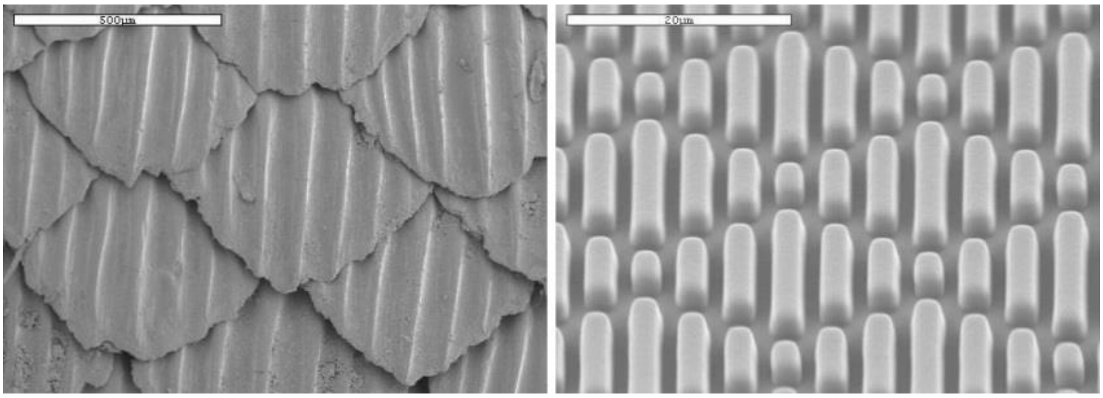

Figure 2.13 Dermal denticles on the left side, and Sharklet AF^{TM} design on the right side (From Sharklet Technologies Inc.)

Due to the Sharklet's superior resistance to bacterium attachment and pure physical mechanism, it soon came into notice and became a promising non-toxic fouling-control approach. Carman, Estes et al. (2006) provided the first demonstration of an engineered micro-topography inhibiting the settlement of spores of a marine alga. Experimental results showed that bio-replicated PDMSe surface of Sharklet AF^{TM} topography reduced settlement of the Ulva spore by 86%. The efficient anti-fouling property of Sharklet AF^{TM} topography was also validated by Schumacher, Long et al. (2008), Long, Schumacher et al. (2010), and Magin, Cooper et al. (2010).

Chung, Schumacher et al. (2007) conducted experimental investigations of Sharklet AF^{TM} topography's ability to impede biofilm formation. Polydimethylsiloxane (PDMSe) has been employed by Chung, Schumacher et al. (2007) to manufacture Sharklet AF^{TM} surface and reference smooth surface, over which the biofilm formation of *Staphylococcus aureus* is tested over 21 days course. During the entire test period, no evidence of biofilm colonization is found for the Sharklet AF^{TM} surface until day 21. However, for the smooth surface, early-stage biofilm colonization is found at day 7 with 54% coverage of *S. aureus*, compared to 7% coverage for the topographical surface. These results propose that the topographical features of Sharklet AF^{TM} might well have a superior performance to inhibit the biofilm formation of *S. aureus*.

It is needed to point out that Sharklet AF^{TM} surface pattern is not the same as dermal denticles found on shark skin, but biomimetically inspired surface structure. The dimension of Sharklet AF^{TM} is largely reduced and the crown tips are flattened (Carman, Estes et al. 2006).

Coarse Surface Topography (Tubeworm larva, Barnacle cypris larva)

- Barnacle Specific Sharklet AF^{TM} topography

The length scale of fouling-control surface topography is an important factor that will affect the fouling deterrence impact. Concerning the dimensional differences of marine organisms as shown in Figure 2.11, it is more plausible to employ larger surface topography to resist fouling attachment of tubeworm larvae (~200µm for *Hydroides elegans*) and barnacle cypris larvae (~500 µm for *Balanus Amphitrite*).

The larger Sharklet topographical features engineered in polydimethylsiloxane (PDMSe) have been investigated by Schumacher, Long et al. (2008) on the settlement of cyprids of *Balanus Amphitrite.* The barnacle-specific Sharklet AF^{TM} topography (40µm feature height, 20µm feature width) reduced cyprid settled by 97% compared to the smooth PDMSe surface. Although the enlarged Sharklet AF^{TM} has shown an excellent fouling-control performance for the particular fouling animal of interest, more designed experiments are still needed to understand its ability to resist a broader range of fouling plant or animal of interest. The identification of effective fouling-control topographies typically occurs through trial-and-error and there is still much to be studied and understood in terms of the unique properties of the shark skin surface that make it such an effective fouling-control surface.

2.6.2.2 *Theories of Fouling-Control Surface*

Two existing fouling-control surface theories such as number of distinct topographic features and attachment point theory are discussed below, any of which may affect the fouling organisms' attachment.

Number of Distinct Topographic Features

In the area of fouling-control using surface pattern technology, the impact of the number of distinct topographic features (n) is significant, that is evidenced in the work of Callow and Callow (2011). The fouling-control tests examined the settlement of spores of Ulva on micro-engineered Sharklet AF pattern moulded in PDMSe by comparing the smooth surface and those with different number of distinct topographic features, as shown in Figure 2.14.

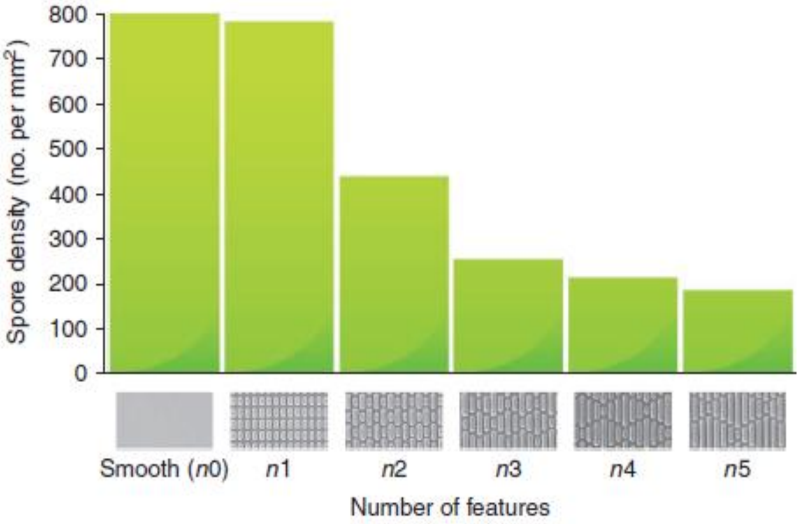

Figure 2.14 Settlement of spores of Ulva on micro-engineered Sharklet AF patterns moulded in PDMSe (Callow and Callow 2011)

As shown in Figure 2.14, the surface ability to resist spore from settling is greatly improved as the number of topographic features increase. It is also noticed that the improvement of surface fouling-control ability is not significant when n=1 (slight improvement compared to smooth surface) and n>3 (slight improvement as n increases). The excellent fouling-control performance of Sharklet pattern is explained as the result of nanoforce gradients, a concept proposed by Schumacher, Long et al. (2008). As suggested by Schumacher, Long et al. (2008), the complexity of Sharklet pattern might cause stress gradients within the membrane of a settling microorganism during initial contact, the unstable state of which will interrupt the microorganism settlement by causing a disturbance. A more detailed explanation is provided by Schumacher, Long et al. (2008), it is found that most cell/microorganism need to consume energy for the settlement and stability on target surfaces, which are essential to overcome the stresses of the contact area posed by different topographical features. However, the net energy consumption to achieve the steady settlement state is not thermodynamically favourable and does not always occur because cell/microorganism will prefer to probe another area that is much easier to settle.

Attachment Point Theory

As suggested by the attachment point theory (Scardino, Harvey et al. 2006), the fouling-control effect of the surface topography is directly related to the relevant scale of the surface and the fouling organism. If the fouling organism is larger than the scale of the surface feature, the adhesion strength will be weaker due to less attachment points. If the fouling organism is smaller than the scale of the surface feature, the adhesion strength will be stronger due to more attachment points. To make the attachment point theory much clearer, a schematic figure is shown in Figure 2.15.

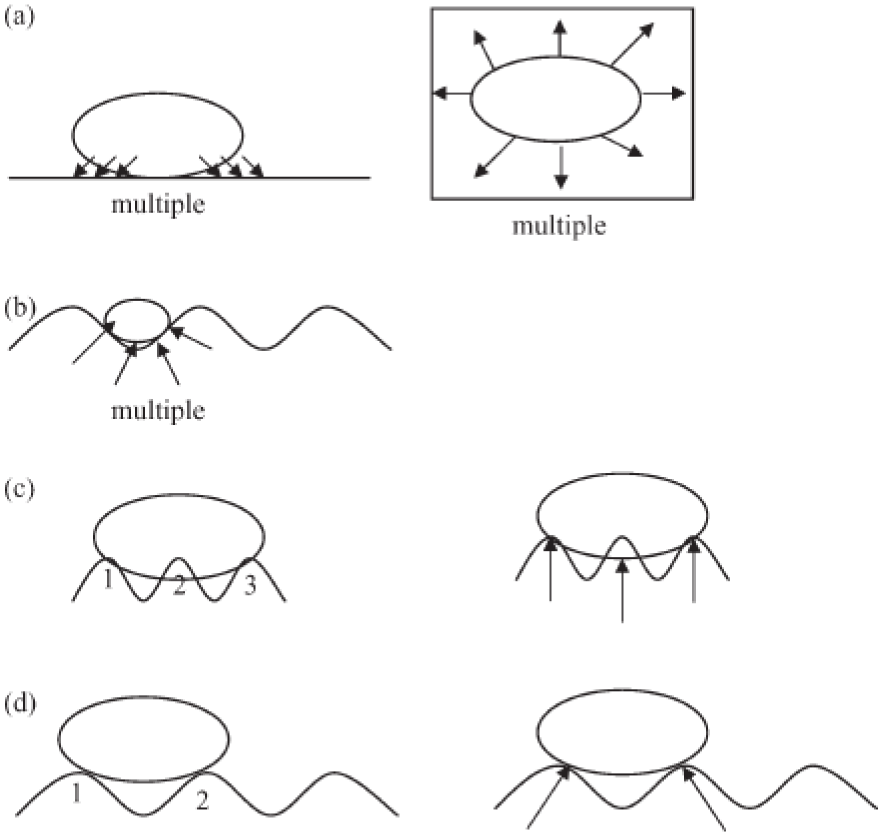

Figure 2.15 A schematic illustration of theoretical attachment points (a) smooth surface – multiple attachment points (b) ripples – multiple attachment points (c) ripples – 3 attachment points (d) ripples-2 attachment points. (Scardino, Harvey et al. 2006)

Static bioassays were conducted by Scardino (2006) to test the attachment point theory based on diatom attachment on micro-patterned polyimide surfaces, the results of which support the application of attachment point theory to diatoms. It is found that reduced number of attachment points is associated with lower attachment of diatoms and increased number of attachment points is associated with more attachment of diatoms.

2.7 Summary

The available literature focusing on the drag-reduction technologies and innovative non-toxic fouling-control systems, both of which contribute to a better ship energy efficiency and less environmental impact (air pollution and harm to the marine ecological system), have been reviewed. The past work, especially riblet drag-reduction structure, and Sharklet AF^{TM} have been discussed in detail and the gaps in the literature were determined. The important conclusions are listed below:

- Energy efficiency regulations such as EEDI and SEEMP, have entered into force and the technical and operational measures suggested by MEPC were made mandatory for all ships irrespective of flag and ownership. As a result, green innovations need to be developed and spread to reduce the diesel exhaust emissions so that the requirements of legislative frameworks can be satisfied.

- Nowadays, toxic biocide-based fouling-control systems are under increasingly stringent scrutiny due to the new environmental protection criteria such as the 6th Environmental Action Plan, the EU Water Framework Directive, and the Biocidal Products Criteria. In the short term, no alternative seems able to reach a sufficient degree of development to replace biocide-based antifouling systems. Thus, new research of environmentally benign coating systems is needed to overcome this technical gap.

- Although the riblet drag-reduction technique is a reliable energy-efficient method, it has not been widely used in the maritime shipping industry because current research has not indicated the anti-fouling capability of the riblet surface. The lack of fouling-control performance makes it impractical to be used on the under-water ship hull surface, where the formation of biofouling will cause damaging effect to riblet drag-reduction performance. Therefore, the traditional riblet surface needs to be optimized to possess a combined function of drag-reduction and anti-fouling in order to be used as an efficient maritime energy-saving technique.

- Currently, Direct Numerical Simulation (DNS) is the primary turbulence modelling method in the field of CFD to study riblet structure. However, it requires a huge amount of computational core hours and associated financial cost, which will significantly increase the R&D time and cost for a riblet-related industrial project. As a result, an alternative engineering turbulence modelling method needs to be found and validated to predict the drag-reduction performance of a particular riblet structure at an acceptable level of accuracy.

- As a promising surface technology, the impact of riblet structure on a full-scale ship is still not well evaluated because most riblet research, either numerical or experimental, only focuses on the riblet surface in the channel flow environment. As a consequence, a feasible approach to predict riblet's effect on the full-scale ship is needed and hence the shipping companies will become more aware of the benefits of using the riblet technique.

3. Validation Test

3.1 Introduction

As mentioned in Chapter 1, CFD method is employed in this thesis to study the drag-reduction performance of the new design surface. However, prior to the CFD investigation of the new surface topography, it is very important to ensure that the selected RKE 2L turbulence model is able to reflect the impact of surface topography on the near-wall turbulent activities. In the following sections, the validation test of a traditional symmetric v-groove riblet structure is conducted in the fully-developed turbulent channel flow to examine if any near-wall effects caused by riblet can be captured.

In Section 3.2, the fundamental knowledge of the channel flow will be reviewed together with relative physical definitions such as Reynolds shear stress, inner layer scaling, law of the wall, and velocity defect law. Due to the micro-scale of the target research surface and requirement of an acceptable computational cost, internal channel flow is chosen as the computational model for the investigation of the drag-reduction structure.

In Section 3.3, the mathematical model, which is utilized to model the turbulent channel flow, is introduced. The Realizable K-Epsilon two layer (RKE 2L) model provided by the commercial CFD software STAR-CCM^{+} is used to reproduce turbulence. The built-in governing equations are also indicated in this section.

In Section 3.4, the research problem is depicted in detail. Firstly, the geometry of the selected triangular riblet structure is specified. Secondly, the computational box of the channel and the implemented boundary layer conditions are indicated. Finally, detailed mesh specification of computational domain is shown and mesh dependence tests for both plane channel flow and riblet channel flow have been conducted to determine the appropriate mesh refinement for the following studies.

In Section 3.5, the RKE 2L turbulence model is examined to explore whether a plausible drag-reduction performance is derived. The impact of the riblet's surface topology on the mean velocity profile and near-wall turbulent activities is discussed.

For a better understanding of the obtained numerical results, popular riblet drag-reduction theories are also presented in this section.

In Section 3.6, the summary of this chapter is given.

3.2 Basic Definitions of Channel Flow

The basic physical definitions relevant to the channel flow are shown in this section.

3.2.1 Channel Flow and Reynolds Number

Plane channel flow is always used as a tool to analyse the turbulent boundary layer structure d0ue to its geometric simplicity. Generally, a plane channel is composed of two infinite planes, separated with a distance of 2δ in the wall-normal direction as channel height. The streamwise length and spanwise length of the channel satisfy $\frac{L}{\delta} \gg 1$ and $\frac{W}{\delta} \gg 1$, where L is the channel length, W is the channel width, and δ is half channel height. The size of channel length, width and height are specified based on Reynolds number so that all turbulent statistics will not be disturbed by each other and will be explained afterwards in the simulation. In the case of channel flow, there are two mostly frequently used Reynolds number based on different turbulent scales.

Reynolds number based on the main dimension:

$$Re = \frac{\bar{U}2\delta}{\nu} \tag{3}$$

Where $\overline{\mathrm{U}}$ is bulk velocity, δ is half channel height, and ν is the kinetic viscosity.

Reynolds number based on viscous scales:

$$Re_{\tau} = \frac{u_{\tau}\delta}{\nu} \tag{4}$$

Where $\mathrm{u}_{\tau}$is the friction velocity.

Normally, the flow is laminar for Re<1350, and fully turbulent for Re>1800. (Pope 2000)

3.2.2 Reynolds Shear Stress and Inner Layer Scaling

Different from the free shear flows, wall-bounded flow is affected by the presence of the wall. In the region close to the wall, viscous stresses dominate and Reynolds shear stress is small. In contrast, the viscous stress is negligibly small compared to the Reynolds stresses in the free shear flows. Figure 3.1 below clearly shows the variation of viscous stress and Reynolds shear stress from the wall to centreline of the channel.

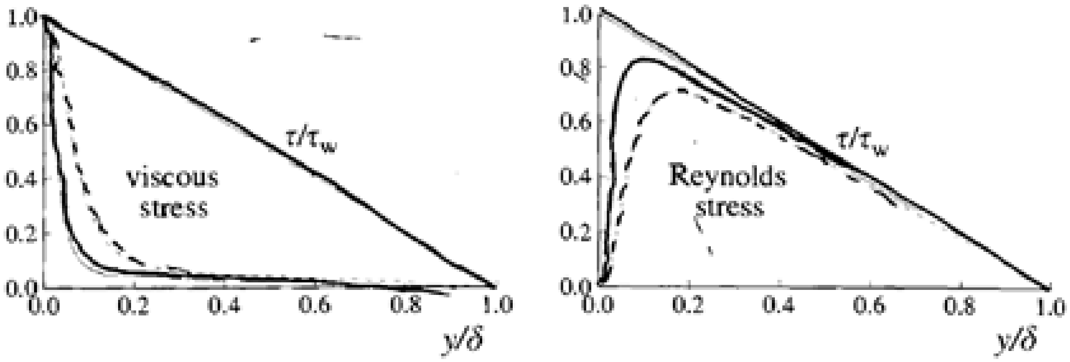

Figure 3.1 Profiles of the viscous shear stress and the Reynolds shear stress in turbulent channel flow: DNS data of Kim, Moin et al. (1987): dashed line, Re=5,600; solid line, Re=13,750. (Pope 2000)

The mathematical expression of near-wall shear stress is:

$$\tau_y = \rho\nu\frac{dU}{dy} - \rho uv \qquad (5)$$

At the wall, due to the no-slip boundary condition, the velocity is zero and thus Reynolds shear stress is zero. The near wall shear stress (τ_w) is equal to the viscous stress at y=0.

$$\tau_w = \rho\nu(\frac{dU}{dy})_{y=0} \qquad (6)$$

Hereby, two fundamental parameters associated with the wall-bounded flow are introduced:

Friction velocity: $u_\tau = \sqrt{\frac{\tau_w}{\rho}}$

Viscous length scale: $\delta_\nu = \frac{\nu}{u_\tau}$

It is interesting to note here that if all the components of Reynolds number formula are replaced by viscous scales as shown above, then Reynolds number can be regarded as a unit.

Alternatively, the formula of Re_τ could be written as:

$$Re_\tau = \frac{\delta}{\delta_v} \tag{7}$$

Similarly, we have non-dimensional wall-normal distance y^+ as:

$$y^+ = \frac{u_\tau y}{\nu} = \frac{y}{\delta_v} \tag{8}$$

It is proper to deduce the intensities of viscous stress and Reynolds shear stress based on the y^+ value as a local Reynolds number.

Actually, the channel flow could be divided into several regions based on viscous length-scale (δ_v), and channel scale (δ) and the region partitions of the turbulent boundary layer are shown in Table 3.1.

Table 3.1 Region partitions of the turbulent boundary layer (Pope 2000)

$y < 5\delta_v$	Viscous sublayer	Viscous stress dominates, Reynolds stress is negligibly small
$5\delta_v < y < 30\delta_v$	Buffer layer	Viscous stress decreases, Reynolds stress increases; equilibrium is reached at $y = 12\delta_v$, after which Reynolds stress dominates
$30\delta_v < y < 0.3\delta$	Log layer	Effects of viscous stress gradually vanish
$y < 50\delta_v$	Inner layer	Near-wall shear stress dominated by viscous stress and Reynolds stress
$y > 50\delta_v$	Outer layer	Effects of viscous stress are negligible

3.2.3 Law of the Wall

Prandtl (1934) proposed that the velocity profile in the inner layer ($y^+<50$) is supposed to be independent of half channel width (δ), and centreline velocity (U_c) but is closely associated with viscous scales. Moreover, the velocity at a certain point is proportional to the logarithm of the distance from that point to the wall. (Von Karman, 1930) This is the well-known law of the wall. Since the inner layer of the turbulent boundary layer is the region of interest where the phenomenon of riblet drag reduction occurs, a brief introduction of the law of the wall will be given here.

The velocity profile of the inner layer could be depicted as below:

$$u^+ = y^+ \ (y < 5\delta_v) \tag{9}$$

$$u^+ = \frac{1}{\kappa} lny^+ + C^+ \ (y > 30\delta_v) \tag{10}$$

However, there is no equation that could accurately describe the velocity profile in the region between $5\delta_v$ and $30\delta_v$. Normally, $12\delta_v$is regarded as a transition point of these two equations, to which value the range of Eq.9 and Eq.10 are extended so that an acceptable accuracy of near wall velocity profile could be predicted. In the literature, there is some variation in the values ascribed to the log-law constants, but generally are within 5% of $k=0.41$, $C^+=5.2$.

It is shown by Nikuradse (1954) that an additional term of F, which accounts for the roughness of the pipe wall, should be added into Eq.10. The same idea was also proposed by Hama (1954), and a parameter h^+, normalized by viscous length-scale, is used to represent the height of roughness. Thus a new velocity profile is formed as follows:

$$u^+ = \frac{1}{\kappa} lny^+ + C^+ + F(h^+) \tag{11}$$

Not only is this true for a drag-increasing (rough) wall, it is also equally true for a drag-reducing (riblet) geometry, as verified by sample profiles of Sawyer and Winter (1987). It is found that $F(h^+)$ is negative for a drag-increasing surface and positive for a drag-reduction surface.

3.2.4 Velocity Defect Law

In the outer layer (y^+>50), the case is different where the velocity profile is independent of viscous scales. The assumption of the independence of viscosity gives rise to the appearance of the velocity defect, which will be explained here in terms of the mathematical method.

For a fully developed channel flow, it is possible to specify it with only four parameters: ρ, ν, δ, u_τ. Thus, the following relationship is derived:

$$u = u_\tau f\left(\frac{y}{\delta}, Re_\tau\right) \tag{12}$$

If the derivative of velocity is taken in the wall normal direction, we have:

$$\frac{du}{dy} = \frac{u_\tau}{y} F\left(\frac{y}{\delta_v}, \frac{y}{\delta}\right) \tag{13}$$

The assumption that $F(\frac{y}{\delta_v}, \frac{y}{\delta})$ is independent of ν implies that, for large $\frac{y}{\delta_v}$, F tends asymptotically to a function of $\frac{y}{\delta}$ only, i.e.,

$$\lim_{\frac{y}{\delta_v}\to\infty} F(\frac{y}{\delta_v}, \frac{y}{\delta}) = F_0\left(\frac{y}{\delta}\right) \tag{14}$$

Substituting F_0 for F in Eq. 14 and integrating between y and δ then yields the defect law due to von Karman (1930)

$$\frac{U_C - u}{u_\tau} = F_D\left(\frac{y}{\delta}\right) \tag{15}$$

Where

$$F_D\left(\frac{y}{\delta}\right) = \int_0^1 \frac{1}{y^+} F_0(y^+) dy^+ \tag{16}$$

Unlike the law of the wall, there is no general formula of $F_D(\frac{y}{\delta})$, which is relying on different flow conditions.

3.3 Mathematical Model

The computational code used to perform RANS of the fully-developed turbulent channel flow is developed by STAR-CCM$^+$ (commercial software). The code uses finite volume solver, with a second-order upwind scheme for the discretization of convection and viscous fluxes of the momentum equations, and first-order temporal or Euler implicit scheme for the time discretization. The code has been used for many industrial-type calculations containing turbulence and heat transfer.

Many different forms of K-Epsilon model have been developed and applied in the past half century, and gradually become the most widely spread and employed turbulence model for all sorts of industrial applications. Nowadays, K-Epsilon model has been improved greatly and becomes very mature as a result of consistent efforts in the past decades, the most recent developments of which have been incorporated into Star-CCM+ (CD-ADAPCO 2017). In order to reproduce a good representation of near-wall turbulent statistics, the specific Star-CCM+ built-in Realizable K-Epsilon Two-layer Turbulence model (RKE 2L) is employed in this work to study the fully developed channel flow.

The RKE 2L model combines Realizable K-Epsilon model with the two-layer approach. Different from standard model, a new transport equation for the turbulent dissipation rate is incorporated in the realizable K-Epsilon model and traditional constant value of Cμ is replaced by a function of mean flow and turbulence properties (CD-ADAPCO 2017). The two-layer approach is firstly proposed by Rodi (1991) that allows the K-Epsilon model to be applied in the viscous-affected layer. In this approach, the computation is divided into two layers. In the layer next to the wall, the turbulent dissipation rate ε and turbulent viscosity μ_t are specified as functions of wall distance. The values of ε specified in the near wall layer are blended smoothly with the values computed from solving the transport equation far from the wall. The equation for the turbulent kinetic energy is solved across the entire flow domain. This explicit specification of ε and μ_t is arguably no less empirical than damping function approach, and the results are often as good or better.

The transport equation of RKE 2L model is as follows:

Turbulence Kinetic Energy:

$$\frac{\partial}{\partial t}(\rho k) + \nabla \cdot [\rho k \bar{v}] = \nabla \cdot \left[\left(\mu + \frac{\mu_t}{\sigma_k}\right)\nabla k\right] + P_k - \rho\big((\varepsilon - \varepsilon_0)\big) + S_k \tag{17}$$

Dissipation Rate:

$$\frac{\partial}{\partial t}(\rho \varepsilon) + \nabla \cdot [\rho \varepsilon \bar{v}] = \nabla \cdot \left[\left(\mu + \frac{\mu_t}{\sigma_\varepsilon}\right)\nabla \varepsilon\right] + \frac{1}{T_\varepsilon} C_{\varepsilon 1} P_\varepsilon - C_{\varepsilon 2} f_2 \rho \left(\frac{\varepsilon}{T_\varepsilon} - \frac{\varepsilon_0}{T_0}\right) + S_\varepsilon \tag{18}$$

The turbulent eddy viscosity μ_t is calculated as:

$$\mu_t = \rho C_\mu f_\mu k T \tag{19}$$

The formulation of the production terms

$$P_k = f_c G_k + G_b + \Upsilon_M \tag{20}$$

$$P_\varepsilon = f_c S k + C_{\varepsilon 3} G_b \tag{21}$$

For turbulence models that resolve the viscous- and buffer-layer, damping functions mimic the decrease of turbulent mixing near the walls. For the RKE and RKE 2L models, damping functions enforce reliability.

$$f_2 = \frac{k}{k + \sqrt{\nu k}} \tag{22}$$

$$f_\mu = 1 \tag{23}$$

The associated model coefficients are shown in Table 3.2.

Table 3.2 Model coefficients (CD-ADAPCO 2017)

$C_{\varepsilon 1}$	$\max(0.43, \frac{\eta}{5+\eta})$ where: $\eta = \frac{Sk}{\varepsilon}$
$C_{\varepsilon 2}$	1.9
C_μ	$\dfrac{1}{4 + \sqrt{6} cos\left[\frac{1}{3}\operatorname{acos}(\sqrt{6}\frac{S^3}{\sqrt{S:S}^3})\right]\sqrt{S:S + W:W}\frac{k}{\varepsilon}}$
C_M	2

The details of the value and formula for the coefficients shown above are available in CD-adapco.

3.4 Problem Description

3.4.1 Surface Geometry

As the most frequently studied riblet structure, symmetric v-groove riblet is selected as the target surface in the validation test. The specification of the symmetric v-groove riblet surface is shown in Figure 3.2, where s is the spacing of the rib and the rib angle is 60˚. The specific surface is formed by extruding zig-zag line of constant angle (60˚ in this case) in the flow direction.

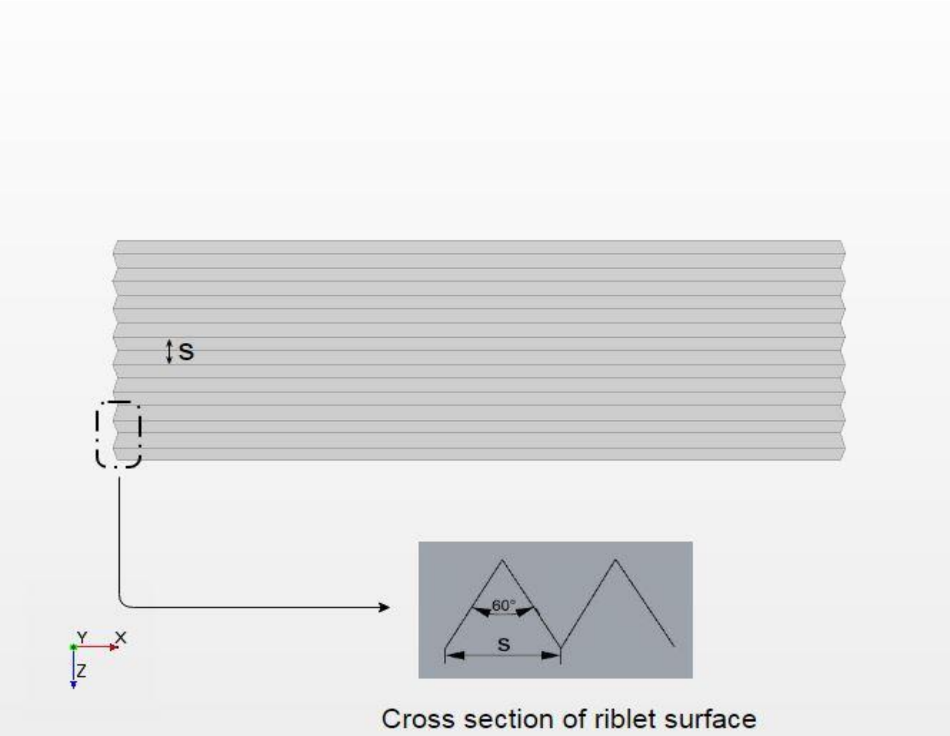

Figure 3.2 Specification of the symmetric v-groove riblet surface

3.4.2 Computational Box and Boundary Conditions

Similar to the work of Choi, Moin et al. (1993), the length of the computational box in the streamwise, spanwise, and wall-normal directions are separately 3δ, δ, 2δ, where δ represents the half channel height. The simplicity of the geometry makes it possible to focus the attention on the near-wall region of interest, with no regard to any unnecessary effects that might be caused by a complex geometrical shape. The computational box of riblet channel is shown in Figure 3.3.

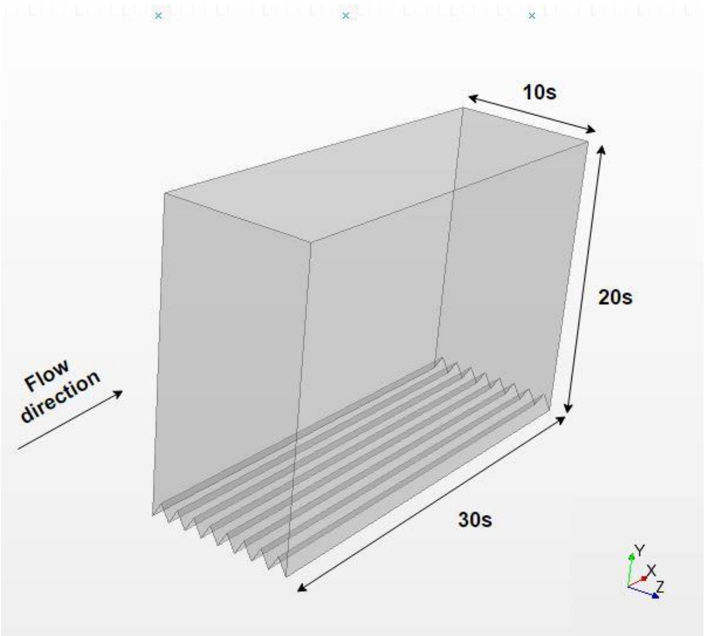

Figure 3.3 Computational box of riblet channel

The computational box generally satisfies the conclusion of the minimal flow unit suggested by Jimenez and Moin (1991): minimal spanwise length = 100 wall units; minimal streamwise length =250-350 wall units. The significance of Jimenez's work is that it quantifies and simplifies the research of turbulent channel flow study. In the suggested minimal flow unit, it is possible to sustain most of the fundamental near-wall turbulent activities in the fully developed turbulent channel flow. In contrast to a general channel, the cost of computation is significantly reduced with no compromise in the simulation of near-wall turbulent structure and dynamics.

The computational box is composed of six faces, with three separate sets in three different directions: inlet & outlet (main flow direction), symmetry planes (spanwise direction), no-slip wall (wall-normal direction). Periodic boundary conditions are applied in the streamwise (x) and spanwise (z) directions and the pressure gradient that drives the flow is adjusted dynamically to maintain a constant mass flow rate ($\dot{m} = \rho U_b A$, where U_b is the bulk velocity and A is the channel cross-section area) through the channel.

3.4.3 Mesh

Automatic mesh generator in STAR-CCM+ is used and particular functions of trimmer and surface remesher are enabled to generate uniform structured mesh cells. The computational grid is distributed uniformly in the streamwise and spanwise directions, but non-uniformly in the wall normal direction. As indicated by Choi (1989), riblets only affect the inner part of the boundary layer which is a few riblet heights away from the wall. Generally, the entire computational domain is split into five parallel blocks, represented by three different levels of mesh refinements. Thus the finest mesh will only be applied in the riblet affected region, which spans approximately double rib height for the block nearest to the wall. As wall distance increases, the 2nd and 3rd level of mesh refinement will be used since it is less affected by the existence of riblets and will greatly reduce the cost of computational resources.

As shown in Figure 3.4, the y-z view and volume mesh of the computational domain is shown. It is needed to point out that enough grid points (~18 points along rib spacing, ~16 points along rib height) are allocated for each rib in order that the turbulent activities in the riblet affected region can be well captured.

(a)

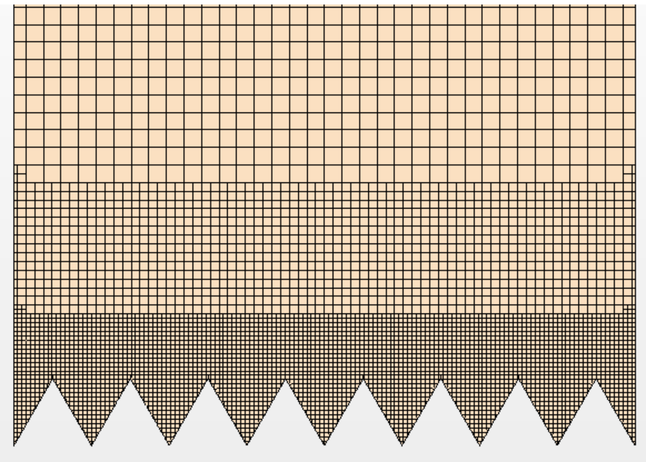

(b)

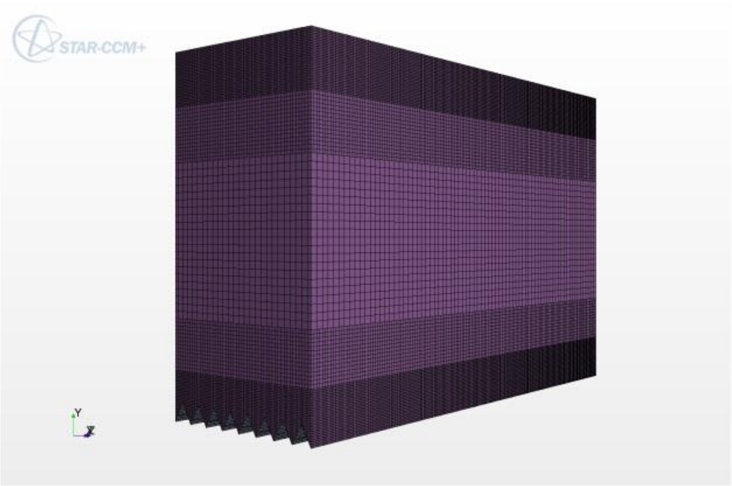

Figure 3.4 (a) y-z view of numerical grid (b) Computational mesh of riblet channel

As k-epsilon turbulence model is used in this study, the question of whether wall function is used in the near wall region is always proposed. Wall function is always not suitable for flows at low to moderate Reynolds number and thus not preferred in the near wall region. This might be due to its working range at $y^+ > 30$ that makes the statistics under 30 wall units in the wall normal direction inaccurate. However, the case is different in STAR-CCM$^+$. The normal application range of $y^+ > 30$ is extended to include the accurate representation in the viscous sublayer and buffer layer. A new option called Low y^+ Wall Treatment is incorporated into the mesh options and thus the near region could be well calculated using this function as long as the middle point of the first mesh layer is smaller than one wall unit.

3.4.3.1 Mesh Independence Test

Systematic mesh independence studies of turbulent riblet channel are carried out here to examine the sensitivity of calculated turbulent statistics, such as riblet surface friction coefficient, to grid resolution. Simulations of three levels of mesh refinements (coarse, medium, and fine) are separately run for the riblet channel flow. The grid refinement factor, r, is chosen to be $\sqrt{2}$. The fine mesh is firstly created in the CFD simulation. To avoid putting the solution out of asymptotic range, the number of grid points is not halved in each direction to obtain the coarser grid while non-integer grid factor, $\sqrt{2}$, is used. Results calculated by the CFD simulations are shown in Table 3.3.

Similar non-integer grid factor method has also been used for other CFD studies by Tezdogan, Demirel et al. (2015) and Demirel, Turan et al. (2017).

Table 3.3 C_{f_riblet} results at three mesh refinements for riblet channel at Re=11,200

Mesh refinement	Total No. of Cells	Computational Cost (Core hours)	C_{f_riblet}
Coarse	5.22×10^5	180	0.007013
Medium	1.50×10^6	438	0.007009
Fine	3.79×10^6	1008	0.007040

As shown in Table 3.3, the friction coefficients of the symmetric v-groove riblet surface are indicated at three different mesh refinements. The value of C_{f_riblet} shows a fluctuating convergence although the differences among three different mesh refinements are pretty small. However, to make sure the numerical result is generally independent of mesh refinement, an additional comparison is made between numerical results and empiric formula suggested by Dean (1978) in terms of top smooth plate friction coefficient, as shown in Table 3.4.

Table 3.4 C_{f_smooth} results at three mesh refinements for riblet channel at Re=11,200

Mesh refinement	Total No. of Cells	C_f (CFD)	C_f (Dean 1978)	Absolute Difference (%)
Coarse	$5.23 * 10^5$	0.007189	0.007096	1.31%
Medium	$1.54 * 10^6$	0.007179	0.007096	1.17%
Fine	$3.76 * 10^7$	0.007147	0.007096	0.71%

Dean's empiric correlation: $C_f = 0.073 * Re^{-0.25}$

As shown in Table 3.4, a mesh convergence trend has been observed by finding that the friction coefficient gradually decreases as mesh becomes finer and finer. For the fine mesh refinement, only 0.71% difference exists between numerical results and Dean's empiric formula, which is small enough to state that the numerical statistics is almost independent of fine mesh refinement. As a result, fine mesh refinement is chosen chosen for riblet channel flow simulations due to its relatively good accuracy and acceptable computational cost.

3.5 Results

3.5.1 Riblet Channel Validation Test

Most of the work on the RANS study of fully developed turbulent channel flow with a plate covered with riblet structure is carried out by Djenidi, Squire et al. (1991), Djenidi and Antonia (1993), Launder and Li (1993). Djenidi adopted an existing k-ε model (Chien 1982) for the calculation. The result shows an over-underestimated drag reduction, which is attributed to incorrect use of damping factor (f_μ=1-$e^{(-0.0115y+)}$) because the damping factor introduces the near wall effects by including non-dimensional wall distance y^+. Within the grooves, friction velocity is not constant but varies significantly along the groove contour, which is not appropriate to represent the damping effects. Launder and Li (1993) applied the classical isotropic turbulent viscosity model to approximate the turbulent stresses proposed by Launder and Sharma (1974) while the proximity to the wall is sensed only through the local value of turbulent Reynolds number. The obtained results indicate a broadly correct drag reduction level, but the use of viscosity formulation will suppress secondary motions. As a result, second momentum closure is introduced in the region above the riblet tips in place of the eddy viscosity model. Hereby, a k-epsilon model of STAR-CCM$^+$ will be employed here with good improvements in transport equations to explore the drag reduction performance of riblet surface in a fully developed turbulent channel flow.

3.5.2 Drag Reduction Results

It is noted that almost 6-8% drag reduction could be obtained for an optimum triangular riblet (Walsh 1990). However, due to problems with measurement accuracy and quality of the machined surface, it is difficult to observe drag variation since the changes in drag maybe within the scatter of measurement and unknown effects of the imperfect machined surface on drag performance (Walsh 1990). As a result, a data band that incorporates all available experimental data of triangular riblet is collected to establish a drag-reduction performance curve, and the experimental specifications are shown in Table 3.5.

Table 3.5 All available drag-reduction performance data for triangular riblet (53-degrees to 66-degrees)

Publication	*h (mm)*	*s (mm)*	*α (rib angle)*
Walsh and Lindemann (1984) _ Model 13R	0.5100	0.5100	53.13°
Walsh and Lindemann (1984)_Model 33	0.2500	0.2500	53.13°
Walsh (1990) _ Case 1	0.0330	0.0330	53.13°
Walsh (1990) _ Case 2	0.0762	0.0762	53.13°
Walsh (1990) _ Case 3	0.1143	0.1143	53.13°
Sawyer and Winter (1987)	0.3900	0.5000	65.32°
Enyutin, Lashkov et al. (1987)	N/A	N/A	63.37°
Reidy (1987)	0.0762	0.0762	53.13°
Coustols, Gleyzes et al. (1988)	0.1524	0.1524	53.13°
Pulles (1988)	N/A	N/A	53.13°
Beauchamp and Philips (1988)	0.0330	0.0330	53.13°
Liu, Christodoulou et al. (1990)	0.1143	0.1143	53.13°
Bechert, Bruse et al. (1997) _ Case a	2.64	3.04	60°
Bechert, Bruse et al. (1997) _ Case b	5.31	6.1	60°
Current CFD work 1	0.1080	0.1250	60°
Current CFD work 2	0.3900	0.5000	65.32°

For the same value of h^+, Models 13R and 33 indicate a 5% discrepancy due to peak curvature of Model 33 caused by the quality of machined surface (Walsh 1982). The data of Coustols, Gleyzes et al. (1988) is obtained from velocity profile measurement, the drag measurement of which produces data that does not follow the dominant trend and is thus omitted in our data band. Walsh and Lindemann (1984) claimed that the triangular form with a height-to-spacing ratio of one appears to be the optimum and most practical riblet. A rib angle of 60° is used in the current validation test since the small gap between the suggested rib angle of 53.13° $(h/s = 1)$ and 60° is proven not to be so important (Bechert, Bruse et al. 1997). The commercial code capability to reproduce the drag-reduction result for the traditional triangular riblet is examined here.

3.5.2.1 General Validation Test

Seven different speeds of flow are implemented to cover a relatively broad range of s^+ value ranging from 4.7 to 50.8, which provides a full picture of the trending. The results of drag-reduction values for the current CFD work 1 and previous experimental and RANS results are compared and shown in Figure 3.5.

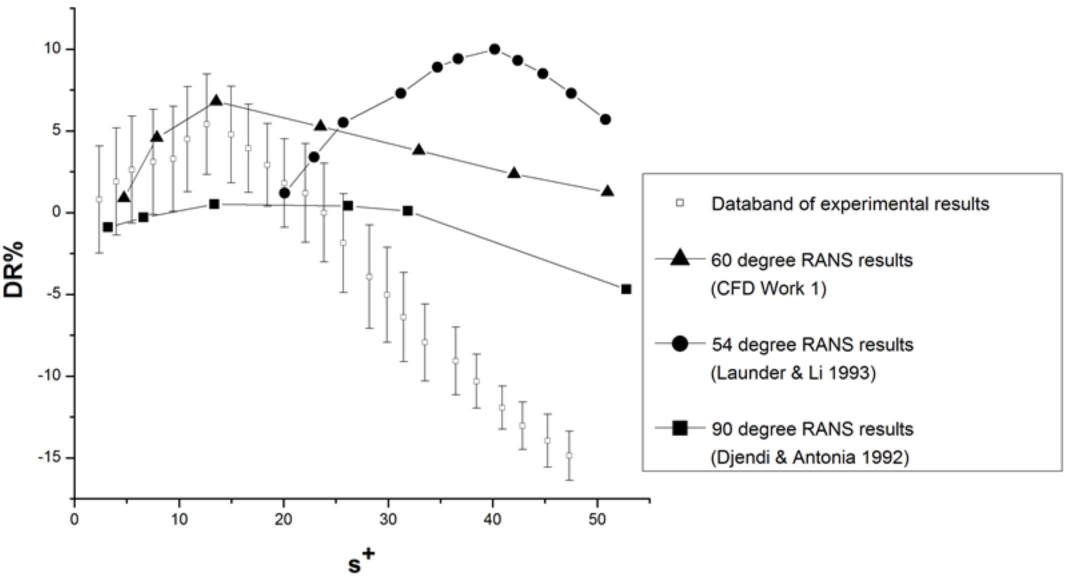

Figure 3.5 Comparison of current CFD work 1 and previous experimental and RANS data

The calculated drag reduction percentage, $\mathrm{DR\%} = \frac{F_S - F_R}{F_S}$, where F_R is the riblet frictional resistance and F_S is the frictional resistance on a smooth flat plate, is shown in Figure 3.5 for different values of s^+.

Djenidi and Antonia (1992) adopted an already existing k-ε model (Chien 1982) by introducing a new damping function for the calculation of a turbulent boundary layer over a riblet wall. However, their calculated drag-reduction strongly underestimates the measurements of the summarized experimental data band, as shown in Figure 3.5. Moreover, when s^+ approaches 0, DR% falls below 0 whereas it is expected to approach 0 (e.g. $s^+=0$ is equivalent to a smooth surface). As indicated by Djenidi and Antonia (1992), the problem might be caused by the lack of reassessment of k and ε modelling, which is significantly affected by the choice of damping function and f_μ. It needs to be noted that the modelling of k and ε in turn require the reassessment of

various empirical constants (C_μ, $C_{\varepsilon 1}$, $C_{\varepsilon 2}$, σ_k, σ_ε) as well as the functions (f_1, f_2).

Another numerical riblet using k-ε turbulence model was conducted by Launder and Li (1993), who employed an isotropic viscosity model for the turbulent stresses and therefore no secondary motions. As seen in Figure 3.5, the values of s^+ where the optimum drag reduction occurs are 2-3 times greater than reported by experimental measurements. As indicated by Launder and Li (1993), the most likely reason is the absence of secondary flows from the calculations, which is an inevitable consequence of adopting an isotropic viscosity model. The following exploration conducted by Launder suggests that the use of a second moment closure, rather than eddy viscosity model, can reproduce sweep motions in the near-wall turbulent boundary layer region which move towards the riblet surface at high-speed and lead to increased riblet skin friction (Launder and Li 1993).

Compared to the riblet drag results calculated by k-ε turbulence model mentioned above, the present numerical results of the 60° symmetric v-groove riblet using RKE 2L turbulence model are generally in accord with the measurements of the summarized experimental data band. A maximum DR% value of 6.80% is found at approximately $s^{+}=13$, which fits well with the established data band. A reasonable prediction of the riblet drag-reduction performance is reproduced when s^{+} is smaller than the optimum value where maximum drag reduction occurs, but the prediction beyond that optimum s^{+} value is far from satisfactory where a much lower DR% decreasing rate is found compared to the experimental results.

Based on the calculated results, it is plausible to deduce that the explicit use of ε and μ_t, rather than damping function, in the present model shows a better near-wall performance than that of Djenidi and Antonia (1992). However, as s^{+} exceeds the optimum value, riblet frictional drag is found to be overestimated. Similar results were found by Launder and Li (1993) because both turbulent models lack the ability to reproduce any turbulence-driven secondary motions. Although the present RANS results only show a reasonable estimate of riblet drag-reduction performance at a certain range of s^{+}, it is unlikely that there will be significant errors incurred in using the commercial code as an auxiliary tool for an initial estimate of the drag-reduction performance of a new surface.

3.5.2.2 Specific Validation Test

In addition to the general comparison of current CFD work 1 to the data band generated from all available experimental results. A new validation test, CFD work 2, against the specific experimental result of Sawyer and Winter (1987) for the symmetric v-groove riblet surface is conducted to complement current validation work.

Nine different speeds of flow are implemented to cover a relatively broad range of s^+ value ranging from 8.7 to 41.9, which provides a fully picture of the trending. The absolute friction coefficients of the smooth surface and symmetric v-groove riblet for CFD work 2 are depicted in Table 3.6.

Table 3.6 Friction coefficients of smooth surface and symmetric v-groove riblet for CFD work 2

s^+	C_{f_Smooth}	C_{f_Riblet}	*DR%*
8.7	0.01500	0.01408	6.1%
11.9	0.01258	0.01166	7.3%
14.9	0.01113	0.01036	6.9%
17.8	0.01012	0.00950	6.1%
20.6	0.00940	0.00885	5.8%
26.1	0.00850	0.00801	5.7%
31.4	0.00789	0.00746	5.4%
36.7	0.00747	0.00712	4.6%
41.9	0.00716	0.00688	3.9%

The results of current CFD work 2 and experimental results obtained by Sawyer and Winter (1987) are well compared in Figure 3.6.

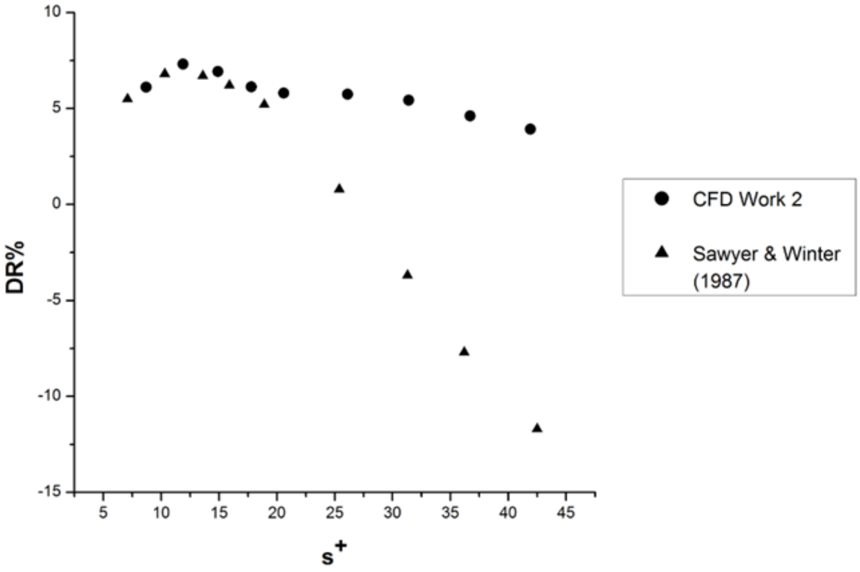

Figure 3.6 Comparison of current CFD work 2 and Sawyer & Winter (1987)

As shown above, current results of CFD work 2 shows similar trending as that of CFD work 1. Both of them indicate a good fit with the experimental result when s^+ is not much bigger than the optimum s^+ value. Concerning specific CFD work 2, it generally fits with the experimental results up to $s^+ = 17.8$.

It is essential to point out that, within the reach of the author's ability, no available experimental data of the absolute friction coefficient values of the symmetric v-groove riblet has been found. As a result, only the drag-reduction percentage of the past experiments are discussed and compared to the conducted numerical results. The absolute values of friction coefficient obtained from numerical results have also been presented for further study or comparison.

3.5.3 Velocity Profile

Besides the obvious drag reduction phenomenon caused by riblet structure, similar influences on the mean velocity profile, as indicated by Choi, Moin et al. (1993), are observed in present work and detailed including riblet induced velocity shift in the log layer and velocity variation in the spanwise direction.

- Riblet induced velocity shift in the log layer

As suggested by Hama (1956), the classical logarithmic law of the wall is reasonably modified by adding a new term $\mathrm{F}(\mathrm{h}^+)$, which represents the effects of surface roughness as shown in the equation .

$$\mathrm{u}^+ = \frac{1}{\kappa}\ln \mathrm{y}^+ + \mathrm{C}^+ + \mathrm{F}(\mathrm{h}^+) \tag{31}$$

The term $\mathrm{F}(\mathrm{h}^+)$ is generally mentioned as the sand-grain roughness at that time, but this formula has got a universal significance for both drag-increase and drag-reduction surfaces. It is found that $\mathrm{F}(\mathrm{h}^+)$ is negative for a drag-increase surface, and positive for a drag-reduction surface. The same outcome is also found in our simulation of the riblet channel validation test as shown below in Figure 3.7.

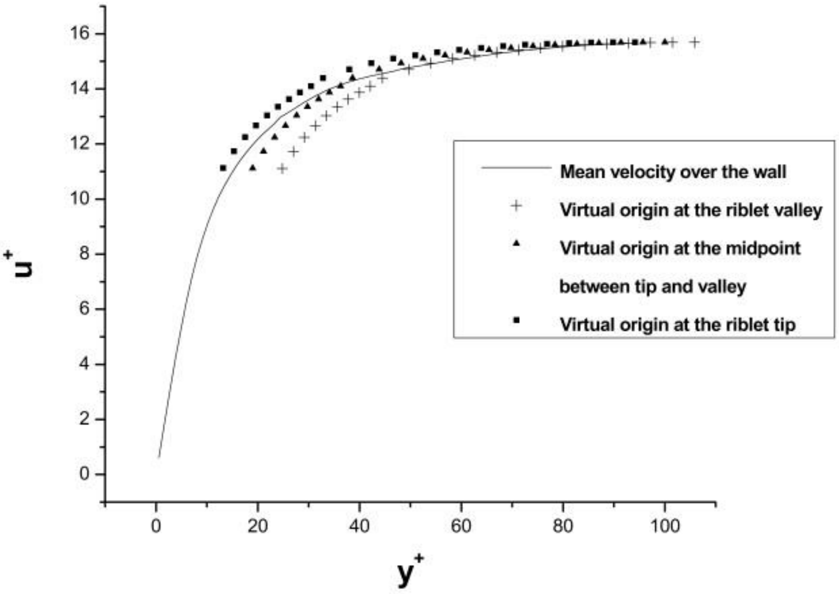

Figure 3.7 Plot of u^+ vs y^+ for flat wall and riblet wall with three different virtual origins

- Velocity variation in the spanwise direction

As shown in Figure 3.8, six points are selected from the rib valley to the rib tip with an equally spaced gap to depict the effect of different spanwise location on the mean velocity. It is found that the spanwise variation only occurs in the region close to the riblet and also the mean velocity above the riblet valley is larger than that above the riblet tip. The conclusion is consistent with previous experimental (Hooshmand, Youngs et al. 1983, Benhalilou, Anselmet et al. 1991) and numerical (Bechert and Bartenwerfer 1989) results.

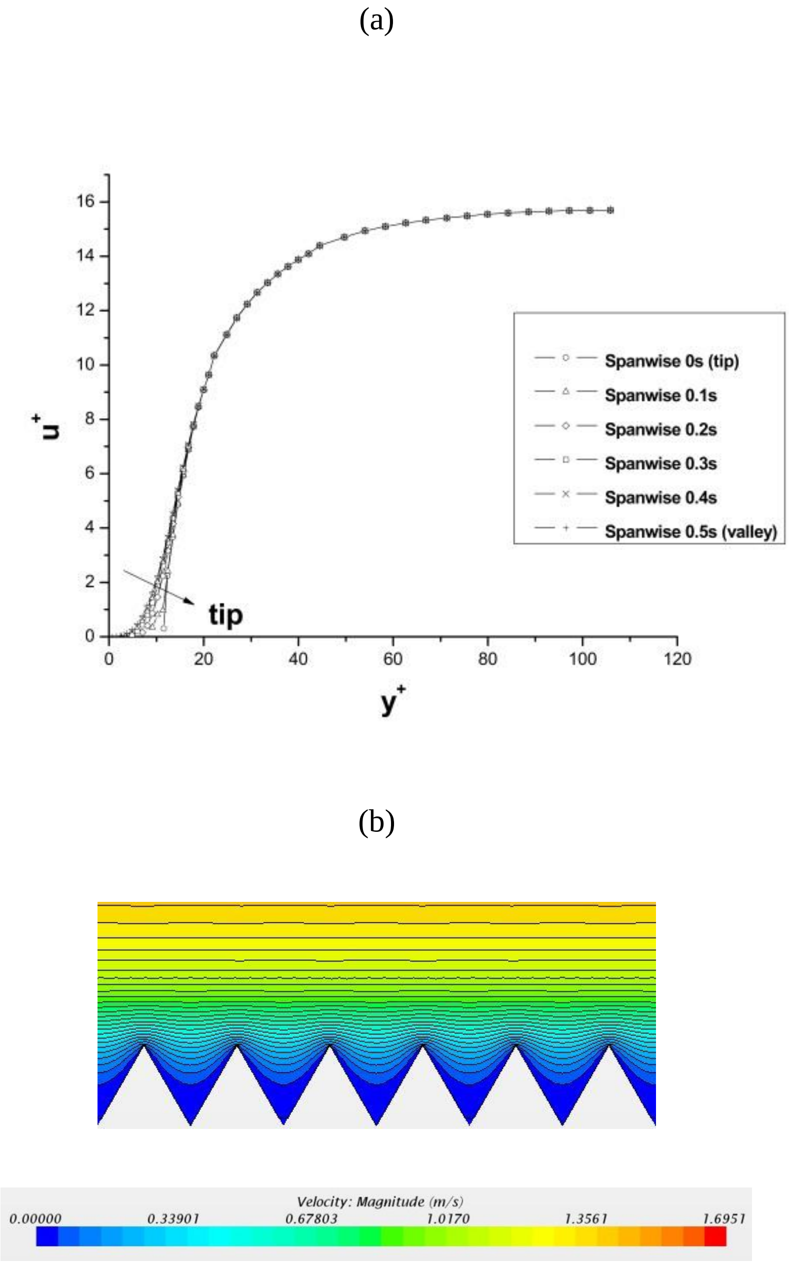

Figure 3.8 (a) Plot of u^+ vs y^+ at six different locations from riblet tip to valley (b) Contour of the mean velocity in the y-z plane

3.5.4 Turbulent Kinetic Energy & Wall Shear Stress

In this section, the impact of riblet on the near wall turbulent activities is reflected by the computed results of turbulent kinetic energy in the near wall region and wall shear stress of the riblet surface. Firstly, the computed profiles of normalized turbulence kinetic energy above the smooth surface, riblet trough, riblet crest are plotted in the wall-normal direction against y^+ as shown in Figure 3.9.

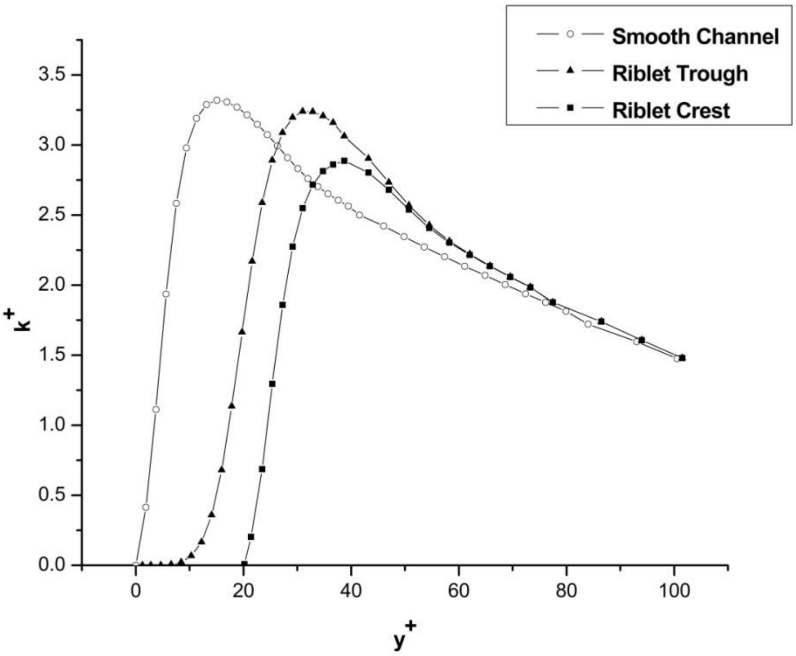

Figure 3.9 Computed profiles of normalized turbulence kinetic energy

It is important to clarify that the data is based on the numerical results of 60° V-groove riblet, which has a drag reduction percentage of 5.66% at $\mathrm{Re_m} = 5600$ when s^+ equals to 20.3 (8 ribs along the bottom surface). Moreover, the coordinate y^+ has its origin in the trough of the riblet for both crest and trough profiles.

As shown above, a steep rise in k^+ across the buffer layer is displaced to larger values of y^+, which indicates the thickening of this viscous affected sublayer. Besides that, the peak k^+ value above the riblet crest and riblet trough are separately 13.0% and 2.4% smaller than that above the smooth surface, which indicates an effective inhibition of the violent turbulent activities in the near wall region.

For a better understanding of the riblet drag reduction mechanism, the scalar scenes of both turbulent kinetic energy and wall shear stress at $s^+ = 20.3$ and $s^+ = 42.7$ are compared as shown in Figure 3.10 and Figure 3.11.

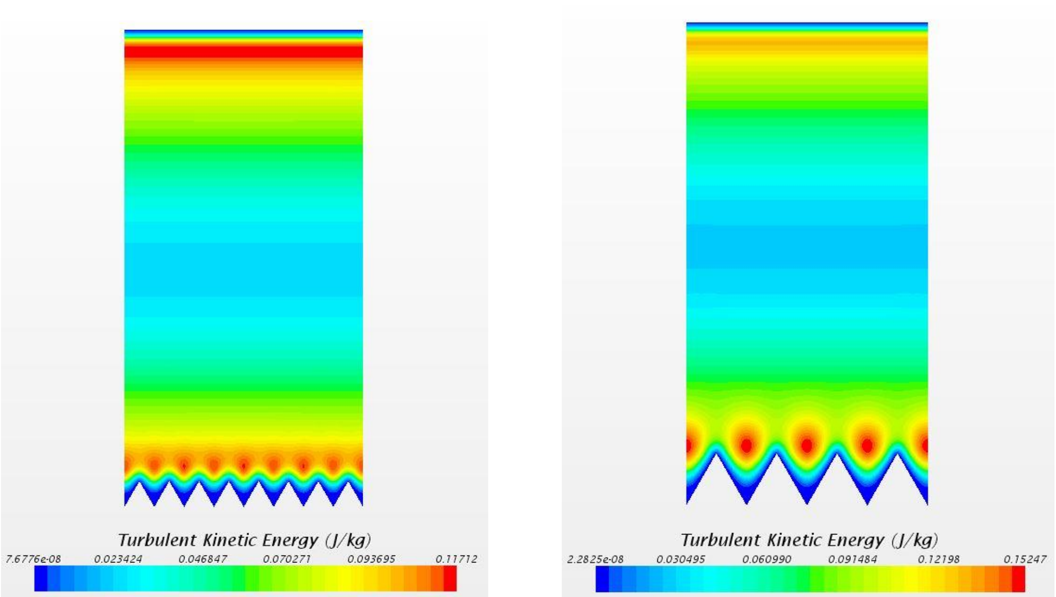

Figure 3.10 Turbulent kinetic energy distribution in the y-z plane of the channel for the case of s^{+}=20.3 (left) and s^{+}=42.7 (right)

(a)

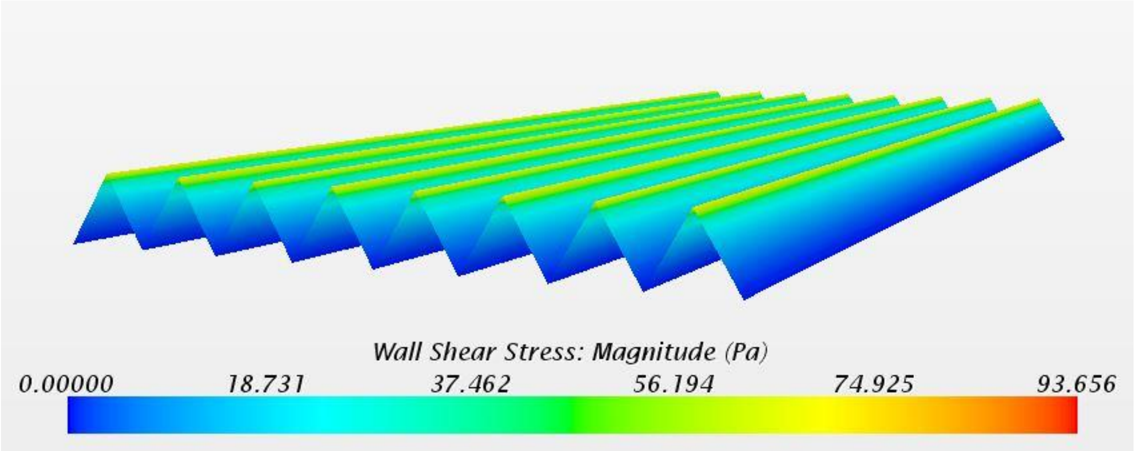

(b)

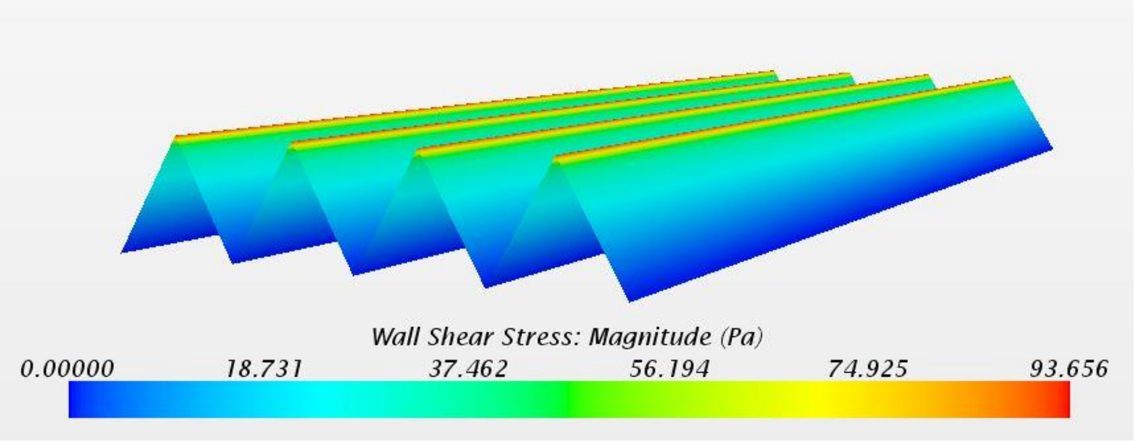

Figure 3.11 (a) Wall shear stress of riblet surface for the case of s^+=20.3; (b) Wall shear stress of the riblet surface for the case of s^+=42.7;

Compared to the TKE above the riblet, it is distributed uniformly in the spanwise direction above the top smooth surface for both cases as shown in Figure 3.10. Peak turbulent kinetic energy is found at $y^+ = 15$ above the smooth surface, but is displaced much further away from the wall above the riblet surface to the position of y^+=30-40.

The red contour above the riblet crest is the region where turbulent activities are the most violent. The representative turbulent coherent structures such as ejection, sweep, and vortical structure, which are responsible for the momentum transfer and thus the frictional resistance in the near wall turbulent region, are mostly found here. Unlike the uniformly distributed turbulent kinetic energy above the smooth surface, the spanwise velocity fluctuation is inhibited due to the existence of riblet. For the case of $s^+ = 20.3$, a weakening effect of the turbulent activities in the buffer layer could be observed if we compare peak values of turbulent kinetic energy above riblet surface and smooth surface. Moreover, the violent turbulent activities are found some distance above the riblet crest. For the case of $s^+ = 42.7$, the weakening effect of the turbulent activities cannot be found any longer and the violent turbulent activities are found to partly fall inside the grooves.

The result of the downwards movement of violent turbulent activities is much clearly seen in Figure 3.11. For the same scalar field, the riblet surface for the case of $s^+ =$

42.7 exhibits a larger area of high wall shear stress. The wall shear stress at the tip region for the case of $s^+ = 42.7$ is also bigger, which is concluded as the result of stronger and downwards movement of turbulent activities.

3.6 Summary

This chapter acts as an essential preparation step for the investigation of the new design surface. The specific RKE 2L turbulence model has been examined by simulating the traditional symmetric v-groove riblet surface in a fully-developed turbulent channel flow. The impact of surface topography on the near-wall turbulent boundary layer is reflected by the change of skin friction, mean velocity profile, turbulent kinetic energy. Although the calculated results of the riblet's drag-reduction performance are generally in accord with the measurements of the summarized experimental data band, the riblet frictional drag is overestimated when s^+ exceeds the optimum value due to the lack of secondary turbulent motions which is supposed to sweep the riblet surface at a high speed and thus deteriorates the drag-reduction performance. Although current RANS result could only partly reflect the drag-reduction performance of riblet, it is still economical (less computational time compared to DNS) and acceptable to use it as an auxiliary tool for an initial estimate of the drag-reduction performance of a new surface.

4. Numerical Investigation of the New Design Surface

4.1 Introduction

Based on the results derived in Chapter 3, the numerically validated RKE 2L turbulence model is used to study the impact of the new surface topography on the near-wall turbulent activities and to answer the following questions:

- Does new design surface possess any drag reduction property?
- What is the optimum design of the new surface topology?
- Is the existence of riblet discontinuity beneficial or harmful to its drag-reduction performance?
- Does new design surface have fouling-control potential?

In section 4.2, the new design surface is proposed based on two existing surface technologies: riblet surface and Sharklet AF^{TM} surface, where detailed surface pattern is highlighted.

In Section 4.3, the geometrical specifications of the new design surface are firstly depicted, after which the essential numerical setup such as the computational domain of the channel and boundary conditions is introduced. Finally, the mesh independence test is conducted to determine the suitable mesh refinement based on the turbulent statistics sensitivity to the grid resolution.

In Section 4.4, a preliminary CFD test is carried out to assess the potential drag-reduction properties of the new surface pattern. Besides the direct monitoring of the skin friction, the variation of the mean velocity in the wall-normal direction and spanwise direction is also derived to examine the surface topography's impact on the near wall turbulent activities. Subsequently, a more systematic parametric study is conducted to explore the new surface pattern's impact on near-wall turbulent activities. Several parameters such as bulk flow velocity, rib height, and rib spacing, are independently varied to understand their effects on the drag-reduction performance, and finally the best performing configuration is highlighted based on these considered in the parametric study. Finally, additional CFD simulations of the spaced v-groove riblet or trapezoidal riblet are run to investigate if the existence of riblet discontinuity is beneficial or harmful to its drag-reduction performance.

In Section 4.5, the summary of this chapter is given.

4.2 Geometry of New Design Surface

As mentioned in Chapter 1, the aim of the work is to propose a new design surface which is expected to possess both drag-reduction and fouling-control performance that could be incorporated into ship coating system. Subsequently, two existing surface technologies: riblet surface and Sharklet AF^{TM} surface are critically reviewed in Chapter 2 that inspires the author to come up with the idea of the new surface. For the proposed new surface, the traditional triangular rib structure that exhibits good drag reduction performance is employed and arranged with specific streamwise length, offset and gap, which imitates the surface complexity of the Sharklet AF^{TM} fouling-control surface. Similar to the application of riblet structure, the direction of the new design surface should be aligned with the direction of water flow and is expected to be longitudinally painted on the underwater ship hull surface. The unique new design surface is similar to dermal denticles found on fast-swimming shark skin and the size of the ribs vary at different conditions (ship length, ship speed, etc.), generally lying between the range of 10µm and 100µm.

To be more specific, the new surface consists of four different sizes of ribs ($\frac{8}{3}$s, 2s, $\frac{4}{3}$s, $\frac{2}{3}$s) with an equal offset and gap of $\frac{1}{3}$s. Take the first column for example, the largest rib is located at the centreline, and rib size decreases from the middle to two sides. If the first column is regarded as a basic unit, the new surface could be regarded as assembling of repeated basic units with every second column transformed by a distance of 3s. A detailed specification of the new design surface is shown in Figure 4.1.

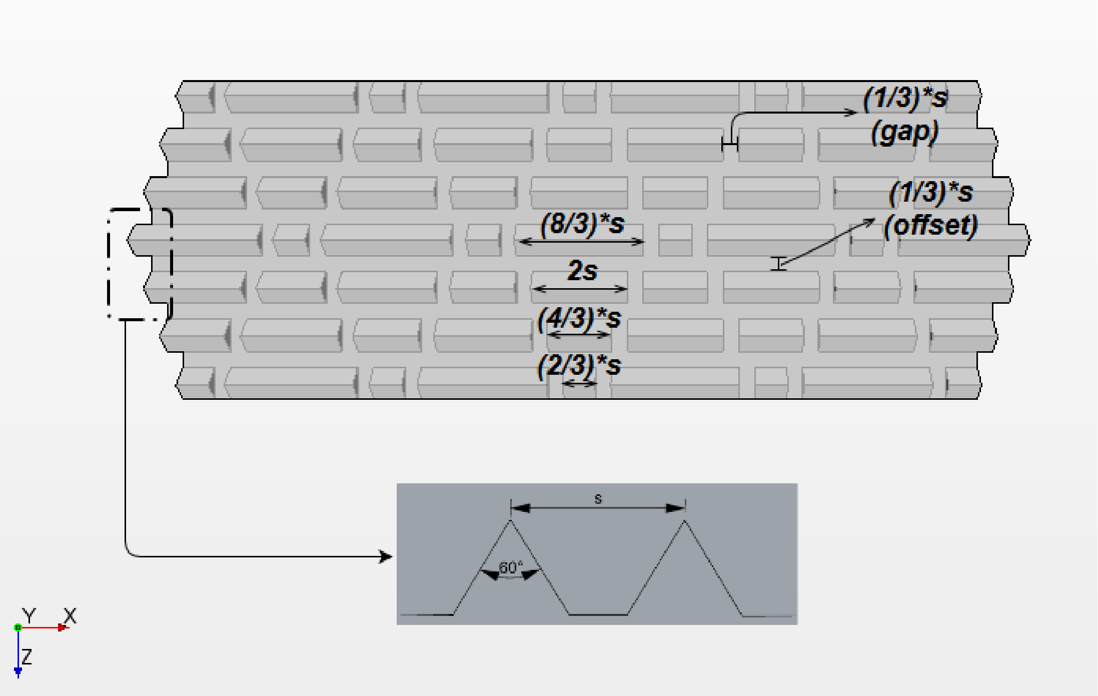

Figure 4.1 Specification of the new design surface

Although the proposed surface is designed to have the anti-fouling performance, due to the unavailability of proposed surface manufacturing within the author's reach in terms of cost and capability, it is currently unavailable to conduct laboratory fouling assays, field immersion tests, or even in-service anti-fouling demonstration. Nevertheless, the existing experimental barriers do not impede the author to make preliminary anti-fouling predictions based on the calculated CFD results (wall shear stress) and previous findings of anti-fouling technologies. Inevitably, more calculations of the new design focus on the drag-reduction performance but experimental research on the fouling-control performace is expected to be done in the future.

4.3 Numerical Study of New Design Surface Hydrodynamic Performance

4.3.1 Numerical Preparation

4.3.1.1 Model Setup

For a more practical aim of the study, the size of triangular ribs is selected to offer good drag-reduction performance at the speed of 15 knots, at which many ocean-going ships are operated. As a result, the size of the computational box will have a smaller physical value but the non-dimensional length in streamwise, spanwise and wall normal directions will still be kept in a plausible range and also the conclusion of minimal flow unit suggested by Jimenez and Moin (1991) is satisfied in these simulations. Similarly, the computational box, as shown in Figure 4.2 consists of six faces: top smooth surface (no-slip wall), bottom new design surface (no-slip wall), left symmetry plane (symmetry), right symmetry plane (symmetry), inlet face (velocity inlet), and outlet face (pressure outlet). The periodic boundary condition is implemented in both streamwise and spanwise directions with specific mass flow rate.

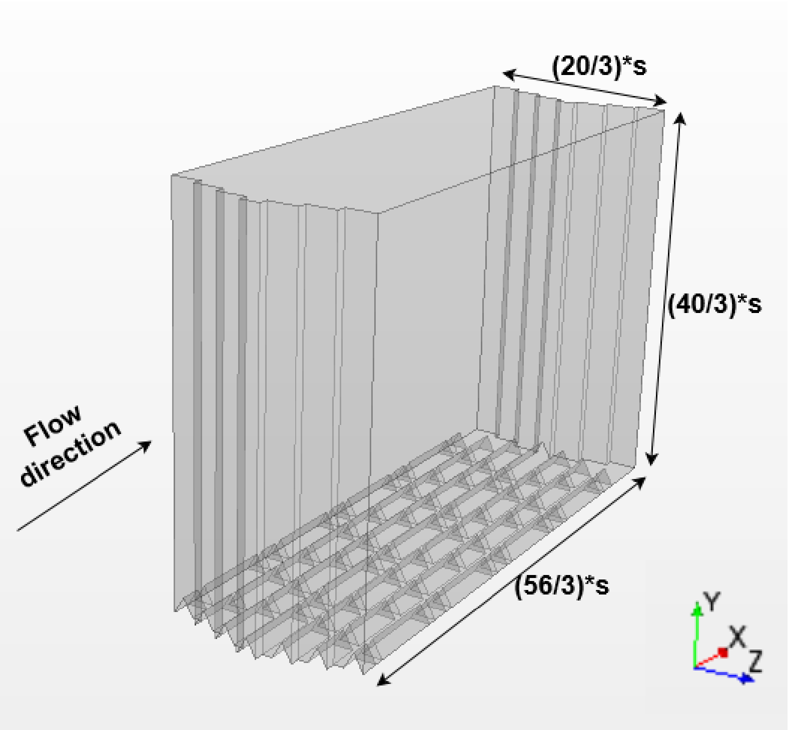

Figure 4.2 Computational box of the new design surface channel

Similar to Section 3.4.3, the entire channel is still split into five independent volumes at three levels of refinements. The isotropic and structured mesh is used at each volume, while the finest mesh is applied in the near wall region (around 2 riblet height) in order to capture the near turbulent activities. As the distance from the wall increases, the lower requirement of the mesh is needed and thus two other refinement levels are specified for the aim of reducing computational time. The non-dimensional values of Δx^{+} are separately 1.88, 3.76, 7.52 from the finest level to the coarsest level, which is the same as the riblet validation test mentioned in Chapter 3.

4.3.1.2 Mesh Independence Test

Similar to Section 3.4.3.1, mesh independence test is conducted here again for the turbulent channel flow covered with new design surface. Simulations of three mesh refinements are carried out to determine the turbulent statistics sensitivity to the grid resolution. The grid refinement factor, r, is chosen to be $\sqrt{2}$. Results calculated by the CFD simulations are shown in Table 4.1.

Table 4.1 $C_{f\_new\ surface}$ results at three mesh refinements for new design surface channel at Re=9529

Mesh refinement	Total No. of Cells	Computational Cost (Core hours)	$C_{f\_new\ surface}$
Coarse	5.23×10^{5}	336	0.007125
Medium	1.54×10^{6}	438	0.007129
Fine	3.76×10^{6}	1008	0.007096

Notes: It should be noted that the computational time consumed in the coarse mesh is calculated based on private PC rather than HPC, with 8 cores of Intel Core i7-3770 CPU.

As shown in Table 4.1, all solutions of three selected mesh refinements do not vary significantly. In the perspective of CFD problem's accuracy, increasing the number of mesh cell is always beneficial to the solution accuracy. However, an additional comparison is made here, which is similar to what is conducted in Section 3.4.3.1, between numerical results and empiric formula in terms of top smooth plate, as shown in Table 4.2

Table 4.2 C_{f_smooth} results at three mesh refinements for new design surface channel at Re=9529

Mesh refinement	Total No. of Cells	C_f (CFD)	C_f (Dean 1978)	Absolute Difference (%)
Coarse	$5.23 * 10^5$	0.007465	0.007442	0.31%
Medium	$1.54 * 10^6$	0.007477	0.007442	0.47%
Fine	$3.76 * 10^7$	0.007453	0.007442	0.15%

Dean's empiric correlation: $C_f = 0.073 * Re^{-0.25}$

As shown in Table 4.2, the difference between numerical results and empiric formula generally becomes smaller as mesh is refined although it experiences a slight fluctuation for the medium mesh refinement. However, the difference for the fine mesh is negligibly small, which is only 0.15%. As a result, fine mesh refinement is chosen for new design surface channel flow simulations due to its relatively good accuracy and acceptable computational cost. The mesh of the new surface computational domain is shown in Figure 4.3.

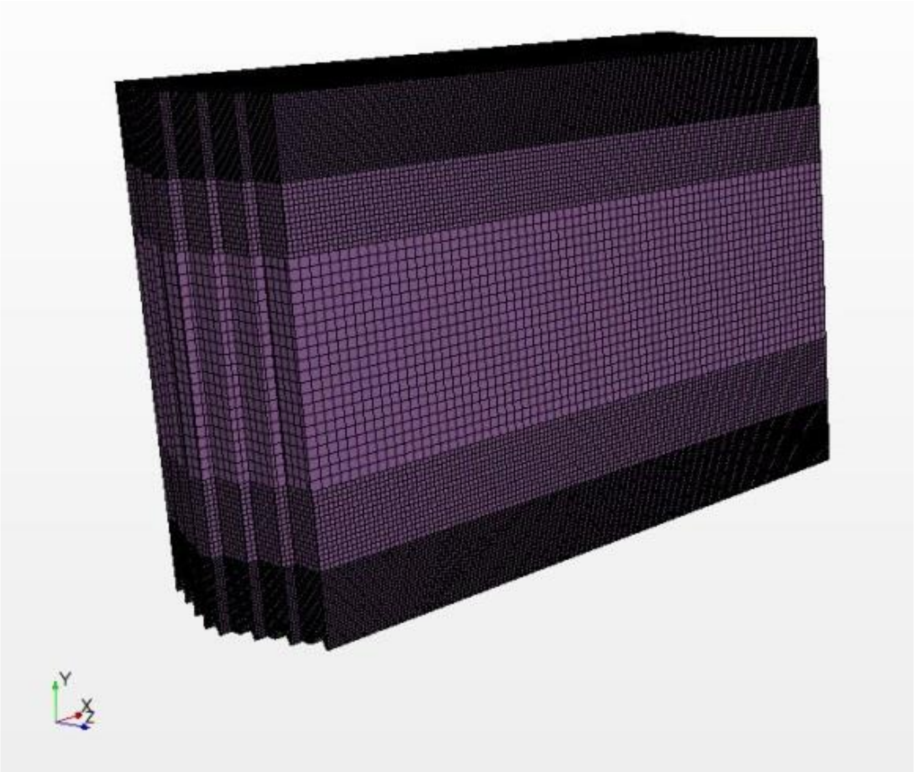

Figure 4.3 Computational mesh of new design surface channel

4.3.2 Numerical Results

4.3.2.1 Preliminary Study of the New Surface Pattern

Inspired by the diamond surface pattern of Sharklet AF^{TM} technology, the new surface is structured in the same way while every single rib is replaced by a triangular riblet structure that possesses drag-reduction property. To some extent, the new design surface could be regarded as a discontinuous form of trapezoidal riblet structure. However, the drag-reduction performance of the new surface is still questionable due to the discontinuous feature in the flow direction, and thus will be examined here with the aforementioned validated numerical method.

An initial attempt is made here to assess the drag-reduction performance of the new design surface. The bulk speed of 7.72 m/s (or 15 knots) is specifically chosen, at which many ocean-going ships are operated. Subsequently, the friction velocity of the flat plate is calculated based on Dean's empiric correlation. Using the calculated result of flat plate friction velocity, the rib spacing is actively adjusted to ensure the predicted s^+ value is near to the s^+ value of trapezoidal riblet at which max drag-reduction performance is reached. The optimum value of s^+ is found from the work of Bechert (1997), which are approximately 20 wall units. Following this procedure, the basic dimension of the new surface pattern is confirmed. The validated engineering turbulence model, as indicated in chapter 4, is used here to investigate the new surface pattern. The information of the CFD test is shown in Table 4.3.

Table 4.3 Information and results of the preliminary new surface simulation

CFD simulation information			
Rib spacing (s)	Rib height (h)	Bulk Velocity (U)	Rib Angle (α)
45 μm	26 μm	7.72 m/s	60°
Results			
s^+	h^+	*DR%*	
23.84	13.77	6.22%	

As shown in Table 4.3, when compared to the skin friction of the top flat plate, an initial drag-reduction result of 6.22% is obtained for the new design surface at $s^+ = 23.84$, which is near to the optimum s^+ value of trapezoidal riblet. As mentioned in Chapter 4, the drag-reduction results of the symmetric v-groove riblet surface is generally in agreement with the past experimental results, Thus, using the same engineering turbulence model and computational setup, the darg-reduction performance of the new surface pattern could be preliminarily assumed at this stage. In the later section of 4.3.2.2, a more systematic parametric study will be conducted to examine the drag-reduction performance of the new design surface.

Mean Velocity Profile

Besides the direct observation of the skin friction of the new design surface, the drag reduction property could also be reflected in the change of mean velocity profile across the channel, which will be discussed next from two aspects: upward shift of mean velocity and velocity variation in the spanwise direction.

- ***Upward Shift of Mean Velocity***

The impact of surface roughness on the mean velocity profile of the turbulent flow over a flat plate is represented as $F(h^+)$ as suggested in Eq.11. The value of this additional term for the log law velocity is positive for the drag-reduction surface, and negative for the drag-increasing surface. As indicated by Choi, Moin et al. (1993), there is no consensus on the selection of virtual origin from the experience of previous experimental studies. Thus, the profiles of the mean velocity based on three different virtual origins (rib tip, rib valley, the midpoint between tip and valley) are calculated and shown in Figure 4.4. The law of the wall is also presented in the plot as the reference line of a smooth surface.

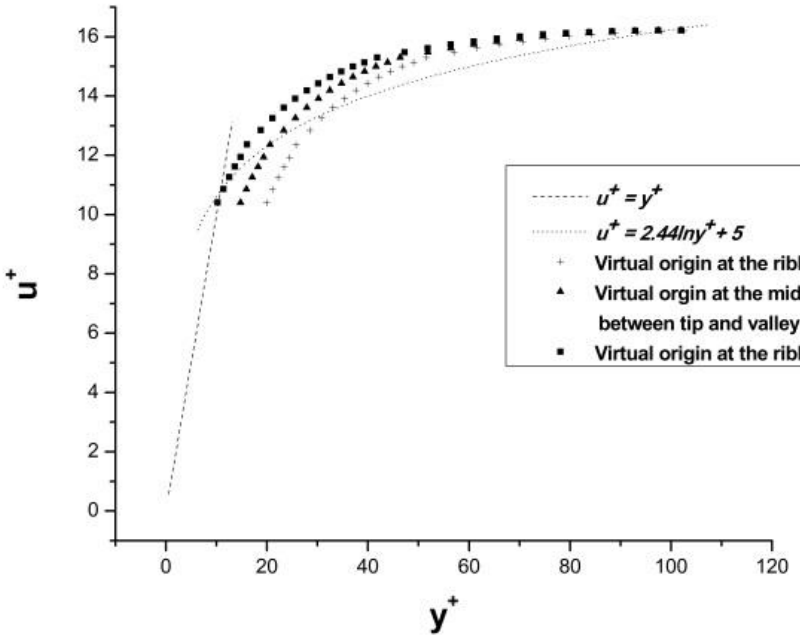

Figure 4.4 Comparison of mean velocity profile with different virtual origins and law of the wall

The upward shift of the mean velocity profile is observed at three different virtual origins, which validates the drag-reduction effect of the new design surface. The upward shift is found to start at a vertical position of 12, 22, 32 wall units respectively for cases of rib tip, midpoint, and rib bottom respectively. However, these lines collapse into one as y^+ becomes larger, which is due to the geometric restriction of internal channel flow.

- ***Velocity Variation in the Spanwise Direction***

Similarly, the velocity variation of the new surface in the spanwise direction is investigated in this study. Since the cross-section geometry of the new surface (trapezoidal) is different from that of triangular riblet surface (triangular), 4, rather than 6, different spanwise locations, spaced by $\frac{1}{6}$ s, are selected along the surface from the rib tip to the middle point of rib valley. The plot of u^+ vs y^+ at four different spanwise locations in the near-wall region is depicted in Figure 4.5.

(a)

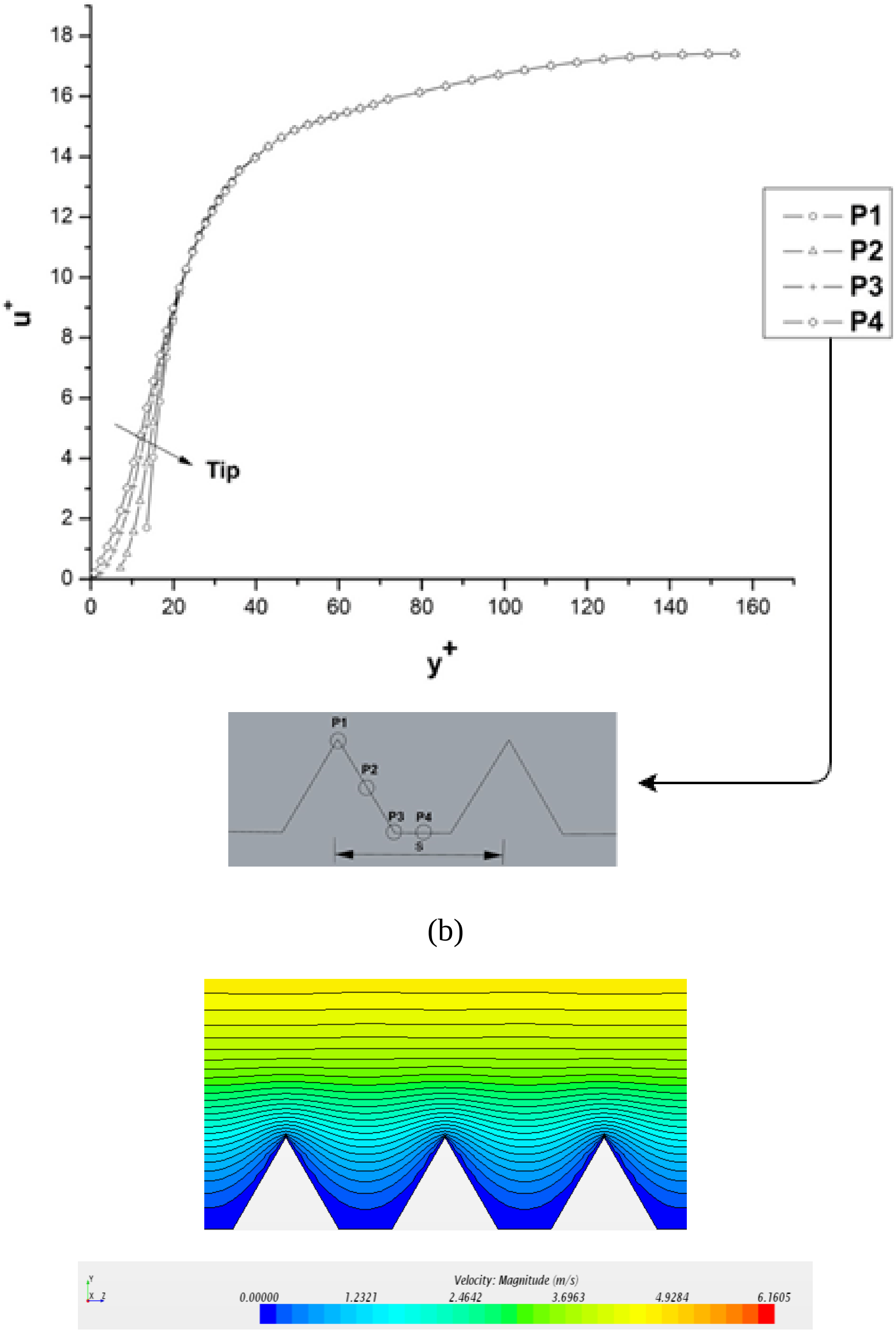

Figure 4.5 (a) Plot of u^+ vs y^+ at four different spanwise locations (b) Contour of the mean velocity in the y-z plan

As shown in Figure 4.5, the impact of the surface topology is confined to the near wall region approximately two rib heights away from the valley, where y^+ is smaller than 30. It is found that the velocity gradually decreases in the spanwise direction from P1 to P4 at the same y^+ value, where y^+ is smaller than 30 (surface topology affected region). It is obviously noticed from Figure 4.5 (b) that the velocity gradient at the rib peak (Ex: P1) is much larger, and therefore larger skin friction at rib peak. However, the velocity gradient in the rib valley (Ex: P2, P3) is much smaller and even approaches to 0 at the bottom of the rib valley (Ex: P4). This result is consistent with the findings of Hooshmand, Youngs et al. (1983), who reported 10-15 % increase in the velocity gradient at the riblet peak and 40% reductions in the valley for a triangular riblet surface. Compared to the smooth surface, the skin friction of the new surface topography is a balance between drag penalty caused by an increased wetted surface area and drag reduction caused by low-speed fluid in the rib valley.

4.3.2.2 Parametric Study

The new design surface has two fluid parameters (velocity U and viscosity ν) and four rib parameters (spacing s, height h, gap, and offset). The effect of viscosity is not discussed here because seawater is the only fluid in contact with seagoing ships. The values of rib gap and rib offset are preserved because this specific topography inspired by Sharklet AF^{TM} is expected to possess fouling-control property. As a result, only one fluid parameter (velocity U) and two rib parameters (spacing s, height h) are independently changed to investigate the new design surface. The information of all test cases is shown in following tables.

Table 4.4 Information of parametric study of velocity

	Case No.	*s* *(μm)*	*h* *(μm)*	Rib Angle	Velocity *U* *(m/s)*
Baseline	**1**	**45**	**26**	**60°**	**7.72**
Effect of U	2				1.29
	3				2.57
	4				5.14
	5				10.29
	6				12.86
	7				15.43
	8				18.00
	9				20.58

Table 4.5 Information of parametric study of rib height

	Case No.	*s* *(μm)*	*h* *(μm)*	Rib Angle	Velocity *U* *(m/s)*
Effect of h	1	45	26	60°	7.72
	10	45	15	90°	7.72
	11	45	8.7	120°	7.72

Table 4.6 Information of parametric study of rib spacing

	Case No.	*s* *(μm)*	*h* *(μm)*	Rib Angle	Velocity *U* *(m/s)*
Effect of s	6	21	26	30°	7.72
	7	45	26	60°	7.72
	8	78	26	90°	7.72
	9	135	26	120°	7.72

Effect of Velocity

Considering the geometric similarity of new design surface to trapezoidal riblet and riblet structure drag-reduction mechanism, it is assumed that drag-reduction result will be obtained at roughly the same range of s^+ value if there is any. To the best of the author's knowledge, the most frequently studied range of s^+ value is up to 50 – 70 wall units. In this study, nine different speeds are implemented so that a broad s+ range from 6.0 to 54.3 wall units is covered.

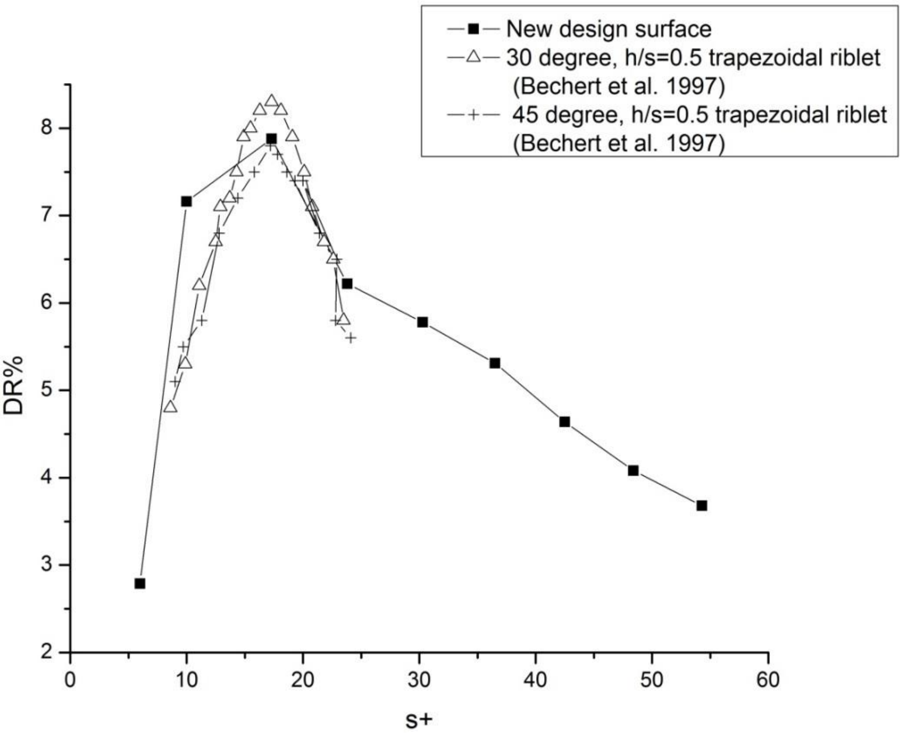

Figure 4.6 Comparison of the current study and several representative riblet structures

The possibility of imperfect prediction beyond the optimum s^+ value has been pointed out in section 3.5.2, and the calculated new surface results generated by the same numerical method indicate an identical problem as well as s^+ exceeds 25. However, a relatively good drag-reduction estimate could be well reproduced when s^+ is smaller than the optimum value. Based on the feature of the current numerical method, the new design surface is deduced to possess drag-reduction ability. The peak performance (7.88% drag reduction) of the new surface is achieved at s^+=17.3. Probably due to the similarity in geometry, a generally similar trend is obtained for the new surface compared to that of trapezoidal riblet surface. Although a good drag-reduction percentage has been numerically predicted for the 60° the new surface, its drag-reduction performance might be further optimized if a parametric study is conducted in terms of rib angle. Different from trapezoidal riblet, the effects of the gap and offset between different ribs will not be considered, because the specific pattern inspired by Sharklet technology should be maintained to preserve fouling-control potential.

For a better understanding of the topography effects on the near wall turbulent activities, four representative cases (Case 1, 4, 5, 6) are selected for a more detailed investigation. Firstly, the distribution of the normalized turbulent kinetic energy (k^+)

in the wall normal direction has been presented at various non-dimensional rib spacings (s^+) as shown in Figure 4.7.

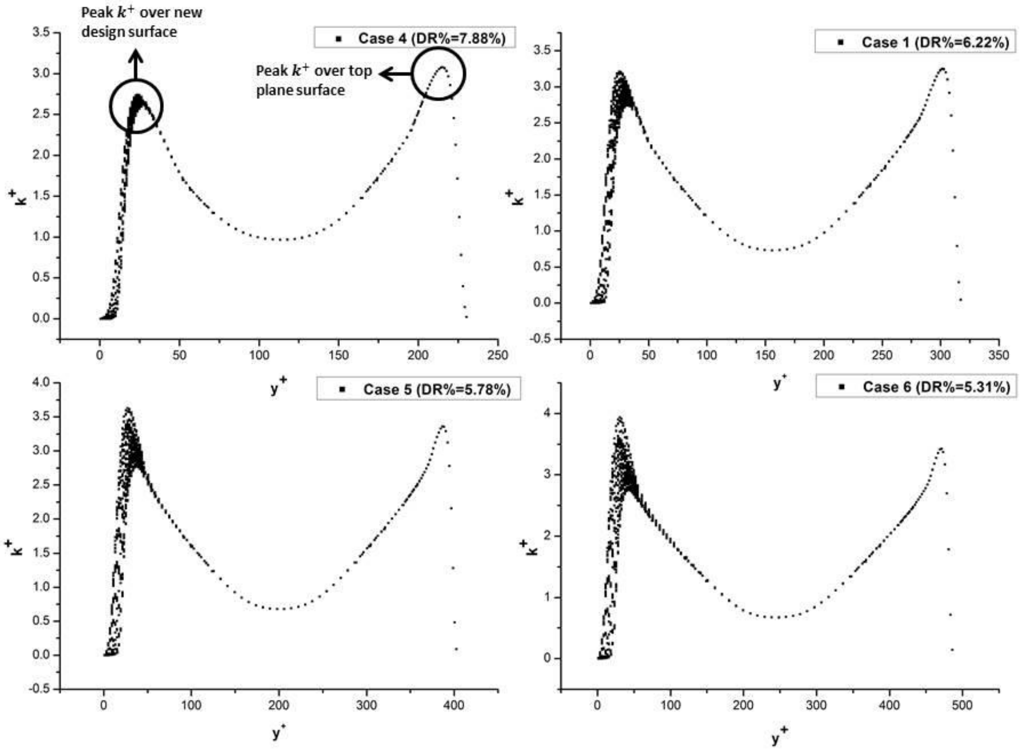

Figure 4.7 Plot of k^+ vs y^+ in the y-z plane; Case 4: $s^+=17.3$, DR%=7.88%; Case 1: $s^+=23.8$, DR%=6.22%; Case 5: $s^+=30.3$, DR%=5.78%; Case 6: $s^+=36.5$, DR%=5.31%

As shown in Figure 4.7, the left and right peak respectively represents the peak k^+ over the new design surface and the top plane surface. The inhibition of the momentum transfer in the near wall region is most apparent in case 4, where the peak k^+ value is obviously smaller above the new design surface rather than a smooth surface. As s^+ becomes bigger, it is found that the data points gradually become more dispersive and also the peak k^+ value above the new design surface gradually approaches that above the smooth surface. This tendency is likely to be caused by the degradation of the surface drag reduction performance.

For a better understanding of the problem, a comparison between the peak k^+ value above two surfaces is shown quantitatively in Table 4.7, and the scalar scenes of turbulent kinetic energy for Case 1, and Case 4-6 are shown in Figure 4.8.

Table 4.7 Comparison of a new and smooth surface in terms of peak k^+ value and position

Case No.	$(y/h)_{new}$	$(y/h)_{smooth}$	k^+ difference
4	2.37	1.56	14%
1	1.79	1.21	12%
5	1.56	0.98	11%
6	1.44	0.75	9%

Note: $(y/h)_{new}$ *represents the ratio of the wall-normal position of peak* k^+ *value above the new design surface;* $(y/h)_{smooth}$ *represents the ratio of the wall-normal position of peak* k^+ *value above the smooth surface;* $k^+\ difference$ *is the difference of peak* k^+ *between new surface and smooth surface.*

Due to the existence of the surface structure, it is found that the buffer layer is thickened and the peak k^+ value occurs further away from the wall compared to the smooth surface. The mean value of k^+ is calculated based on the data of the x-z plane at the height y_{new} and y_{riblet} (where peak k^+ value is reached). The decrease of k^+ difference compared Case 1 and Case 4-6 and indicates a weaker inhibition of near wall turbulent activities and thus less drag reduction percentage.

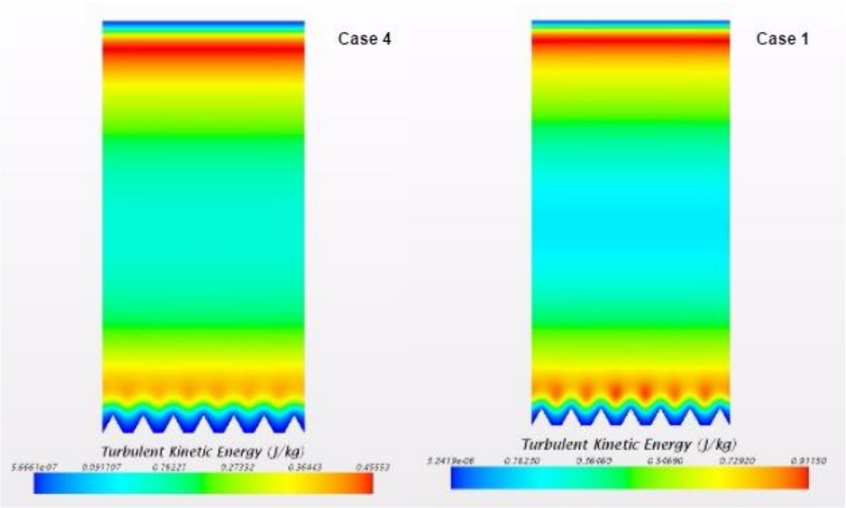

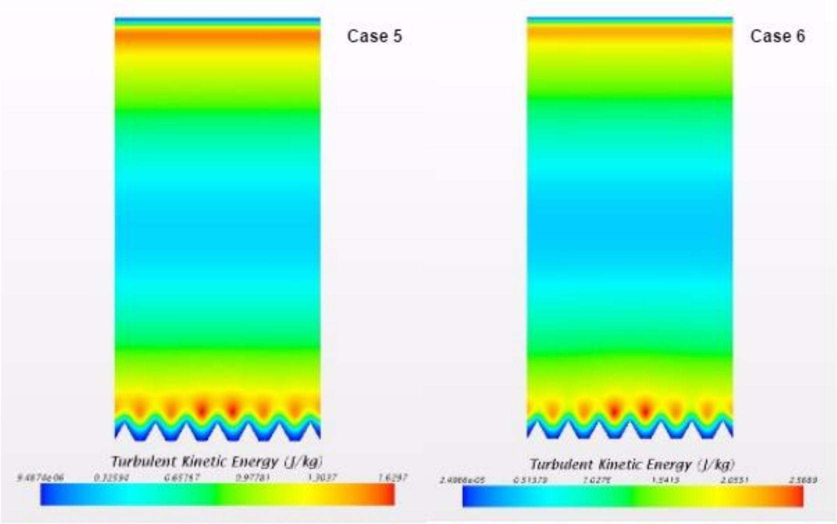

Figure 4.8 Scalar scenes of turbulent kinetic energy for Case 1, and Case 4-6

The inhibition impact of new surface topography on the near wall momentum transfer is much clearly seen here. It is observed that the violent turbulent activities are well repelled from the rib tip in Case 1, but this performance is deteriorated as nondimensional rib spacing becomes bigger. As the violent turbulent activities gradually approach the rib tip, the riblet surface is partly exposed to high-speed vortical structures and thus gives rise to a weakening drag reduction performance.

Effect of Rib Height

In this section, the rib height will be varied independently and the rib spacing is kept the same as the baseline value. All cases are carried out in the same computational domain and at the same bulk velocity as detailed in Table 4.8.

Table 4.8 Effect of rib height on new surface drag reduction performance

Effect of rib height			
Case No.	h^+	s^+	*DR%*
1	13.8	23.8	6.22%
10	7.8	23.6	5.67%
11	4.5	23.4	3.52%

As shown above, the drag reduction performance deteriorates as the value of h^+ becomes smaller. The decrease of rib height leads to a shallower groove which might not effectively inhibit the lateral motion of velocity fluctuation in the near wall region. However, the deterioration is still not big enough to compensate for the fairly low wall shear stress in the groove surface, and thus only a weakened drag reduction performance is obtained in Table 4.8. Moreover, for a more direct insight into the rib height effect on the near wall turbulent activities above the new design surface, scalar scenes of turbulent kinetic energy for above cases are also shown hereby in Figure 4.9.

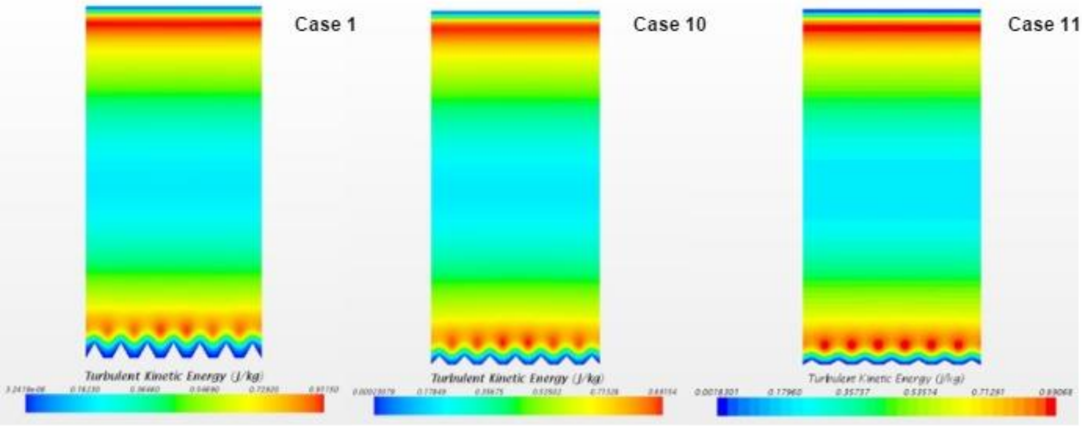

Figure 4.9 Scalar scenes of turbulent kinetic energy for Case 6, Case 11-12

The weakening effect of turbulent activities in the near wall region arising from the reduction in rib height is shown in Figure 4.9 through the increase of peak turbulent kinetic energy value or smaller inhibition impact on the spanwise velocity fluctuations as rib height gradually decreases. This phenomenon is also in support of the conclusion drawn from Table 4.8.

Effect of Rib Spacing

Following the investigation of rib height effect, the effect of rib spacing is discussed here for a systematic understanding. Similarly, the rib spacing is varied independently with rib height kept as the same as the baseline value. Due to the change of rib spacing, our computational domain also needs to be changed accordingly in the spanwise direction to preserve the complete surface topography (7 ribs in the spanwise direction). However, channel height and bulk velocity are kept the same as baseline case for a reasonable comparison between each other. The results of all test cases are shown in Table 4.9.

Table 4.9 Effect of rib spacing on new surface drag reduction performance

Effect of rib spacing			
Case No.	h^+	s^+	*DR%*
12	13.3	10.8	8.53%
1	13.8	23.8	6.22%
13	13.8	41.6	2.05%
14	13.9	72.3	-0.43%

For a constant and optimum h^+ value, the test case of smaller s^+ exhibits better drag reduction performance. The relatively narrower grooves make it harder for streamwise vortices (diameter = 20-30 wall units) to fall into the grooves. For larger s^+ cases, the ability to repel the streamwise vortices becomes weaker, and finally the low wall shear stress over the grooves is not enough to compensate for the increased drag cause by the relatively high speed streamwise vortices and drag increase result is obtained. The scalar scenes of turbulent kinetic energy for different cases are shown in Figure 4.10 to reflect the rib spacing effect on the near wall turbulent activities.

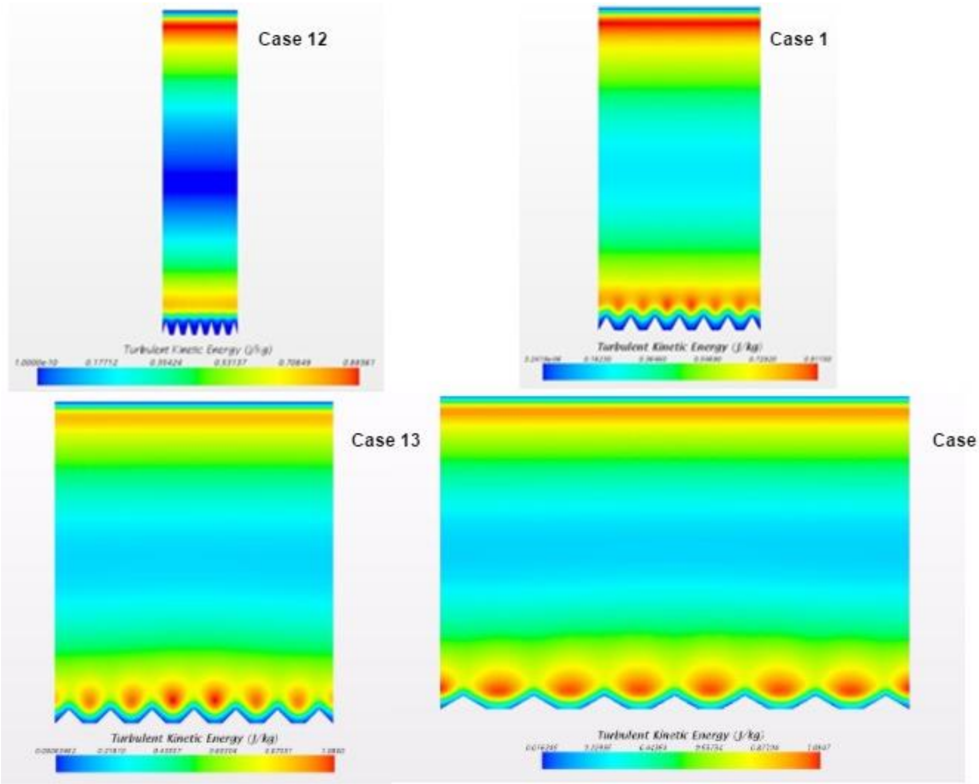

Figure 4.10 Scalar scenes of turbulent kinetic energy for Case 1, Case 12-14

The effect of rib spacing is mainly to restrict the streamwise vortices at or above the tip of the ribs, which effectively reduce the exposure area of groove surface to relatively high-speed streamwise vortices and thus reduce the skin friction. As shown in Figure 4.10, an obvious downward movement of violent turbulent activities is observed from some distance above the rib tip to the middle point of the grooves as rib spacing changes from the smallest value to the largest. Moreover, if the peak turbulent kinetic energy above the top smooth plate and bottom new surface are compared, it will be found that the lateral inhibition effect induced by the rib becomes weaker as well.

4.3.2.3 Effect of Geometry Discontinuity

The reference lines shown in Figure 4.6 are geometrically similar to that of the new design surface but still differ in two aspects: rib angle and streamwise discontinuity of ribs. As indicated by Bechert, Bruse et al. (1997), the influence of rib angle on the resulted drag reduction percentage is almost negligible and is thus not studied here. However, the streamwise discontinuity of ribs will be studied to understand the impact on the drag reduction performance. As a result, continuous 60° trapezoidal riblet of the same rib size as the new design surface is tested at various speeds to explore the overall performance at a relatively broad s^+ range. The details of the supplementary tests are indicated in Table 4.10 and Figure 4.11.

Table 4.10 Results of 60-degree trapezoidal riblet at various speeds

Velocity *U* (m/s)	h^+	s^+	*DR%*
2.57	5.7	9.9	6.62%
5.14	9.9	17.1	7.28%
7.72	13.6	23.5	5.47%
10.29	17.2	29.8	5.05%

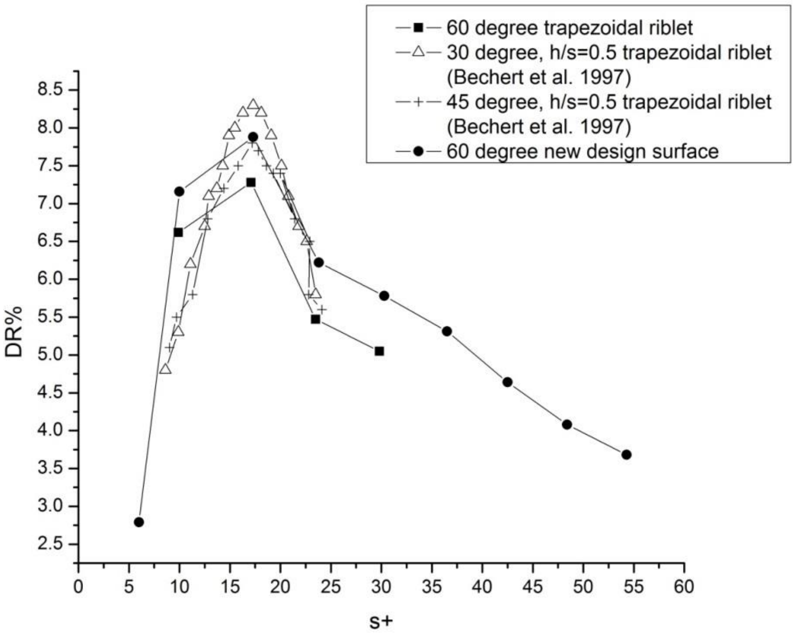

Figure 4.11 Effect of streamwise discontinuity on the new design surface

The calculated results indicate a maximum drag reduction percentage of 7.28% at $h^+=9.9$ and $s^+=17.1$. Using the same numerical method, the peak drag-reduction performance of the trapezoidal riblet is approximately 0.6% worse than the new design surface. The superior performance of the new design surface is deduced to benefit from its unique streamwise discontinuous pattern, which is expected to have a smaller surface area exposed to relatively high-speed flow and thus smaller skin friction. Such an impact can be clearly observed in the scalar scene of wall shear stress of two surfaces, as shown in Figure 4.12.

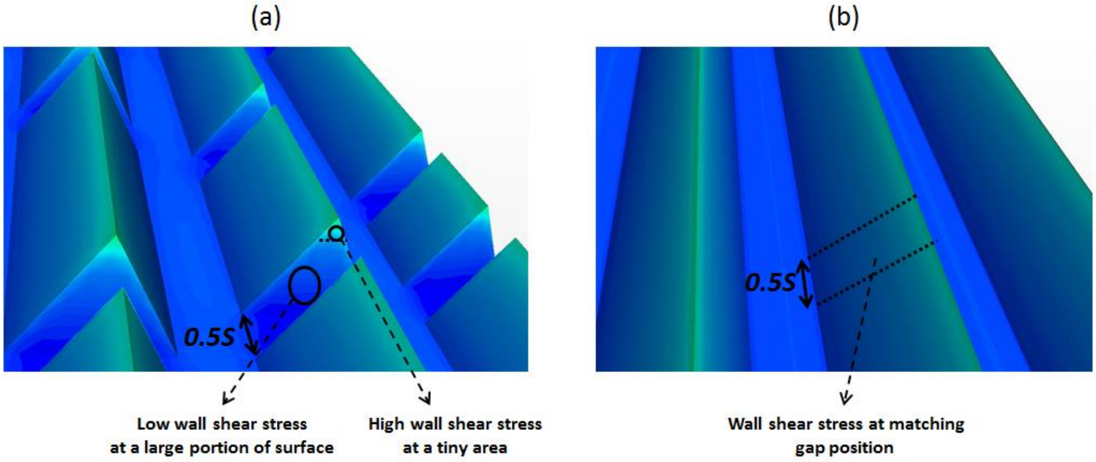

Figure 4.12 (a) Wall shear stress of new design surface (b) Wall shear stress of trapezoidal riblet

In the gap region ($\frac{1}{3}$s long) of the new design surface, a large portion of the cross-section area has a low wall shear stress, and thus lower velocity gradient and skin friction. By contrast, at the matching gap region of a trapezoidal riblet surface, the wall shear stress is consistent in the streamwise direction and a larger area of surface area is exposed to high-speed flow, and thus larger wall shear stress and skin friction.

4.4 Discussion on New Surface's Fouling-Control Performance

Concerning the new design surface proposed in this thesis, its unique fouling-control performance will be discussed here both theoretically and numerically. Some practical suggestions for potential commercial application are also indicated to improve its fouling-control performance.

4.4.1 Unique Fouling-Control Potential

- ***Intense Flow Activities above New Surface***

As discussed earlier in this chapter, the strong momentum exchange discovered near the tip region of new design surface might lead the fouler to perceive the proposed surface as unconductive to settlement in the 'surface-sensing' phase of settlement. For instance, motile spores produced by Ulva and barnacle cyprids are the most commonly occurring micro- and macro-fouler on ship hulls.

For both of them, the choice of settlement location is very important because the settling process is irreversible. By secreting adhesive, Ulva spores and barnacle cyprids are permanently attached to the substratum and their motility is lost (Callow and Callow 2000, Schumacher, Aldred et al. 2007).

- ***Larger Wall Shear Stress at the New Surface's Tip Region***

Although both physical (surface length scale, surface complexity) and chemical (low surface energy) technologies are effective methods to deter initial colonization of micro-fouler from attaching ship hull surface, it is unlikely to draw a conclusion that micro-organisms can be thoroughly prevented from accumulating on the underwater surface concerning the complex variety of molecules and organisms. For micro-organisms that have been attached on the surface, it is important to examine the value of adhesion strength, defined as the force required for removing a marine organism from a given surface and expressed as force per unit area (N/m^2=Pa).

Hereby, the wall shear stress over the smooth surface and new design surface is compared to understand the hydrodynamic impact of the new design surface on its fouling release performance. As shown in Figure 4.13, the ration of new surface wall shear stress and smooth surface wall shear stress along the spanwise direction is well compared for case 1.

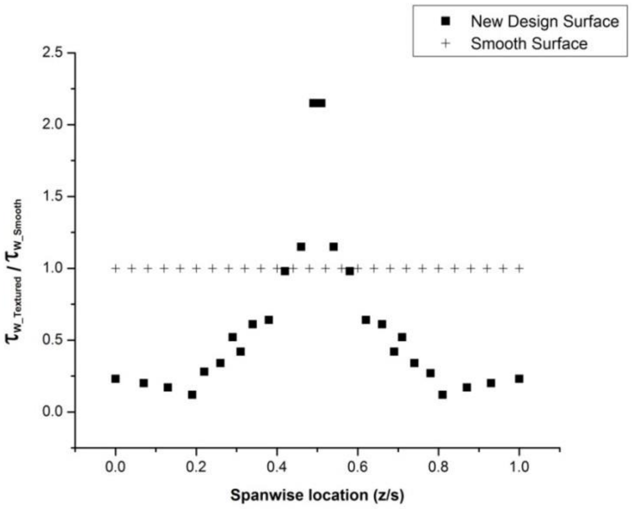

Figure 4.13 Wall shear stress distribution of two representative surfaces along spanwise z direction

Due to more intense turbulent activities near the tip region, the wall shear stress of the new surface is obviously larger than that of smooth surface in the spanwise range of ~0.45s and ~ 0.55s where the peak wall shear stress is achieved and twice as much as that of smooth surface. As the distance from the rib tip increases, the wall shear stress gradually becomes smaller and experiences a slight fluctuation at the rib groove. A very rough estimate of the wall shear stress at the tip region of the new surface is estimated here based on the work of Pablo (2013). As shown below, the hydrodynamic analysis of reference hull, KVLCC2 is depicted, whereas Figure 4.14 plots the distribution of the friction coefficient in full scale, and Figure 4.15 plots the friction coefficient along longitudinal cuts for the reference hull, the KVLCC2.

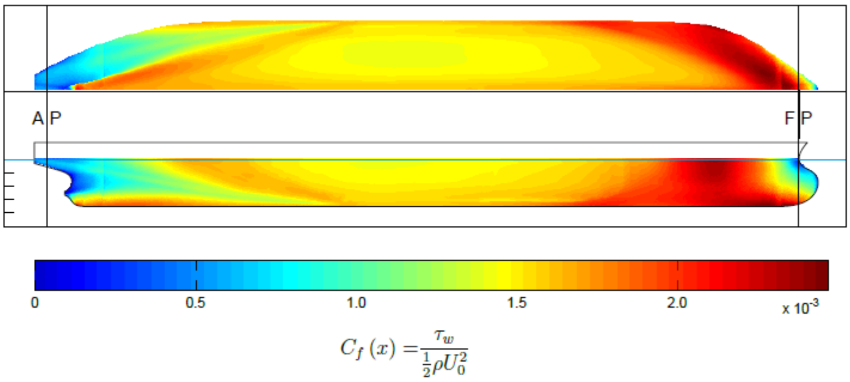

$$C_f(x) = \frac{\tau_w}{\frac{1}{2}\rho U_0^2}$$

Figure 4.14 Friction coefficient distribution on the surface of KVLCC2 in full scale. (Pablo 2013)

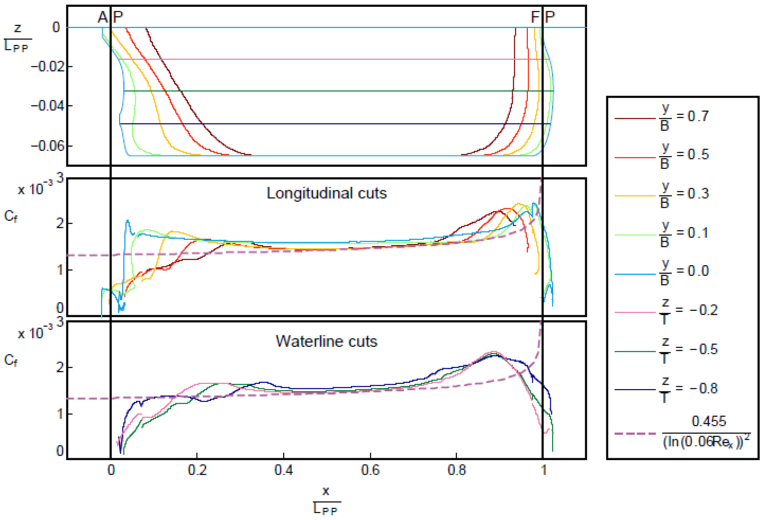

Figure 4.15 Friction coefficient distribution along water lines and longitudinal cuts of the KVLCC2 in full scale. (Pablo 2013)

As shown above, the majority region of the underwater hull surface of KVLCC2 experiences a friction coefficient of ~1.5E-3 or equivalently 47.7 Pa at the given service speed of 7.974 m/s (Pablo 2013). Compared to the given adhesion strength of diatoms and macroalgae which is no bigger than ~100 Pa in the most time (Oliveira and Granhag 2016), the new surface's tip region wall shear stress is much larger than the smooth surface and more efficient to remove the micro-fouler. Concerning the complex marine environment, coating material, sailing speeds, etc., more experimental tests are needed in the future to quantify the impact of new design surface on marine attachments.

- ***Length Scale***

The length scale of the proposed surface is particularly determined to hit the peak drag-reduction performance for applications on ocean-going ships. For example, concerning a 335m Post Panamax Container Vessel operated in 2008 at a service speed of 22 knots (Banks, Turan et al. 2013), the rib width of the proposed surface is estimated to be 36μm which is regarded as an effective length scale to resist relatively larger marine organisms such as tubeworm larva and barnacle cypris larva. Experimental results from Schumacher, Aldred et al. (2007) indicate supportive findings that a 10 times larger Sharklet surface (20μm width) is a superior barnacle-specific anti-fouling solution, which reduces the mean cyprid settlement by 97% compared to a smooth PDMSe surface.

4.5 Summary

A detailed hydrodynamic analysis of the new design surface has been conducted in this section and the questions proposed at the start of this chapter can be answered. Firstly, according to the preliminary study results, the new design surface indicates the potential of drag-reduction property due to the direct monitoring of the surface skin friction decrease and the upward mean velocity shift in the logarithmic layer. Moreover, it is found that the impact of the surface topology is confined to the near wall region approximately two rib heights away from the valley. In the later section, the drag-reduction performance of the new design surface is further confirmed in the parametric study.

Secondly, according to the parametric study of the new design surface, Case 12 (h^+=13.3, s^+=10.8) is the best performing configurations out of those considered in the parametric study. Ultimately, the features of an optimum new surface design are concluded as:

- Minimized wetted surface area
- Capable of preventing vortical structures from falling into grooves
- Capable of imposing lateral inhibition effect on spanwise velocity fluctuations

Thirdly, the existence of streamwise riblet discontinuity is numerically proved to improve the new surface's drag-reduction performance by approximately 0.6% when compared to the trapezoidal riblet. This improvement is attributed to the inactive flow region within the riblet gap which exposes the smaller surface area to high-speed flow and thus smaller velocity gradient and skin friction.

Finally, the fouling-control potential of the new design surface is discussed from three aspects: impact of intense near-wall turbulent activities, wall shear stress, and length scale. New surface is believed to have superior fouling-control performance in the tip region and current length scale is expected to inhibit the settlement of relatively larger marine organisms such as tubeworm larva and barnacle cypris larva. Concerning the practical application of new design surface in ship coating system, it is suggested to assess the feasibility of modifying existing commercialized Foul Release Coating to produce a hierarchical surface structure that may well reinforce the fouling-control performance and increase the breadth of use.

5. Predicting the Performance of Drag-Reduction Coating Surface on Full-Scale Ship

5.1 Introduction

With the growing awareness of the large contribution of greenhouse gas (GHG) emissions from the shipping industry, some regulations such as: EEDI, SEEMP, etc. have been proposed by IMO to urge the ship owner and operator at each stage of the plan to consider new technologies and practices when seeking to optimise the performance of a ship. As a result, research on innovative energy-saving approaches has become a popular topic in the past decade, among which the riblet technique is expected to be a promising solution.

Since the discovery of riblet drag reduction property, some high-fidelity numerical work (Choi, Moin et al. 1993, Goldstein, Handler et al. 1995, Yulia Peet, Pierre Sagaut et al. 2007, Mohsen Jahanmiri and Bahraini 2015) using Direct Numerical Simulation (DNS) and Large Eddy Simulation (LES) were conducted to investigate the effect of riblet structure on the near wall turbulent activities and coherent structure. Similar CFD studies have also been completed in Chapter 4 and Chapter 5 to study the drag-reduction performance of symmetric v-groove riblet surface and the new design surface.

Due to the micro-scale size of the target rib structure, the current CFD studies are generally conducted in a small channel flow, whose physical size is only millimetres long. It is believed that the drag-reduction study for a full-scale ship may serve as a great guideline for naval architects to understand the potential impact of drag-reduction coating surface on ship’s frictional resistance, and ship energy efficiency. However, it is not economical or even possible to resolve the CFD governing equations at a micro-scale riblet height throughout the entire computational domain, size of which is as large as a full-scale ship. Alternatively, the similarity law scaling method proposed by Granville (1958) can serve as a good option to estimate the impact of the drag-reduction coating surface on the frictional resistance of flat plates of ship lengths.

In section 5.2, the background information of Granville's work is depicted in two aspects: derivation of the general mathematical representation of the flat plate resistance, and the similarity law scaling procedure. Based on the information, an in-house code was developed for the automatic calculation of friction coefficient, drag-reduction percentage, and suitable riblet coating size, which helps to satisfy the author's requirement of a large amount of computational efforts.

In section 5.3, a three-step procedure to derive the suitable riblet coating size is suggested. A 100m case ship was used in this section to go through each step of the proposed procedure, and exact values of suitable coating heights are calculated at three sailing modes, hypothetically coated with two representative drag-reduction surfaces. In order to avoid the complex and repetitive work of the three-step procedure, the convenient and useful charts for two representative drag-reduction surfaces are established to help a naval architect to quickly find the rough range of the optimum coating size.

In Section 5.4, the study extends to the field of predicting the drag-reduction impact on the full-scale ship. In the real world, there exists a speed distribution that is determined by many factors such as ship types, ballast/loaded condition, weather, etc. The suitable riblet coating sizes of some case ship types, hypothetically coated with two representative coating surfaces, are calculated, and their drag-reduction performance is subsequently predicted along the speed distribution range by using the similarity law scaling method.

The summary of this chapter is given in Section 5.5.

5.2 Methodology

The core sector of this model is based on the work of Granville (1958), who derived a general, complex mathematical representation of the flat plate resistance, and proposed the similarity law scaling process to predict the frictional drag of full-scale ships based on experimental flat plate towing test results. In this section, the derivation of the general logarithmic resistance formula and the process of similarity law scaling are presented accordingly.

5.2.1 Derivation of General Logarithmic Resistance Formula

The complete derivation process of general logarithmic resistance formula is a pretty complex analytical process, but the details can be found in the work of Granville (1958). Thus, it will be condensed and summarized here to clarify the important procedures only. During this derivation process, it is found that the final resistance formula is derived in a general way and thus could be used universally. In other words, this method is not restricted to drag increasing problems. It is also applicable to drag-reduction problems. The general process has been subdivided into three parts which are discussed next:

- Boundary-Layer characteristics from similarity laws
- Boundary-layer parameters – Momentum thickness
- The frictional resistance of flat plates

Boundary-Layer characteristics from similarity laws

For turbulent shear flows, such as the fully-developed channel flow mentioned in Chapter 5, there are two laws: inner law and outer law. The overlapping region of inner law and outer law gives rise to velocity logarithmic relationships and important local skin friction as shown in Eq.32 – Eq.35

$$\frac{u}{u_\tau} = Aln(y^+) + B_1\left(k^+, \frac{k}{k_1}, \frac{k}{k_2}, \dots\right) \; or = Aln\left(\frac{y}{k}\right) + \; B_2\left(k^+, \frac{k}{k_1}, \frac{k}{k_2}, \dots\right) \tag{32}$$

$$\frac{U-u}{u_\tau} = -Aln\left(\frac{y}{\delta}\right) + B_3 \tag{33}$$

$$\sigma \equiv \frac{U}{u_\tau} = Aln\left(\frac{u_\tau \delta}{\nu}\right) + B_3 + B_2 \ or = Aln\left(\frac{\delta}{k}\right) + B_3 + B_2 \tag{34}$$

$$\frac{\sqrt{2}}{\sqrt{C_\tau}} = Aln\left[\sqrt{C_T}\left(\frac{U\delta}{\nu}\right)\right] + B_3 + B_2 \ or \ Aln\left(\frac{\delta}{k}\right) + B_3 + B_2 \tag{35}$$

Boundary-layer parameters – Momentum thickness

The boundary-layer parameters of momentum thickness (θ) is obtained by the integrations of the appropriate velocity laws for each sublayer shown in Table 5.1, Table 5.2 and Table 5.3.

Table 5.1 Information of limits of y and velocity law at each sublayer (Granville 1958)

Sublayer	Limits of y	Velocity Law
Laminar sublayer	$0 \le \frac{y}{k} \le (\frac{y}{k})_L$	$\frac{u}{u_\tau} = k^+(\frac{y}{k})$
Transitional sublayer	$(\frac{y}{k})_L \le \frac{y}{k} \le (\frac{y}{k})_T$	$\frac{u}{u_\tau} = Aln(y^+ - J_2) + B_2$
Inner turbulent boundary layer	$(\frac{y}{k})_T \le \frac{y}{k} \le (\frac{y}{k})_G$ $(\frac{y}{k})_G = \left(\frac{y}{\delta}\right)_G (\frac{\delta}{k})$	$\frac{u}{u_\tau} = Aln\frac{y}{k} + B_2$
Outer turbulent boundary layer	$(\frac{y}{\delta})_G \le \frac{y}{\delta} \le 1$	$\frac{u}{u_\tau} = \sigma - F$

Table 5.2 Integral of velocity law at different sublayers (Granville 1958)

Sublayer	$\int \frac{u}{u_\tau} d(\frac{y}{k})$
Laminar sublayer	$\frac{k^+}{2}(\frac{y}{k})_L^{\ 2}$
Transitional sublayer	$\left[\left(\frac{y}{k}\right)_T - J_2\right]\left(\frac{u}{u_\tau}\right)_T - A\left(\frac{y}{k}\right)_T$
Inner turbulent boundary layer	$(\frac{y}{k})_G\left[\left(\frac{u}{u_\tau}\right)_G - A\right] - \left(\frac{y}{k}\right)_T\left[\left(\frac{u}{u_\tau}\right)_T - A\right]$
Outer turbulent boundary layer	$\frac{\delta}{k}\left\{\left[1 - \left(\frac{y}{\delta}\right)_G\right]\sigma - I_1\right\}$

Table 5.3 Integral of velocity law square at different sublayers (Granville 1958)

Sublayer	$\int (\frac{u}{u_\tau})^2 \, d(\frac{y}{k})$
Laminar sublayer	$\frac{{k^{+}}^{2}}{3}(\frac{y}{k})_l^{\ 3}$
Transitional sublayer	$\left[\left(\frac{y}{k}\right)_T - J_2\right]\left[\left(\frac{u}{u_\tau}\right)_T - A\right]^2 - \left[\left(\frac{y}{k}\right)_L - J_2\right]\left[\left(\frac{u}{u_\tau}\right)_L - A\right]^2 + l^2$
Inner turbulent boundary layer	$(\frac{y}{k})_G \left[\left(\frac{u}{u_\tau}\right)_G - A\right]^2 - \left(\frac{y}{k}\right)_T \left[\left(\frac{u}{u_\tau}\right)_T - A\right]^2 + A^2\left[\left(\frac{y}{k}\right)_G - \left(\frac{y}{k}\right)_T\right]$
Outer turbulent boundary layer	$\frac{\delta}{k}\left\{\left[1 - \left(\frac{y}{\delta}\right)_G\right]\sigma^2 - 2\sigma I_1 + I_2\right\}$

Where

- $I_1 = \int_{(\frac{y}{\delta})_G}^{1} F d(\frac{y}{\delta}), I_2 = \int_{(\frac{y}{\delta})_G}^{1} F^2 d(\frac{y}{\delta})$
- $\alpha_1 = \frac{{y_{L^+}}^2}{2} - J_1(\frac{u}{u_\tau})_T, \alpha_2 = \frac{\alpha_1}{k^+}$
- $D_1 = \left(\frac{y}{\delta}\right)_G (F_G + A) + I_1, D_2 = \left(\frac{y}{\delta}\right)_G [(F_G + A)^2 + A^2] + I_2$
- $\beta_1 = \frac{{y_{L^+}}^3}{3} - J_1\left[\left(\frac{u}{u_\tau}\right)_T - A\right]^2 - A({y_{L^+}}^2 - Ay_{L^+} + A^2), \beta_2 = \frac{\beta_1}{k^+}$

The momentum thickness is defined as:

$$\theta = \int_0^\delta \frac{u}{U}\left(1 - \frac{u}{U}\right) dy \tag{36}$$

By taking all relevant equations shown in Table 5.1, Table 5.2, and Table 5.3 to Eq.36, the following formula that depicts momentum thickness θ is shown below.

$$\frac{\theta}{k} = \frac{\delta}{k}\left(\frac{D_1}{\sigma} - \frac{D_2}{\sigma}\right) + \frac{\alpha_2}{\sigma} - \frac{\beta_2}{\sigma^2} \tag{37}$$

The frictional resistance of flat plates

Since the frictional resistance of a flat plate without considering pressure gradients can be calculated by the momentum thickness of the boundary layer flow, the derivation thus starts from Von Karman momentum equation (Von Karman 1930), which neglects the small effect of normal Reynolds stress term, as shown in Eq.38.

$$\frac{d\theta}{dx}=\frac{\tau_w}{\rho U^2} \tag{38}$$

Where

- θ: momentum thickness
- x: distance from the trailing edge
- τ_w: wall shear stress
- ρ: fluid density
- U: speed of flat plate

Since the resistance coefficient can be represented as $C_f=\frac{R_f}{\frac{1}{2}\rho U^2 xb}$, where R_f is the total frictional resistance on one side and b is the width of the plate, and Eq.39 represents an alternative description of C_f as a summation of local resistance,

$$\frac{C_f}{2}=\frac{1}{x}\int_0^X \frac{\tau_w}{\rho U^2}dx \tag{39}$$

then a new relation is created as shown in Eq.40

$$\frac{C_f}{2}=\frac{\theta}{x}=\frac{R_\theta}{R_x}=\frac{\frac{\theta}{k}}{\frac{x}{k}} \tag{40}$$

Where

- $R_\theta=\frac{U\theta}{\nu}$ and $R_x=\frac{Ux}{\nu}$

By definition,

$$\sigma^2=\frac{1}{\frac{\tau_w}{\rho U^2}} \tag{41}$$

Therefore, the Eq.38 becomes:

$$d\left(\frac{x}{k}\right) = \sigma^2 d\left(\frac{\theta}{k}\right) \quad or\ dR_x = \sigma^2 dR_\theta \tag{42}$$

For a uniform roughness where k is constant with respect to x, there exists

$$\frac{x}{k} = \int \sigma^2\, d\left(\frac{\theta}{k}\right) = \sigma^2 \frac{\theta}{k} - 2\int \frac{\theta}{k}\sigma d\sigma + const \tag{43}$$

The relation of $\frac{\theta}{k}$ and $\frac{\delta}{k}$ are separately indicated in Eq.37 and Eq.34. Then we insert relation of $\frac{\delta}{k}$ into Eq.37, and integrate by parts repeatedly to get the result:

$$\int \frac{\theta}{k}\sigma d\sigma = \frac{\delta}{k}\left\{AD_1\left[1 - \frac{B_2'}{\sigma} - \frac{A}{\sigma^2}\left(B_2' + B_2'' - \frac{{B_2'}^2}{A}\right) + \cdots\right] - \frac{AD_2}{\sigma}\left[1 + \frac{(A-B_2')}{\sigma} + \cdots\right]\right\} + \int \alpha_2 d\sigma - \int \frac{\beta_2}{\sigma} d\sigma + const \tag{44}$$

Where

- $B_2' = \frac{dB_2}{d(lnk^+)}$ and $B_2'' = \frac{d^2B_2}{d(lnk^+)^2}$

Substituting Eq.44 into Eq.42 results in:

$$R_x = \frac{u_\tau \delta}{\nu}\left\{D_1\sigma^2 - D_2\sigma - 2AD_1\sigma\left[1 - \frac{B_2'}{\sigma} - \frac{A}{\sigma^2}\left(B_2' + B_2'' - \frac{{B_2'}^2}{A}\right) + \cdots\right] + 2AD_2\left[1 + \frac{(A-B_2')}{\sigma} + \cdots\right]\right\} + \alpha_1\sigma^2 - \beta_1\sigma - 2\int \alpha_1 d\sigma + 2\int \beta_1 d\sigma + const \tag{45}$$

The next step is to derive the direct logarithmic resistance formula of C_f. Firstly, initial relationships of $C_f\ vs\ \frac{x}{k}$, $\frac{x}{k}\ vs\ \sigma$ are established as shown in Eq.40 and Eq.43. Combination of the two equations gives:

$$\frac{1}{\sigma^2} = \frac{C_f}{2}\left(1 - \frac{2\int \frac{\theta}{k}\sigma d\sigma}{\sigma^2 \frac{\theta}{k}}\right) \tag{46}$$

With the help of Eq.37 and Eq.44, the parameters of $\int \frac{\theta}{k}$ and $\frac{\theta}{k}$ are eliminated. Finally the relation between C_f and σ is obtained:

$$\sigma = \sqrt{\frac{2}{C_f}}\left[1 + A\left(\frac{C_f}{2}\right)^{1/2} + A\left(\frac{A}{2} - B_2'\right)\left(\frac{C_f}{2}\right) + \cdots\right] \tag{47}$$

Now, after substituting σ from Eq.47 and rewriting Eq.45 in logarithmic form, the general logarithmic resistance formula is finally obtained as:

$$ln\, R_x C_f = \frac{\sqrt{2}}{A}\frac{1}{C_f} - \frac{1}{\sqrt{2}}\left(\frac{D_2}{D_1}\right) - \frac{A}{2} + B_2')\sqrt{C_f} + 1 - \frac{B_3}{A} - \frac{B_1}{A} + ln\sqrt{2}D_1 \tag{48}$$

It is essential to point out that the expression could be applied universally. For a smooth flat plate, the value of B_2 equals to 5.5, suggested by Nikuradse (1950). The effect of surface roughness would actually causes an upward (drag-reduction) or downward (drag-increase) shift in the near wall mean velocity profile. In the derivation process of the general logarithmic resistance formula, the effect of surface roughness is represented by all k^+ relevant parameters like B_1, B_2, α_1, α_2, β_1, β_2. Either drag-reduction effects or drag-increase effects could be well depicted, and thus the general logarithmic resistance formula could be used universally.

5.2.2 The Procedure of Similarity Law Scaling Method

After deriving the mathematical expression of flat plate frictional resistance with respect to surface roughness k^+, it is appropriate to talk about the similarity law scaling method that is used here to predict the frictional drag of the full-scale ship. In the work of Granville (1958), the similarity law scaling is employed to simplify the calculation of frictional drag of full-scale ship. The process is split into four steps:

1. Plot of general smooth plate friction coefficient, $C_{f_{smooth}}$
2. Plot of target plate friction coefficient line (a certain type of coating)
3. Plot of constant ${L_{plate}}^+$ (from the experimental towing test)
4. Plot of constant ${L_{ship}}^+$

Finally, the intersection of constant $\mathrm{L_{ship}}^{+}$ and target plate friction coefficient line is the frictional coefficient of the full-scale ship covered with a target type of coating. The detailed description of similarity law scaling is shown as follows:

Step 1: Plot of general smooth plate frictional coefficient, $\mathrm{C_{f_{smooth}}}$

The investigation of frictional resistance of full-scale ship is firstly proposed by Froude (1872). Froude (1874) carried out the pioneering study on the frictional drag of flat plate, and also a wooden full-scale ship of 52.28 m. Froude (1874) proposed an important assumption that the skin friction of a hull is equal to that of a flat plate of the same length and area as the wetted surface of the ship. Following his work, Prandtl (1921) proposed Eq.49 for the skin friction of a flat plate in turbulent flows based on the experimental data of Froude (1872), Froude (1874), and Gebers (1919).

$$C_F = \frac{R_F}{\frac{1}{2}\rho S_w V^2} = 0.072\left(\frac{VL}{\nu}\right)^{-\frac{1}{2}} \tag{49}$$

Later, Prandtl (1927), Prandtl (1932) derived a theoretical skin friction formulation based on the universal logarithmic boundary layer velocity profile – Eq.50, which could be regarded as a reference line compared to the aforementioned general logarithmic resistance line.

$$\frac{A}{\sqrt{C_F}} = \log(Re \times C_F) + M \tag{50}$$

Following this, Schoenherr (1932) proposed the Schoenherr friction line formula – Eq.51 by incorporating almost all experimental data, high Reynolds number results from Kempf (1929), low Reynolds number of his own measurements.

$$\frac{0.242}{\sqrt{C_F}} = \log(Re \times C_F) \tag{51}$$

In the similarity law scaling process, Schoenherr friction line is used to represent the frictional coefficient line of a smooth surface. Schoenherr friction line was mentioned as the 1947 ATTC line. The American Towing Tank Conference (ATTC) proposed the use of Schoenherr friction line with a constant roughness allowance of 0.0004 for the prediction of the skin friction coefficients of clean new vessels. (Demirel 2015)

Step 2: Plot of the target plate friction coefficient line

As suggested by Granville (1958), the resistance line of constant k^+ for the rough case is offset from the smooth line by a constant amount in the direction of $\log_{10}R_x$, which is given by:

$$log_{10}R_x - log_{10}R_{x,s} = \frac{B_{1,s} - B_1}{2.3026A} \tag{52}$$

Actually, the value of $(B_{1,s} - B_1)$ represents the mean velocity difference of smooth and rough plate, and is renamed ΔU^+ in the paper of Demirel, Khorasanchi et al. (2014).

The value of ΔU^+ varies with h^+ based on types of surface coatings from small to large. Unfortunately, limited by the small size (micron level) of the drag reduction surface pattern, current available computer resources could only solve turbulent channel flow with periodic boundary conditions implemented. Simulation of flat plate towing test in commercial CFD software becomes impossible because of the extremely large ratio of plate length (L_{plate}) to surface pattern height (h), up to five orders of magnitude. The large value of ${}^{L_{plate}}/_{h}$ requires a great number of mesh to calculate the physical properties which exceeds the capability of current available computational resources. Simulation of turbulent flow over the drag-reduction surface in the channel also poses a problem that the centreline velocity is the same for either smooth or drag-reduction surface as a result of the finite height of the channel. Thus it is impossible to directly obtain the difference of mean velocity profile, ΔU^+.

Instead, an alternative method is to employ a formula suggested by Aupoix, Pailhas et al. (2012) which calculates ΔU^+ in terms of frictional coefficient as shown below:

$$\Delta U^+ = \sqrt{\frac{2}{C_{fR}}} - \sqrt{\frac{2}{C_{fS}}} \tag{53}$$

It needs to be pointed out that this formula is not a good formula for the calculation of ΔU^+ because it has been developed for external turbulent flow over plates. Surprisingly, the results calculated with this formula show relatively good fit with experimental results of external flow over the drag-reduction surface and will be discussed quantitatively later. As a result, the formula will be used here, but a general approach to calculate ΔU^+ in channel flow is surely needed for a more accurate result in the future.

Step 3: Plot of constant ${L_{plate}}^+$ value

Normally, the plot of ${L_{plate}}^+$ is obtained by fitting the experimental data of model-scale towing tests. In this study, no experiments are carried out and only CFD results are used to predict the full-scale ship and thus this step is not really implemented in the in-house code for full-scale ship prediction. To make the process complete, the mathematical representation of the constant ${L_{plate}}^+$ suggested by Granville (1958) is shown below:

$$log{L_{plate}}^+ = logR_{L_{plate}} + log\sqrt{\frac{C_f}{2}} - \frac{A}{2.3026}\sqrt{\frac{C_f}{2}} \tag{54}$$

${L_{plate}}^+$ is defined by:

$${L_{plate}}^+ = \frac{L_{plate}u_\tau}{\nu} \tag{55}$$

The friction velocity u_τ could be obtained by

$$u_\tau = \frac{h^+}{h} \tag{56}$$

Step 4: Plot of constant ${L_{ship}}^+$ value

The plot of the constant $\mathrm{L_{ship}}^+$ line is to transform $\mathrm{L_{plate}}^+$ by a constant distance of $\log(\frac{\mathrm{L_{ship}}}{\mathrm{L_{plate}}})$ in the direction of $\log(\mathrm{Re})$. A similar formula as Eq.57 is employed to represent the line of constant $\mathrm{L_{ship}}^+$.

$$logL_{ship}{}^{+} = logR_{L_{ship}} + log\sqrt{\frac{C_f}{2}} - \frac{A}{2.3026}\sqrt{\frac{C_f}{2}} \tag{57}$$

The similarity law scaling is depicted in Figure 5.1.

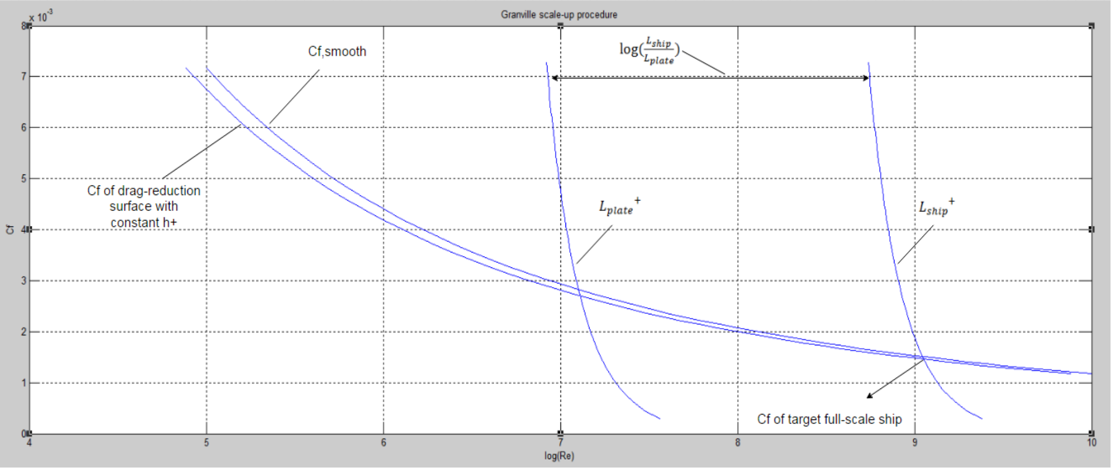

Figure 5.1 An example of Granville scale-up procedure result

It is shown that the intersection point of the target plate friction coefficient line and constant $\mathrm{L_{ship}}^+$ is the target value of the full-scale ship that is expected to be estimated. The whole similarity law scaling process is written as an in-house code so that a series of results will be generated automatically and compared with various input of ship and coating specification.

5.3 Suitable Riblet Coating Size

Past research indicates that riblet drag reduction performance is severely affected by the flow velocity if the riblet size is kept the same. The ideal riblet coating size for the bulk carrier cannot be the same as that of container ship concerning the difference in the ship length and service speed. Any inappropriate decision on riblet coating size would cause unnecessary waste of fuel consumption and extra exhaust emissions. Considering green shipping, riblet coating size should be determined according to target ship information. In this section, the 100m cargo vessel will be taken as an example, and two types of surface coatings (symmetric v-groove riblet, new design surface) that are numerically modelled in Chapter 4 and Chapter 5 will be analysed. Following the 100m cargo vessel example, a broad range of ship lengths from 10m to 400m will be calculated to establish a complete and practical chart that makes it easier and more convenient for naval architects to confirm the rough suitable riblet coating size range.

5.3.1 Three-Step Procedure – Case Study of a 100 Meter Cargo Vessel

Each company in the shipping trade has its own objectives for the ships to operate at an optimal speed in order to gain the highest gross profit per day per vessel. Soren Retz Johansson, a port captain at Denmark's Norden Shipping highlighted that the latest mega-sized 18,000 TEU containerships are designed for slow steaming (Liang 2014). The aim of slow steaming is to cut down cargo ship's fuel consumption and carbon emissions by sailing at a reduced speed. Since 2007, the idea of slow steaming has gradually become a common operating feature of today's shipping market, particularly due to the economic crisis and weak freight market.

The following case study of the 100m cargo vessel focuses on the topic of slow steaming and aims to propose a practical workflow to derive the suitable coating size that fits with the target ship. Three hypothetical 100m cargo vessels are considered, which are designed to operate at super slow steaming mode, slow steaming mode, and normal mode with an average speed of 12 knots, 20 knots, and 25 knots respectively. As shown next, a three-step procedure is proposed to practically choose the suitable coating size.

Step 1: Confirm basic ship information such as the service speed, ship length, and the specific type of riblet coating; Conduct CFD simulations to examine the particular drag-reduction performance, and calculate the unique value of riblet coating's roughness function and ΔU^+ based on relevant precursor CFD simulations.

Step 2: Utilize the existing input information and the developed in-house MATLAB code to narrow the suitable riblet coating size to a rough range.

Step 3: Split the rough coating size range into acceptable small intervals, and run the in-house MATLAB code again to find out the optimum riblet coating size.

Each of the three steps is respectively described in Section 5.3.1.1, Section 5.3.1.2, and Section 5.3.1.3.

5.3.1.1 Step 1: Derivation of Particular Roughness Function

Roughness is a general definition of the deviation in the direction of the normal vector of a real surface from its ideal form. In the context of drag reduction coating such as riblet structure, roughness is usually regarded as the height of every single patterned unit, indicated by the symbol, h. Surface roughness always induces a vertical shift of the mean velocity profile in the log layer, and the shift of mean velocity profile in the logarithmic region is represented by the roughness function, ΔU^+. A positive ΔU^+ indicates a drag decreasing surface (riblet structure), and a negative ΔU^+ indicates a drag increasing surface (sand grain roughness, etc.) as shown in Figure 5.2.

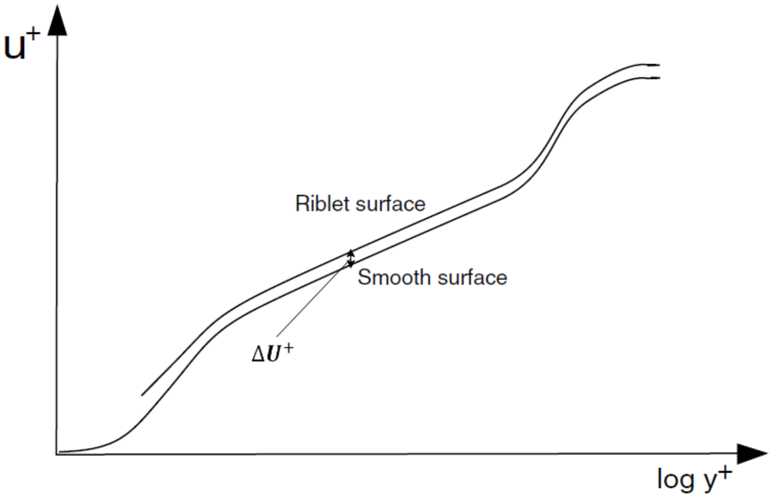

Figure 5.2 Upward shift of logarithmic law due to riblet surface roughness (Aupoix, Pailhas et al. 2012)

The roughness function does not have a universal value and differs by surface patterns and dimensions. In the present mathematical model, the roughness functions of various surfaces are derived by the commercial CFD code validated above rather than the experimental towing test of flat plates. Numerical modelling of turbulent flow over certain riblet surface in the channel does offer an accurate estimate of its drag reduction performance at a certain range of h^+. However, the value of roughness function cannot be directly obtained from the vertical gap of mean velocity profiles of smooth and drag reduction surfaces due to the restriction of the channel as mentioned in Section 5.2. As a result, a simple formula, Eq.58, will be alternatively used to calculate roughness function as employed in the work of Aupoix, Pailhas et al. (2012):

$$\Delta U^+ = \sqrt{\frac{2}{C_{fR}}} - \sqrt{\frac{2}{C_{fS}}} \tag{58}$$

Where

- C_{fR}: friction coefficient of bottom riblet surface of channel flow
- C_{fS}: friction coefficient of top smooth surface of channel flow

With the statistical support from CFD investigations of two representative coating surfaces (symmetric v-groove riblet surface, new design surface) conducted in Chapter 3 and Chapter 4, it is now possible to calculate ΔU^+ at every single value of h^+ by employing Eq.58. As shown in Figure 5.3, the polynomial regression method is used to determine the trending line with the input of all numerically calculated C_{fR} and C_{fS} from CFD results.

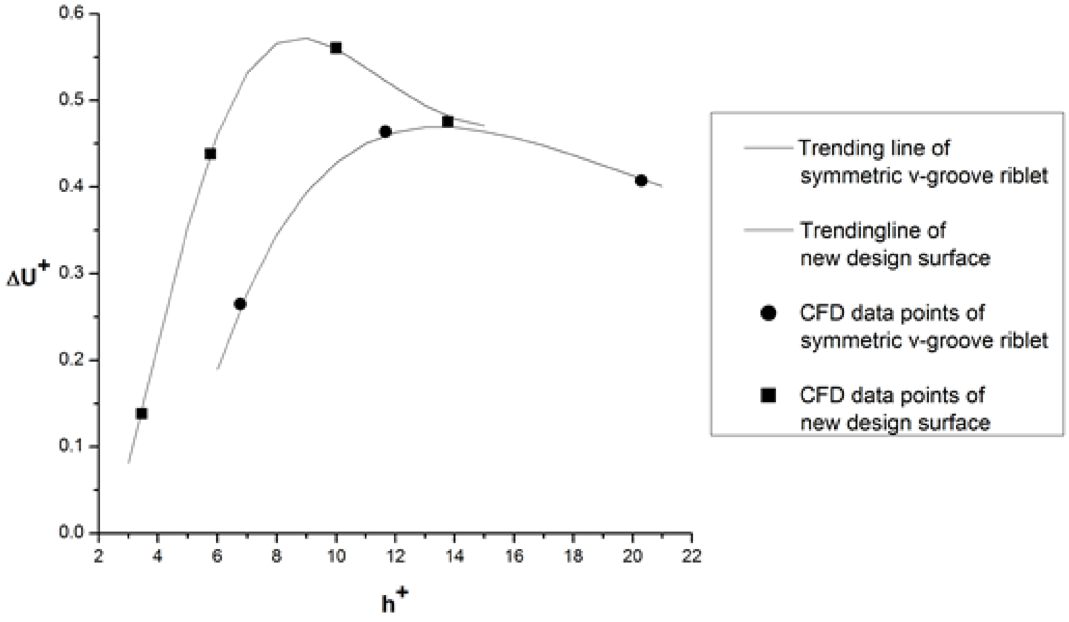

Figure 5.3 Trending lines for two representative surfaces based on CFD results

Two equations, Eq.59 and Eq.60, are respectively determined to associate ΔU^{+} and h^{+} for symmetric v-groove riblet surface and new design surface respectively.

$$\Delta U^{+} = -2.6576 * 10^{-9}(h^{+})^{6} + 5.0898 * 10^{-7}(h^{+})^{5} - 3.9204 * 10^{-5}(h^{+})^{4} + 1.5581 * 10^{-3}(h^{+})^{3} - 3.3836 * 10^{-2}(h^{+})^{2} + 3.6994 * 10^{-1}h^{+} - 1.1018 \tag{59}$$

$$\Delta U^{+} = 5.9326 * 10^{-10}(h^{+})^{8} - 9.0145 * 10^{-8}(h^{+})^{7} + 5.7092 * 10^{-6}(h^{+})^{6} - 1.9437 * 10^{-4}(h^{+})^{5} + 3.8168 * 10^{-3}(h^{+})^{4} - 4.2827 * 10^{-2}(h^{+})^{3} + 2.5010 * 10^{-1}(h^{+})^{2} - 5.6305 * 10^{-1}h^{+} + 0.4095 \tag{60}$$

Since the coating size is designed to hit the peak drag-reduction performance, the maximum values of ΔU^{+} for two representative surfaces need to be calculated. The relevant values of ΔU^{+} and h^{+} derived from Eq.59 and Eq.60, and all basic information of the target ship are shown in Table 5.4.

Table 5.4 Summary of target ship information and maximum roughness function of two representative surfaces

	Ship length (m)	Service speed (knots)	Symmetric v-groove riblet surface	New design surface
Cargo ship I	100	12	$h^{+} = 13.46$ $\Delta U^{+}_{max} = 0.469$	$h^{+} = 8.76$ $\Delta U^{+}_{max} = 0.573$
Cargo ship II	100	20		
Cargo ship III	100	25		

Notes: Cargo ship I, II, III represents three hypothetical ships designed for super slow steaming mode, slow steaming mode, and normal mode respectively.

5.3.1.2 Step 2: Narrow the Range of the Suitable Riblet Coating Size Down

Based on the results of Step 1, the specific value of h^{+} is identified for two representative coating surfaces, at which the maximum drag-reduction performance can be achieved. For the case study of 100m cargo vessel, the next question is how to confirm the rough region that the hypothetical riblet coating size should be located at.

To solve this problem, a broad range of rib height (20μm to 200μm) is considered and taken into the in-house MATLAB code based on the similarity law scaling method to calculate the matching ship service speed for each rib height input. By this way, it is possible to determine the respective rib height interval for cargo vessel I, cargo vessel II, and cargo III designed at three service speeds.

The MATLAB output of 100m cargo vessel, hypothetically covered with 60-degree symmetric v-groove riblet surface is shown in Table 5.5.

Table 5.5 Output of 100m cargo vessel covered with 60-degree symmetric v-groove riblet

ΔU^+	h (μm)	$C_{f,Smooth}$	$C_{f,Riblet}$	DR%	U_{ship} (knots)
0.4693	20	0.001364	0.001324	2.99%	50.85
0.4693	30	0.001435	0.001392	3.07%	33.06
0.4693	40	0.001489	0.001444	3.13%	24.35
0.4693	50	0.001533	0.001486	3.18%	19.20
0.4693	60	0.001571	0.001521	3.22%	15.82
0.4693	70	0.001603	0.001552	3.31%	13.42
0.4693	80	0.001632	0.00158	3.34%	11.64
0.4693	90	0.001658	0.001605	3.37%	10.27
0.4693	100	0.001682	0.001627	3.40%	9.18
0.4693	125	0.001735	0.001677	3.45%	7.23
0.4693	150	0.00178	0.001719	3.50%	5.95
0.4693	175	0.001819	0.001756	3.54%	5.05
0.4693	200	0.001854	0.001789	3.58%	4.37

As shown in Table 5.5, ΔU^+=0.4693 is used here to represent the drag-reduction performance of the specific 60-degree symmetric v-groove riblet. The range of rib height is respectively split by a gap of 10μm and 25μm at 20μm-100μm, and 100μm-200μm. The gap is much finer at 20μm-100μm rib height because the relevant service speed range 9.18knots - 50.85knots includes the most frequently operated ship speed in the nowadays shipping industry. For each single rib height, there exists a numerically calculated matching ship service speed at which maximum drag-reduction performance of symmetric v-groove riblet surface can be achieved. Based on the service speeds designed for three hypothetical 100m cargo vessels, it is possible to narrow down the suitable rib height range and the findings are shown below in Table 5.6.

Table 5.6 Narrowed rib height range

	Service speed (knots)	Narrowed rib height range (μm)
Cargo vessel I	12	70 - 80
Cargo vessel II	20	40 - 50
Cargo vessel III	25	30 - 40

Following the same procedure, the MATLAB output of 100m cargo vessel, hypothetically covered with new design surface and the relevant narrowed rib height range are respectively shown in Table 5.7 and Table 5.8.

Table 5.7 Output of 100m cargo vessel covered with new design surface coating

ΔU^+	h *(μm)*	$C_{f,Smooth}$	$C_{f,Riblet}$	*DR%*	U_{ship} *(knots)*
0.5731	20	0.00132	0.001276	3.36%	32.32
0.5731	30	0.001439	0.001389	3.51%	21.00
0.5731	40	0.001516	0.001462	3.60%	15.46
0.5731	50	0.001575	0.001517	3.67%	12.19
0.5731	60	0.001623	0.001562	3.73%	10.04
0.5731	70	0.001663	0.001601	3.77%	8.51
0.5731	80	0.001699	0.001634	3.81%	7.38
0.5731	90	0.00173	0.001664	3.85%	6.51
0.5731	100	0.001759	0.001691	3.88%	5.82
0.5731	125	0.001785	0.001715	3.91%	4.58
0.5731	150	0.001843	0.001769	3.97%	3.77
0.5731	175	0.001891	0.001815	4.03%	3.20
0.5731	200	0.001934	0.001856	4.07%	2.77

Table 5.8 Narrowed rib height range

	Service speed (knots)	Narrowed rib height range (µm)
Cargo vessel I	12	50 - 60
Cargo vessel II	20	30 - 40
Cargo vessel III	25	20 - 30

5.3.1.3 Step 3: Derivation of Exact Riblet Coating Size

After completing the preliminary refining work at step 2, the suitable riblet coating size has been narrowed down to a small range. At step 3, the narrow region of riblet coating size will be further refined to derive the exact riblet coating size, which is realized by running the in-house MATLAB code with a much smaller rib height gap, 0.5µm rather than 10µm or 25µm.

For cargo vessel I designed for super flow steaming mode, the suitable coating sizes of symmetric v-groove riblet surface and new design surface are respectively 70µm-80µm and 50µm-60µm as shown in Table 5.6 and Table 5.8. Based an initial observation of the distribution relationship between h and Uship, a simple prediction can be made to help reduce computational time. For example, in Table 6.7, the service speed of 12 knots is very near to Uship=12.19 knots at h=50 µm, it is thus more economical to have a refined rib height region like 50µm-55µm instead of 50µm-60µm.

The output of suitable rib heights in the refined region for symmetric v-groove riblet surface and new design surface are respectively shown in Table 5.9 and Table 5.10.

Table 5.9 Suitable riblet coating size at a narrow range for symmetric v-groove riblet

ΔU^{+}	h *(µm)*	$C_{f,Smooth}$	$C_{f,Riblet}$	*DR%*	U_{ship} *(knots)*
0.4693	73.5	0.001614	0.001562	3.18%	12.74
0.4693	74	0.001615	0.001564	3.19%	12.65
0.4693	74.5	0.001617	0.001565	3.19%	12.56
0.4693	75	0.001618	0.001567	3.19%	12.47
0.4693	75.5	0.00162	0.001568	3.19%	12.38

0.4693	76	0.001621	0.001569	3.19%	12.29
0.4693	76.5	0.001622	0.001571	3.19%	12.21
0.4693	77	0.001624	0.001572	3.19%	12.12
0.4693	77.5	0.001625	0.001573	3.20%	12.04
0.4693	78	0.001627	0.001575	3.20%	11.96
0.4693	78.5	0.001628	0.001576	3.20%	11.87

Table 5.10 Suitable riblet coating size at a narrow range for new design surface

ΔU^+	h (μm)	$C_{f,Smooth}$	$C_{f,Riblet}$	DR%	U_{ship} (knots)
0.5731	50	0.001623	0.001562	3.73%	12.06
0.5731	50.5	0.001625	0.001564	3.73%	11.93
0.5731	51	0.001627	0.001566	3.73%	11.81
0.5731	51.5	0.001629	0.001568	3.74%	11.69
0.5731	52	0.001631	0.00157	3.74%	11.57
0.5731	52.5	0.001633	0.001572	3.74%	11.45
0.5731	53	0.001636	0.001574	3.74%	11.34
0.5731	53.5	0.001638	0.001576	3.75%	11.23
0.5731	54	0.00164	0.001578	3.75%	11.12
0.5731	54.5	0.001642	0.00158	3.75%	11.01
0.5731	55	0.001644	0.001582	3.75%	10.91

As shown above, the suitable rib height is around 77.5μm-78μm and 50μm-50.5μm for symmetric v-groove riblet surface and new design surface respectively. 77.8μm and 50.3μm are respectively taken as the exact value of suitable rib height if a linear relationship between h and U_{ship} is used. The effect of employing the linear relationship is negligibly small and can be omitted here. Similarly, the work of step 3 is repeated for cargo vessel II and cargo vessel III and the exact suitable riblet coating sizes for two representative coating surfaces and three 100m cargo vessels are summarized in Table 5.11 and Table 5.12.

Table 5.11 Suitable riblet heights for symmetric v-groove riblet at three different modes

Mode	Average ship speed (knots)	Suitable rib height (μm)	ΔU^{+}	$DR\%$
Cargo Vessel I	12 knots	77.8	0.4693	3.20%
Cargo vessel II	20 knots	48.0	0.4693	2.99 %
Cargo vessel III	25 knots	38.9	0.4693	2.95%

Table 5.12 Suitable riblet heights for new design surface at three different modes

Mode	Average ship speed (knots)	Suitable rib height (μm)	ΔU^{+}	$DR\%$
Cargo vessel I	12 knots	50.3	0.5731	3.73%
Cargo vessel II	20 knots	31.4	0.5731	3.57 %
Cargo vessel III	25 knots	25.5	0.5731	3.52%

Following the procedure of three-step approach, the suitable rib heights for three 100m cargo vessels, hypothetically covered with two representative coating surfaces are ultimately derived. It is obvious to notice that a negative correlation exists between ship service speed and suitable rib height which means that it is very essential for a naval architect to conduct the three-step procedure in advance to calculate the suitable rib height for the target ship in order to hit the peak drag-reduction performance. For example, in Table 5.11 and Table 5.12, the suitable rib height for cargo vessel I designed for super slow steaming mode is almost two times as large as that of cargo vessel III designed for the normal sailing mode.

As mentioned in Table 5.4, the values of both h+ and $\Delta U^{+}$are different at their peak drag-reduction performance, which is also reflected in the derived results of suitable riblet height and drag-reduction percentage (DR%) respectively. If the estimated suitable rib heights of two representative coating surfaces are compared at the same sailing mode, it is found that the estimated suitable rib height of the new design surface is much smaller than that of the symmetric v-groove riblet surface. This result is attributed to a smaller h^+ value (h^+=8.76) of the new design surface rather than h^+=13.46 of the symmetric v-groove riblet surface. Moreover, it is found that the drag-reduction performance of the new design surface is superior to the symmetric v-groove riblet surface, where arpproximately 16%-20% drag-reduction performance improvement is found in the new design surface when compared to that of symmetric v-groove riblet. This is due to a larger ΔU^+ value (ΔU^+=0.573) of the new design surface than ΔU^+=0.469 for the symmetric v-groove riblet surface.

5.3.2 General Charts of the Suitable Riblet Coating Size

In Section 5.3.1, the detailed procedure is implied to show the readers how the optimum size of a specific drag-reduction coating is derived if the length and average speed of the target ship is given. The three-step procedure is explained by using a case study of the 100-meter cargo ship sailing at three different average speeds: 12 knots, 20 knots, and 25 knots.

Although the general method of deriving the optimum coating size for a specific ship is explained clearly in the last section, the estimate of optimum coating size has only been done for the specific case. If a naval architect aims to find out the optimum coating size, it will cost him/her a large amount of time to follow the relatively complex similarity law scaling method. Nevertheless, since there are various types of ships sailing at different average speeds in the real world, the same amount of work will be repeated every time the new target ship information is provided. In order to avoid the complex and repetitive work as much as possible, the author aims to establish convenient and useful charts that cover a wide range of ship length and average ship speeds to help a naval architect quickly find out the rough range of the optimum coating size. As a result, the only work left to a naval architect is to carry out Step 3 of the aforementioned procedure, indicated in Section 5.3.1.3, to derive the exact value of the optimum coating size.

Throughout Chapter 5, two representative drag-reduction coatings: symmetric v-groove riblet surface and new design surface are consistently used as the research surfaces. In this section, a broad range of ship length (10m – 400m) and average ship speed (3.67 knots – 55.18 knots for symmetric v-groove riblet surface and 2.31 knots – 35.12 knots for new design surface) is taken into account so that the established charts, as shown in Table 5.13 and Table 5.14 are able to be used for most real cases.

As shown below, there are 14 characteristic ship lengths in the range of 10-400m, within which the ship length increments are respectively 30m, 25m, and 50m for the range of 10-100m, 100-300m, and 300-400m. At the same, there are 13 characteristic riblet heights in the range of 20-200µm, within which the riblet height increments are respectively 10µm and 25µm for the range of 20-100µm and 100-200µm. For each specific ship length and riblet height, the matching average ship speed that maximizes the drag-reduction performance is calculated by the in-house code. All the data within the chart are filled after a large amount of calculation and thus the chart can be used to confirm the rough range of riblet height once the ship length and average ship speed is given.

For example, if the 60° symmetric v-groove riblet coating surface is planned to be used over the underwater ship hull of a 225m KCS ship, whose average ship speed is 24knots. The value of the optimum riblet height can be confirmed to lie between 40-50µm by checking Table 5.13. It must be noted that the current charts are presented here to show its convenience of use. These relatively simple charts can be further extended to include much more refined ship lengths, riblet heights, and other types of the drag-reduction coating surface.

Two diagrams that depict the general relation between suitable riblet height and average ship speed are shown in Figure 5.4 and Figure 5.5.

Table 5.13 General chart for suitable riblet coating size (60-degree symmetric v-groove)

	Ship length (m)													
	10	40	70	100	125	150	175	200	225	250	275	300	350	400
Riblet height (µm)	Ship velocity (knots)													
20	43.75	48.01	49.75	50.85	51.55	52.12	52.60	53.01	53.38	53.71	54.01	54.28	54.76	55.18
30	28.33	31.17	32.33	33.06	33.53	33.90	34.22	34.50	34.74	34.96	35.16	35.34	35.66	35.94
40	20.81	22.94	23.80	24.35	24.70	24.98	25.22	25.43	25.61	25.77	25.92	26.06	26.30	26.51
50	16.37	18.08	18.76	19.20	19.48	19.71	19.90	20.06	20.21	20.34	20.46	20.57	20.76	20.93
60	13.46	14.88	15.45	15.82	16.05	16.23	16.39	16.53	16.65	16.76	16.86	16.95	17.11	17.25
70	11.40	12.62	13.11	13.42	13.62	13.78	13.92	14.03	14.14	14.23	14.32	14.39	14.53	14.65
80	9.88	10.94	11.37	11.64	11.81	11.95	12.07	12.18	12.27	12.35	12.42	12.49	12.61	12.71
90	8.70	9.64	10.02	10.27	10.42	10.54	10.65	10.74	10.82	10.90	10.96	11.02	11.13	11.22
100	7.76	8.61	8.96	9.18	9.31	9.42	9.52	9.60	9.68	9.74	9.80	9.85	9.95	10.03
125	6.10	6.78	7.06	7.23	7.34	7.43	7.51	7.57	7.63	7.68	7.73	7.77	7.85	7.91
150	5.01	5.58	5.80	5.95	6.04	6.12	6.18	6.23	6.28	6.33	6.37	6.40	6.47	6.52
175	4.24	4.73	4.92	5.05	5.13	5.19	5.24	5.29	5.33	5.37	5.40	5.43	5.49	5.53
200	3.67	4.09	4.27	4.37	4.44	4.50	4.55	4.59	4.62	4.66	4.69	4.71	4.76	4.80

Table 5.14 General chart for suitable riblet coating size (New design surface)

	Ship length (m)													
	10	40	70	100	125	150	175	200	225	250	275	300	350	400
Riblet height (µm)	Ship velocity (knots)													
20	27.69	30.47	31.60	32.32	32.77	33.14	33.45	33.72	33.96	34.16	34.36	34.53	34.85	35.12
30	17.93	19.77	20.52	21.00	21.30	21.55	21.75	21.93	22.09	22.23	22.36	22.48	22.69	22.86
40	13.16	14.54	15.10	15.46	15.69	15.87	16.02	16.16	16.28	16.39	16.48	16.57	16.73	16.86
50	10.35	11.45	11.90	12.19	12.37	12.52	12.64	12.75	12.84	12.93	13.00	13.08	13.20	13.31
60	8.50	9.42	9.80	10.04	10.18	10.31	10.41	10.50	10.58	10.65	10.71	10.77	10.88	10.97
70	7.20	7.99	8.31	8.51	8.64	8.75	8.83	8.91	8.98	9.04	9.09	9.15	9.23	9.31
80	6.24	6.92	7.20	7.38	7.49	7.59	7.66	7.73	7.79	7.84	7.89	7.93	8.01	8.08
90	5.49	6.10	6.35	6.51	6.61	6.69	6.76	6.82	6.87	6.92	6.96	7.00	7.07	7.13
100	4.90	5.45	5.67	5.82	5.91	5.98	6.04	6.09	6.14	6.18	6.22	6.26	6.32	6.37
125	3.85	4.29	4.47	4.58	4.65	4.71	4.76	4.80	4.84	4.88	4.91	4.93	4.98	5.03
150	3.16	3.53	3.67	3.77	3.83	3.88	3.92	3.95	3.99	4.01	4.04	4.06	4.10	4.14
175	2.67	2.99	3.11	3.20	3.25	3.29	3.32	3.35	3.38	3.41	3.43	3.45	3.48	3.51
200	2.31	2.59	2.70	2.77	2.81	2.85	2.88	2.91	2.93	2.95	2.97	2.99	3.02	3.05

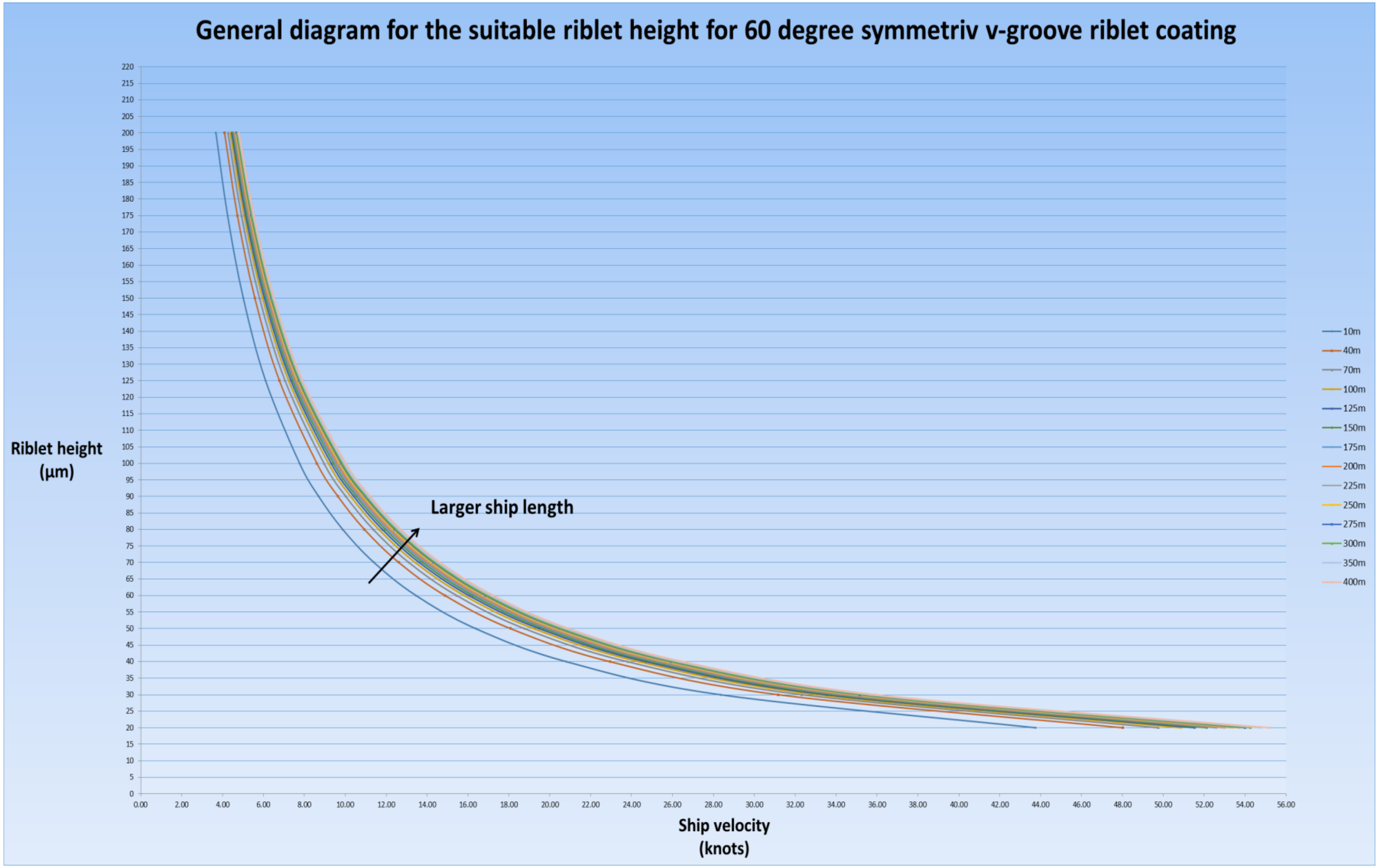

Figure 5.4 General diagram of suitable riblet height for 60-degree symmetric v-groove riblet coating

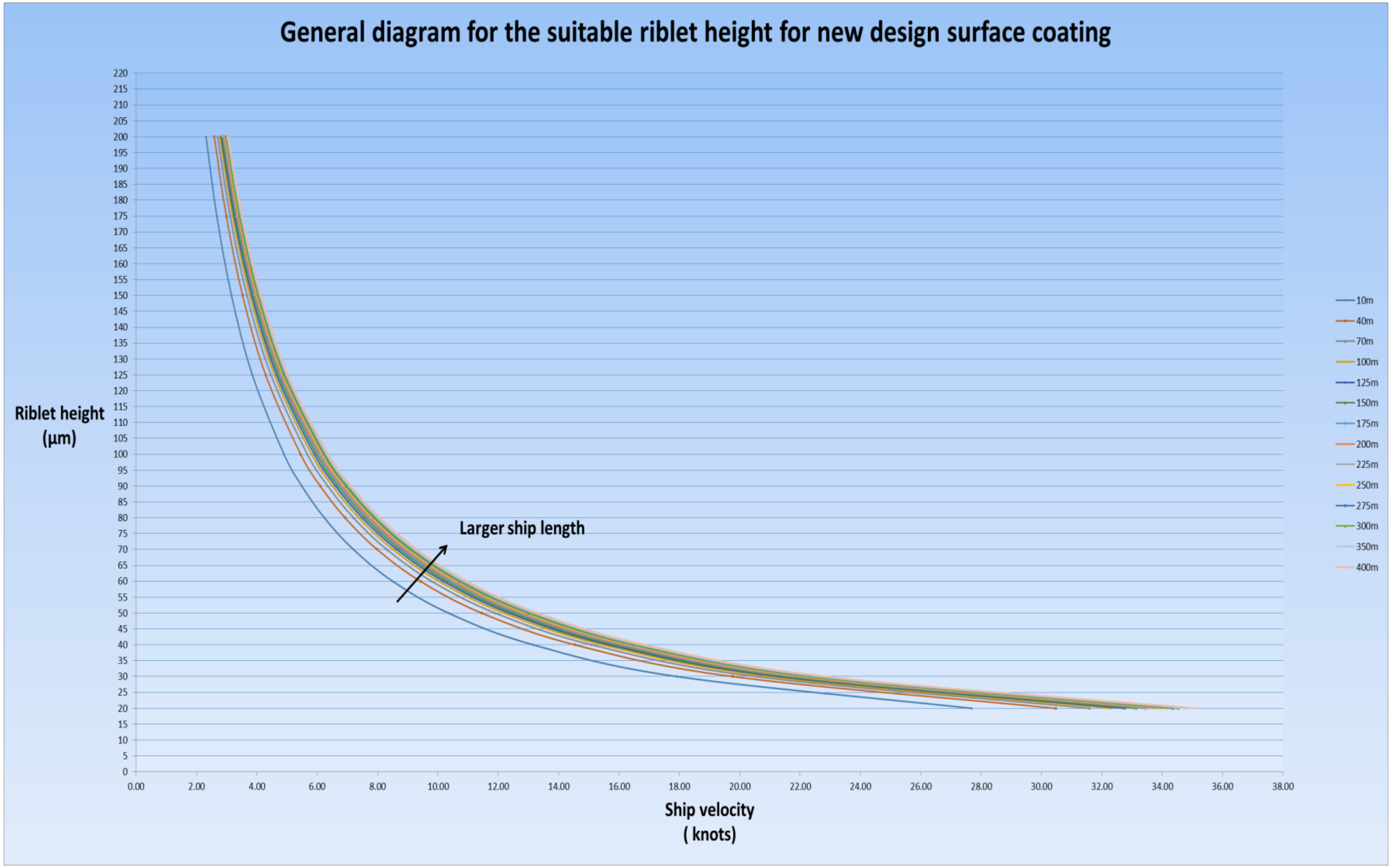

Figure 5.5 General diagram of suitable riblet height for new design surface coating

As mentioned in Section 5.3.1.3, the riblet height should be changed accordingly with the average ship speed, ship length, and types of drag-reduction coating to ensure the maximum drag-reduction performance, which is clearly noticed in Figure 5.4 and Figure 5.5. Generally, a larger riblet height should be used for a higher speed ship and a smaller riblet height for a slower speed ship. In the range of relatively low ship speed, the same amount of change in the ship speed leads to a significant variation of riblet height, which is not really obvious in the range of relatively high ship speed. Moreover, the impact of the ship length on the determination of optimum riblet height is well indicated in the diagrams. It is found that the optimum riblet height increases for larger ships as the same ship speed is maintained.

For each specific riblet coating surface, there is a unique curve of h^+ vs DR% that can be derived using CFD method. The impact of such differences is also reflected in the diagrams shown above. At the same ship speed, the riblet height of the symmetric v-groove is obviously larger than that of the new design surface because symmetric v-groove surface reaches its maximum drag-reduction point at a higher h^+ value.

5.4 Analysis of Riblet Coating's Drag-Reduction Performance along Ship Speed Distribution

As presented in Section 5.3, the optimum coating sizes of two representative surfaces designed for the 100m cargo vessel are derived by following the three-step procedure. For each specific sailing mode, a unique value of riblet height is suggested in order to attain the best drag-reduction performance. Using the average ship speed, which is defined as the speed an ocean-going vessel sails for the longest time during its entire voyage, the suitable riblet coating height can be estimated. However, in the real world, there exists a specific speed distribution during a ship's entire sailing time due to the impact of loading conditions (loaded/ballast), weather, etc. In this section, the drag-reduction performances of two representative coating surfaces are calculated for some case ships based on respective speed distributions.

To meet the various demands of marine cargo transportation, cargo ships come in different types and sizes ranging from the handysize carrier of 15,000 – 35,000 DWT to the ultra-large crude carrier of 550,000 DWT, and mid-sized cargo vessels such as Aframax tanker of 80,000 – 120,000 DWT. The speed distribution information of some case ship types are suggested by the published work of Banks, Turan et al. (2013) and are used in this section to assess the impact of two representative coatings' drag-reduction performance, which will be given as a proportion of the total time sailing during the chosen year.

Table 5.15 Optimum riblet height values for some case ship types

Ship Type Unit	Operation Year	Ship Length m	Service Speed knots	h (Type A) µm	h (Type B) µm
Handysize Vessel	2011	175	12.5	77.7	50.1
Aframax Tanker	2011	245	12.5	79.2	50.6
Suezmax Tanker	2011	285	15.0	67.4	44.4
Post Panamax	2008	290	21.0	49.1	32.4
Container Vessel	2012	290	19.0	54.2	35.8
Post Panamax Plus	2008	335	22.0	47.7	31.1
Container Vessel	2012	335	14.0	72.6	47.6

Notes: h means the riblet coating height; Type A is the symmetric v-groove riblet surface; Type B is the new design surface;

Using the three-step procedure suggested in Section 5.3, the optimum riblet height sizes for two representative coating surfaces are derived for some case ship types with specific ship length and service speed as shown in Table 5.15. All selected case ship types are in consistent with the ones shown in Banks, Turan et al. (2013) so that the information of specific speed distribution can be applied.

For each riblet coating height indicated in Table 5.15, they are designed to provide the case ship types with the best drag-reduction performance at its service speed. The drag-reduction performance of some case ship types is depicted in the following figures by employing the specifically calculated riblet height and their unique speed distributions throughout a year.

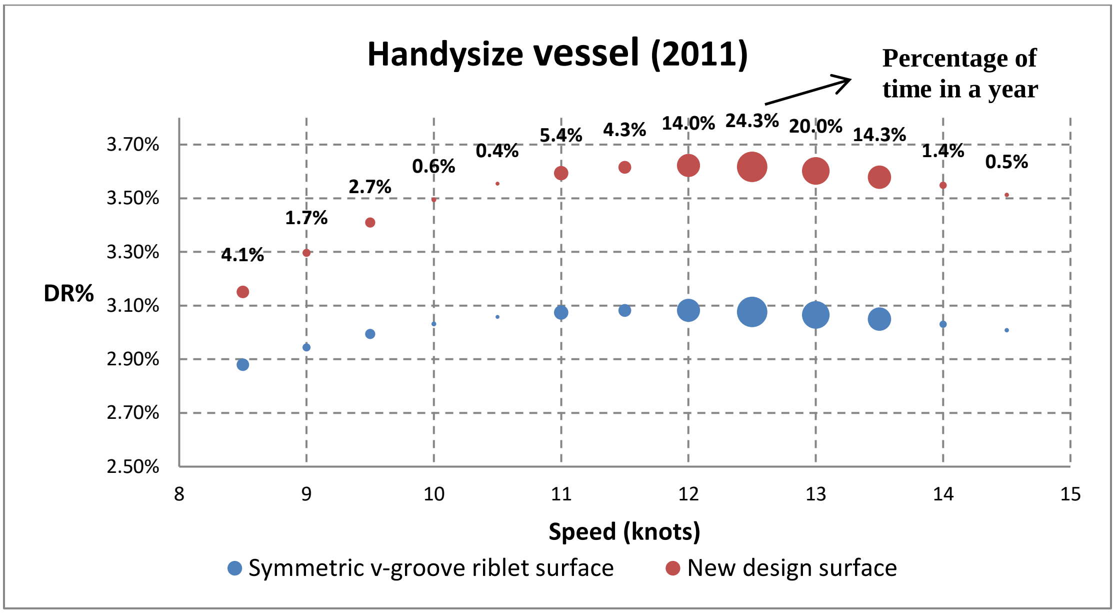

Figure 5.6 Drag-reduction performance of Handysize vessel (2011)

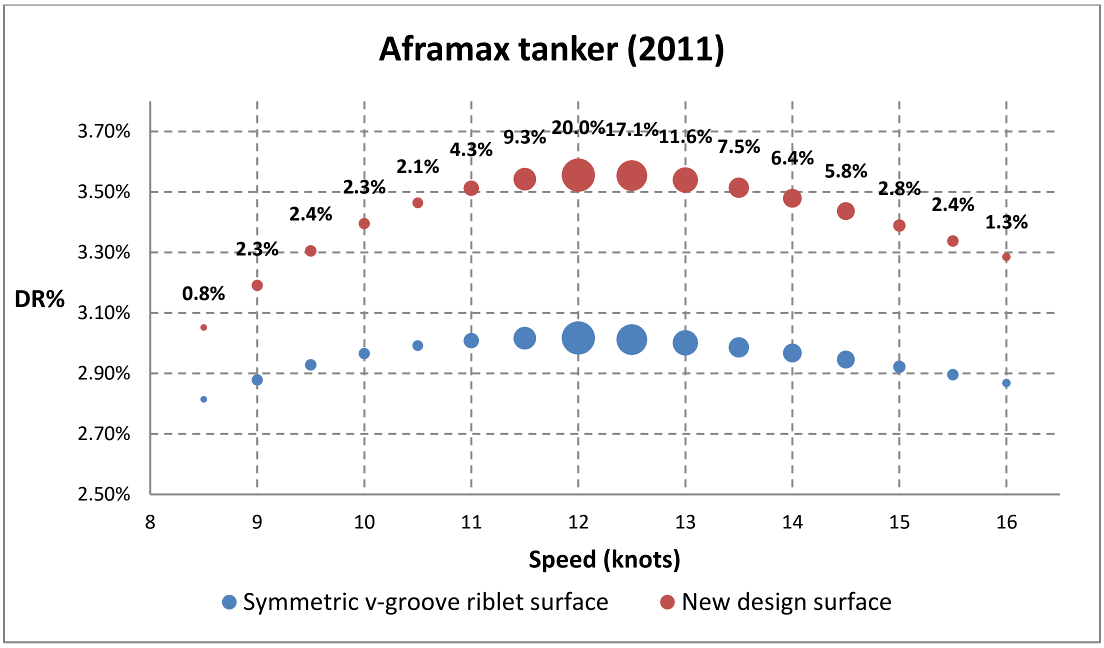

Figure 5.7 Drag-reduction performance of Aframax tanker (2011)

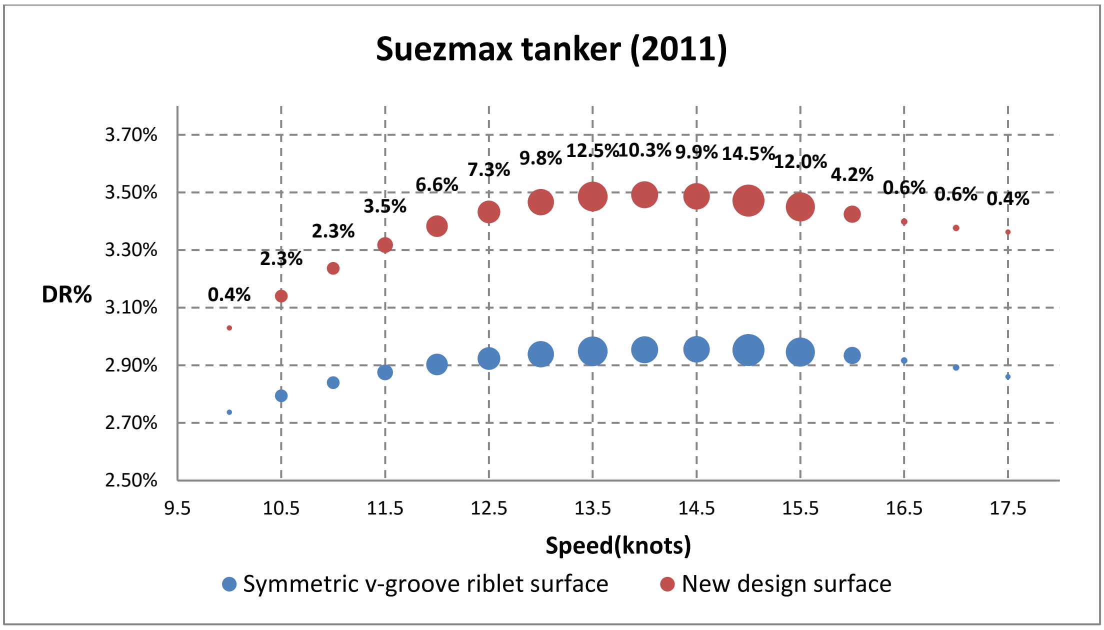

Figure 5.8 Drag-reduction performance of Suezmax tanker (2011)

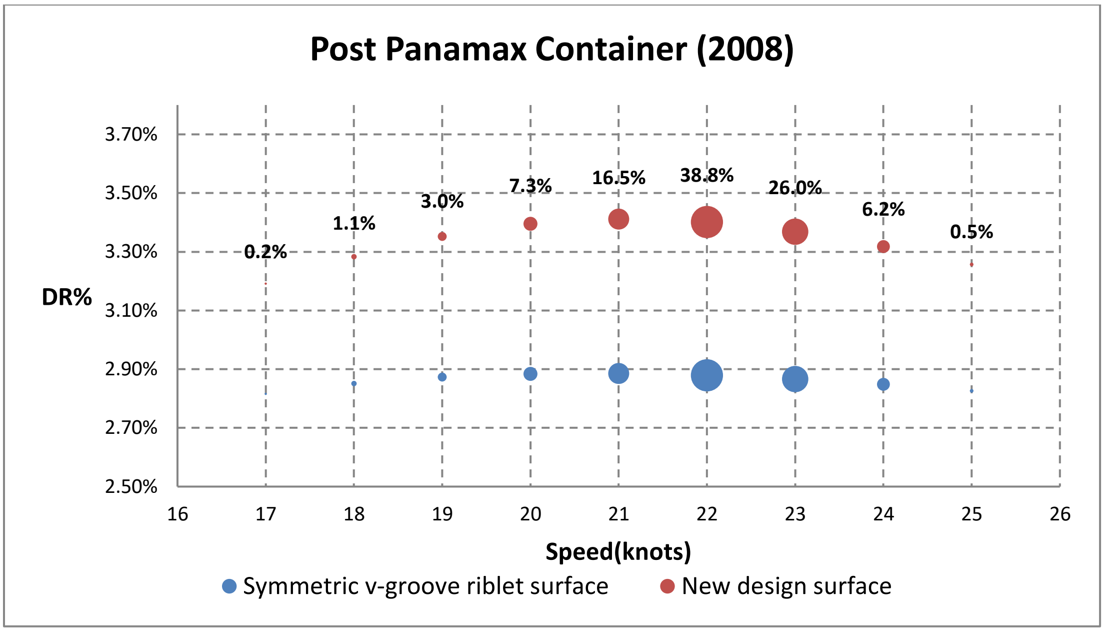

Figure 5.9 Drag-reduction performance of Post Panamax tanker (2008)

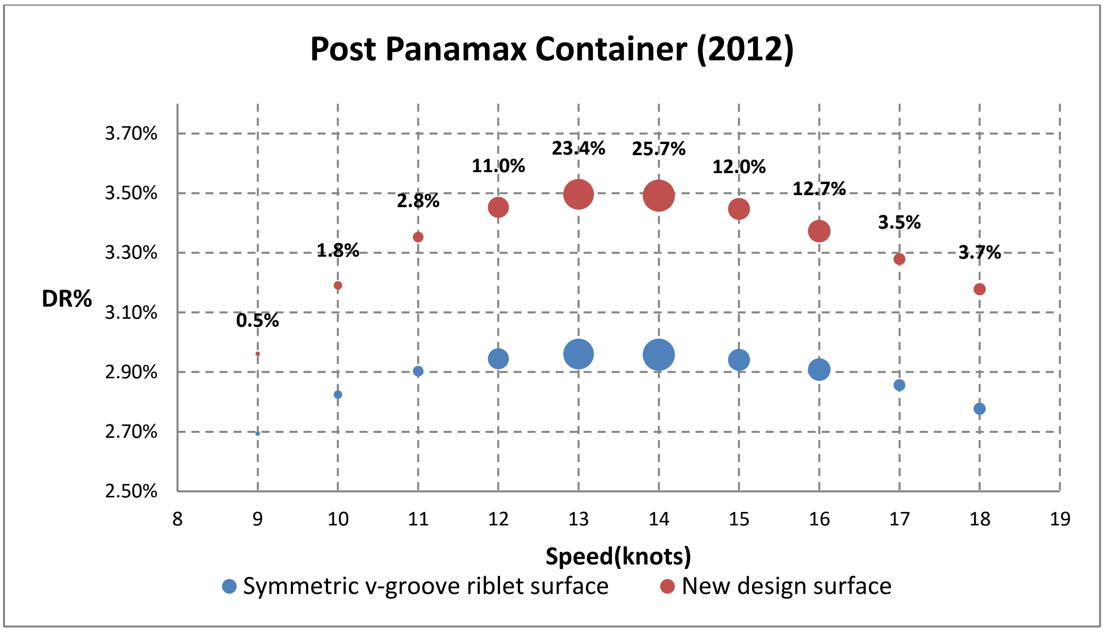

Figure 5.10 Drag-reduction performance of Post Panamax tanker (2012)

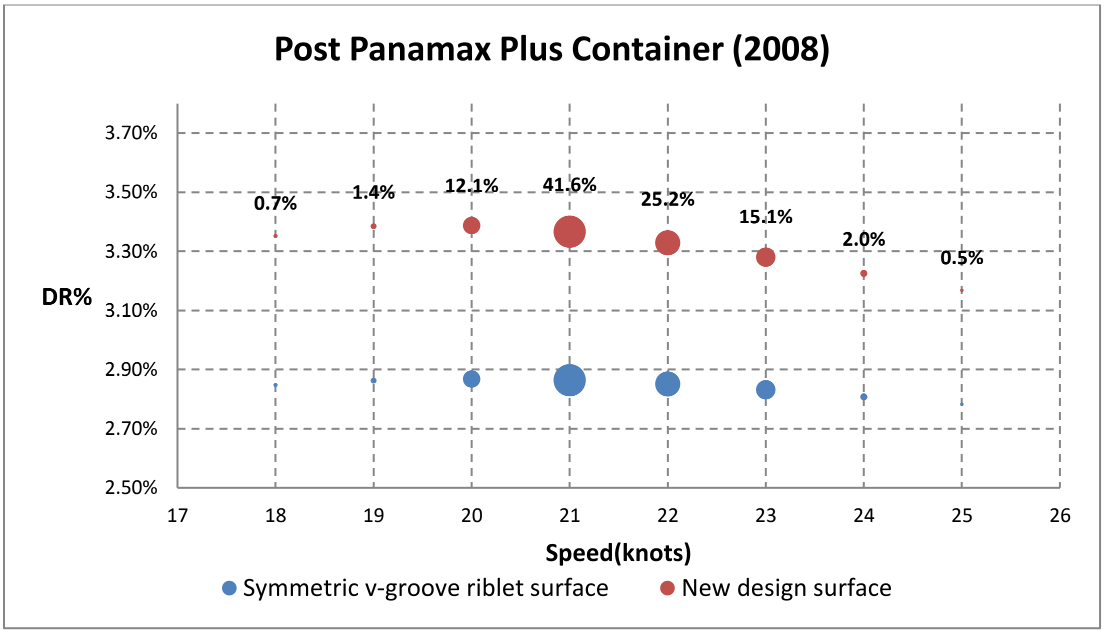

Figure 5.11 Drag-reduction performance of Post Panamax Plus tanker (2008)

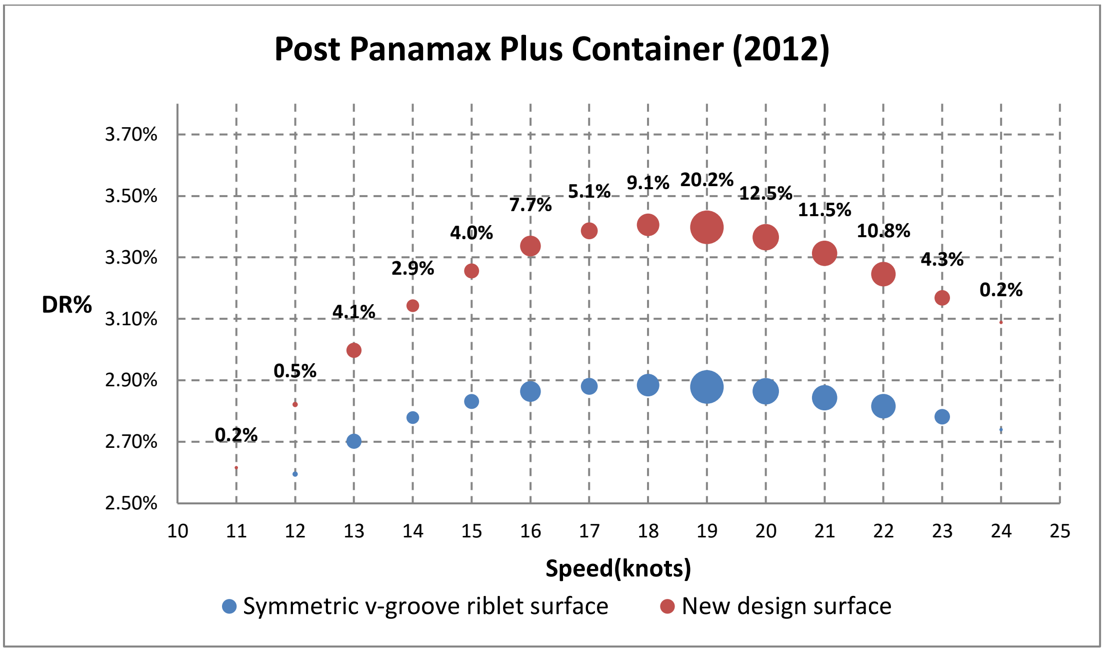

Figure 5.12 Drag-reduction performance of Post Panamax Plus tanker (2012)

As shown in Figure 5.6 – 5.12, the percentage shown above the red bubbles represents the percentage of time in a specific year that a ship spent at the matching speed in the horizontal axis, and so are the diameters of the bubbles. It is found that a good drag-reduction performance is maintained throughout the entire speed distribution range, and a higher drag-reduction percentage is clustered near the service speed, at which the case ship types sail for the largest portion of time in a year. The new design surface exhibits a superior drag-reduction performance to the symmetric v-groove riblet surface throughout the entire speed range. Moreover, the superiority of the new design surface is found to hit the peak near the service speed, which ensures better energy efficiency in most of the ship’s operation time. For example, approximately 18.3% drag-reduction improvement is estimated for Suezmax tanker (2011) hypothetically covered with new design surface when compared to symmetric v-groove riblet. As shown in these figures, the exact value of DR% varies with the unique riblet coating surface, ship service speed, and ship types. The maximum drag-reduction performance respectively maintains at roughly 2.9%-3.1% and 3.4%-3.6% for symmetric v-groove riblet and new design surface respectively, whose impact on shipping companies will be more directly exposed in the next section in terms of ship fuel savings.

5.5 Predicting the Effect of Riblet Coating on Ship Fuel Consumption

Although the drag-reduction performance of two representative coatings, hypothetically coated with underwater ship hull surface of five case ships, has been quantified in Section 5.4, it is believed by the author that converting the drag-reduction performance to ship fuel saving will provide more insights to ship owners.

The mass change of ship fuel saving (Δm) is defined by Eq.61.

$$\Delta m = \frac{\sum_i \Delta P_{E_i} \times T_i}{CV \times \eta \times \eta_P} \tag{61}$$

Where

- i: representation of every speed within the specific speed distribution based on the work of Banks, Turan et al. (2013).
- ΔP_E: Change of effective power.
- T: Voyage time at particular speed distribution.
- CV: The calorific value of ship fuel oil, and Heavy Fuel Oil (HFO) is used here, 41KJ/g.
- η: Net energy engine efficiency, typically 40% (USNA)
- η_P: Propulsive efficiency, typically range from 55% to 75% (USNA)
- Specific Fuel Oil Consumption (SFOC) is assumed to be constant with varying effective power.

The change of effective power is the power that is saved by the riblet coating to move the ship's hull at a given speed and is defined in Eq.62.

$$\Delta P_E = \Delta R_T * V = \frac{1}{2}\Delta C_f \rho S V^3 \tag{62}$$

Where:

- ΔR_T: Change in total ship resistance, which is calculated by $R_{T\_smooth} - R_{T_{riblet}} \approx R_{f_{smooth}} - R_{f_{riblet}}$.
- V: Ship speed.

- ΔC_f: Change of friction coefficient due to the riblet coating, which is calculated by $\Delta C_{f\_smooth} - \Delta C_{f_{riblet}}$.
- S: Wetted surface area, which is calculated by $volume^{\frac{2}{3}} \times (3.4 + \frac{L}{2 * volume^{\frac{1}{3}}})$ (Papanikolaou 2014)

Based on the above equations, a rough estimate of five case ships' fuel savings are calculated and presented in Table 5.16.

Table 5.16 Estimate of ship fuel saving due to two representative riblet coating surfaces

Ship Type	Operation Year	∇	Voyage Time in a Year (%)	Δm (Type A)	Δm (Type B)
Unit		m^3		tonne	tonne
Handysize Vessel	2011	32,000	43%	37 - 50	43 - 59
Aframax Tanker	2011	100,000	51%	96 - 131	113 - 153
Suezmax Tanker	2011	160,000	63%	207 -282	243 - 331
Post Panamax	2008	100,000	64%	613 - 836	772 -985
Container Vessel	2012		75%	201 - 274	235 - 321
Post Panamax Plus	2008	160,000	72%	850 - 1159	995 - 1356
Container Vessel	2012		68%	538 - 733	627 - 855

Notes: h means the riblet coating height; Type A is the symmetric v-groove riblet surface; Type B is the new design surface; Voyage Time in a Year (%) is mentioned as the % of year that a ship is moving rather than in port.

Currently, heavy fuel oil costs around \$600 per tonne and is expected to increase to \$1000 by 2020 as suggested by Munthe-Kaas, an analyst and broker at Wilhelmsen Premier Marine Fuels. These numbers are astronomical for shipping companies who are used to run a business on cheap fuel oil. As a result, even a small drag-reduction percentage induced by the riblet coating surface could help reduce a lot of money for the shipping companies. For example, in 2008 the hypothetical application of new design surface on Post Panamax Plus Container Vessel only contributes to a drag-reduction percentage of roughly 3.4%, but almost 995 to 1356 tonnes HFO are estimated to be saved that year, and thus a saving of 0.6 – 0.8 million US dollars for a single ship in a year based on \$600/tonne.

As indicated in Table 5.16, the fuel saving performance is closely associated with ship types, operating speed, and voyage time. Compared to other case ships, Handysize vessel has the smallest deadweight and voyage time and is operated in the super slow steaming mode. Thus, it benefits least from the riblet coating surface. However, as ships become larger and operating speed increases, the benefits of using riblet coating surface are more obvious. From 2008 to 2012, the service speed of Post Panamax Container Vessel shown in Table 5.16 drops from 22knots to 14knots which leads to roughly 70% less fuel saving.

5.6 Chapter Summary

The research work conducted in this chapter tends to emphasize more about the practical investigations of a full-scale ship condition. The similarity law scaling method proposed by Granville is employed in this study to extend the drag-reduction results from channel flow scale to full ship length scale. Two representative drag-reduction surfaces: symmetric v-groove riblet surface and new design surface, which are respectively presented in Chapter 3 and Chapter 4, are employed here for a case study. Different from the traditional similarity law scaling method, no experimental towing test of the model-scale flat plate is conducted in this work due to the unavailability of manufacturing the specific drag-reduction surface. Instead, specific roughness function is derived from the numerically calculated drag-reduction results and is further used as an important input while conducting the similarity law scaling procedure.

Based on the similarity law scaling procedure, an in-house code was developed by the author to achieve numerical automation. A three-step procedure is proposed in this chapter to explain the fundamental workflow to determine the suitable riblet coating size for a ship, hypothetically coated with the drag-reduction surface. General charts of two representative drag-reduction surfaces are established and expected to serve as a reference dataset to help a naval architect quickly confirm the rough range of a suitable riblet height if either of two representative surfaces is used. The reference dataset can be extended to other drag-reduction surfaces as well if matching precursor numerical tests are completed.

Following the work of suitable riblet height calculation, the drag-reduction performance of two representative surfaces, hypothetically coated on some case ship types are investigated. The statistical information of target ships' speed distribution (Banks, Turan et al. (2013)) is employed to depict how the drag-reduction coating surface performs at different speeds throughout the entire year. In addition, the impact of the riblet coating surface on the shipping companies is more directly reflected by the discussion of the amount of ship fuel savings. The suitable riblet height determined by three-step procedure achieves to attain peak drag-reduction performance over the largest portion of a year. New design surface indicates a better drag-reduction performance, and thus less fuel consumption and GHG emissions than the symmetric v-groove riblet surface.

6. Discussion

6.1 Introduction

Following the research aims and objectives proposed in Section 1.4, the achievements and outputs of this research are summarized in this section. The novel contribution of current work to the field of the study fills the gaps where not enough work has been done. The existing difficulties and imperfections of current work are summarized and the future developments are concluded.

6.2 Achievements of Research Aims and Objectives

The main aim of this thesis is to assess the feasibility of developing a new biomimetic energy-saving ship coating surface which is inspired by shark skin. The ultimate aim was achieved by conducting novel studies within each chapter, as discussed below.

- Chapter 2

The following research objective is achieved:

- ➢ *"To develop a new micro-patterned surface that is expected to possess dual function (drag-reduction and fouling-control)."*

Concerning the serious environmental impact of ship exhaust and biocide-based coating systems, legislative frameworks have been established to regulate ship energy efficiency and the use of toxic ship coating systems. Recent technical advancements in the fields of drag-reduction technologies and post-TBT Anti-Fouling systems have been reviewed in Chapter 2.

As the specific dermal denticles covered with shark skin surface are known to aid fast-swimming sharks in hydrodynamic and Anti-Fouling performance in a purely physical way when moving in the water, the author realized that a new biomimetic surface, which is inspired by the shark skin surface, might be a promising solution to the current legislative frameworks. Following this idea, the literature of shark skin surface was reviewed, focusing on the general perspective, microstructure, drag reduction, and fouling-control properties. Two existing shark skin inspired technologies: riblet drag-reduction structure and Sharklet AF^{TM} Anti-Fouling pattern are incorporated into the formation of the new design surface idea.

- Chapter 3

The following research objectives are achieved:

- *"To establish a plausible CFD model so that a correct frictional resistance of the target plate of the fully-developed turbulent channel flow can be predicted."*
- *"To examine if the Realizable k-epsilon two-layer (RKE 2L) turbulence model is capable of reproducing the drag-reduction performance of the riblet structure."*
- *"To derive the possible drag-reduction mechanism of the classical symmetric v-groove riblet based on the numerically obtained lower-order turbulent statistics, and to justify the findings with existing riblet drag-reduction mechanism."*

In this chapter, the validation test of a traditional symmetric v-groove riblet surface is conducted in a fully developed turbulent channel flow to examine if correct frictional resistance of target plate can be predicted and if the impact of surface topography on the near-wall turbulent activities can be captured. Based on the numerical analysis of the CFD simulations, possible drag-reduction mechanism of symmetric v-groove riblet surface was also summarized.

The estimate of the drag-reduction performance against the non-dimensional riblet spacing is generally in accord with the summarized experimental data band for the symmetric v-groove riblet surface. However, the drag-reduction percentage is overestimated when s^+ exceeds the optimum value. As depicted in Figure 3.5, the drag-reduction performance of the riblet surface was also overestimated in the work of Launder and Li (1993) because both turbulent models lack the ability to reproduce any turbulent driven secondary motions. It is assumed by the author that the effect of lacking secondary turbulent coherent motions, such as ejection and sweep that always occur in the buffer layer, becomes more significant at higher speed or h^+ values and might lead to an insufficient estimate of the kinematic momentum exchange, and ultimately overestimate of drag-reduction performance. Despite the fact that the current RANS results can only partly reflect the real drag-reduction performance of symmetric v-groove riblet where s^+ is no bigger than the optimum value, It is still unlikely that there will be any significant errors incurred in using the RKE 2L turbulence model as an auxiliary tool to predict the new design surface's drag-reduction performance.

Considering the restriction of the current RANS turbulence model, the author has also spent a long time attempting to employ Large Eddy Simulation (LES) turbulence model in STAR-CCM+ to collect higher-order turbulent statistics and to capture the secondary turbulent driven structures in the near wall turbulent boundary layer. However, the LES simulation of the riblet surface in the turbulent channel flow is never successfully modelled because of some unsolved problems, such as the unsustainable turbulent vortical structures, overestimated (roughly double the desired value) skin friction. The unsuccessful STAR-CCM+ modelling experience drives the author to use alternative CFD software, OpenFOAM to conduct the LES study because OpenFOAM is open source and thus more flexible and adaptable. The initial LES work of a plane channel flow has been successfully conducted by using adjusted C++ files and a self-defined initial perturbation to generate sustainable turbulent coherent motions in the turbulent boundary layer. However, due to the timeline of Ph.D. completion, the research is stopped here and listed as a future research direction.

- Chapter 4

The following research objectives are achieved:

- *"To investigate if the new micro-patterned surface possesses drag-reduction property using CFD techniques."*

- *"To conduct a parametric study of the new design surface so that the impact of geometric variation on the drag-reduction performance and near-wall turbulent activities can be better understood."*

- *"To provide an initial guess of the optimum new design surface geometry."*

- *"To conduct preliminary investigation on the fouling-control performance of the new micro-patterned surface using results obtained from numerical simulations."*

In this chapter, a detailed hydrodynamic analysis of the new design surface was conducted by employing the numerically validated CFD model. Initial drag-reduction performance has been indicated in the preliminary CFD results of the new design surface. A systematic parametric study was subsequently conducted for the new design surface to assess the effects of three important variables: velocity, rib height, and rib spacing, on its drag-reduction performance, and confirmed its drag-reduction performance. The key attributes that an optimum design should possess are also indicated. Case 12 (h^+=13.3, s^+=10.8) is the best performing configurations out of those considered in the parametric study. The new design surface is found to have a better drag-reduction performance (8.53%) than the traditional 60° symmetric v-groove riblet surface (6.80%). In contrast with the continuous spaced v-groove riblet surface, the existence of the streamwise surface discontinuity of the new design surface was numerically verified to improve its drag-reduction performance. It is found that the peak drag-reduction percentage of the trapezoidal riblet is approximately 0.6% smaller than the new design surface. The research work conducted in Chapter 4 not only enriched the understanding of the new design surface's hydrodynamic performance but also highlights the possible directions that the design could be further improved. The fouling-control performance of new surface is likely to have a superior performance near the tip region than the smooth surface, and for the relatively larger marine organisms such as tubeworm larva and barnacle cypris larva.

- Chapter 5

The following research objectives are achieved:

- *"To extend the drag-reduction effect from the small channel flow scale to the full ship length scale by employing the similarity law scaling procedure."*

- *"To provide an approach that determines the optimum drag-reduction coating size so that the peak drag-reduction performance could be attained in the most time of sailing."*

- *"To take the existing yearly speed distribution into account and explore the fuel savings and how the drag-reduction coating will perform in a practical sailing condition for various ship types."*

In this chapter, the research work is extended from the millimetre scale of a turbulent channel flow to a more realistic problem of full-scale ships. The similarity law scaling method was converted into an in-house code by the author to predict the frictional resistance of flat plates of full-scale ship length. The workflow to derive the optimum riblet coating size is depicted as a three-step procedure, and two general charts of two representative surfaces are presented as an example to make it convenient for a naval architect to quickly find out the rough range of the suitable riblet coating size. Concerning the fact that a seagoing ship's speed is not constant throughout the entire year, the unique speed distribution for various ship types is taken into account to present a big picture of how a specific drag-reduction coating performs at different speeds. For all five case ships studied, the new design surface indicates a drag-reduction performance of roughly 3.4%-3.6% and approximately 18.3% drag-reduction improvement in the case of Suezmax tanker (2011) when compared to symmetric v-groove riblet surface. When converting the drag-reduction percentage to fuel consumption, the author found the shipping companies could benefit a lot from the riblet coating surface. For example, approximately 995-1356 tonnes of HFO and equivalent 0.6 – 0.8 million US dollars were estimated to be saved for operating a Post Panamax Plus Container Vessel hypothetically covered with new design surface coating in the entire year of 2008.

6.3 Novelties and Contributions to the Field

The contributions of this Ph.D. work could be concluded as the following points:

- New energy efficient approach based on unique surface hull treatment

To the best of the author's knowledge, the new design surface is unique and has never been proposed in any other publications. The topography of the new surface is inspired by two existing technologies: riblet structure and Sharklet AF^{TM} design. The new design surface may be regarded as a new type of energy efficient ship coating. Compared to the traditional symmetric v-groove riblet surface, a superior drag-reduction performance (up to 18.3% improvement) was observed for the new design surface in the full-scale ship case. Compared to the trapezoidal riblet surface, up to 8.2% improvement was observed for the new design surface based on the results of CFD simulations. It needs to be noted that the anti-fouling performance of the new design surface is expected to be retained by the new surface because the same pattern as Sharklet AF^{TM}, which has been experimentally verified to reduce bacteria attachment by up to 86%, is maintained in the new design surface

- Assess the applicability of engineering turbulence model on riblet drag-reduction structure

DNS, as the most accurate approach to turbulence simulation, is superior to LES or RANS methods because no approximation or averaging is made and thus the error can be estimated and controlled (Ferziger and Peric 2002). To some extent, DNS can be seen as numerical experiments which provides equivalent flow visualizations. However, its application is only possible for simple flows at low Reynolds numbers on High-Performance Computers (HPC) since the grid must be no larger than the Kolmogoroff scale, η, in order to capture the kinetic energy dissipation.

- Numerical investigation of new design surface via engineering turbulence model

The proposed new design surface is numerically studied with the engineering turbulence model, which has been validated in Chapter 3. The hydrodynamic benefits of the design surface are firstly verified in this study. The drag reduction performance at a relatively broad range of rib height (h^+) has been calculated and compared to the geometrically similar spaced V-groove riblet. A parametric study of three variables: flow velocity, rib height, rib spacing has been conducted to provide insights into the most optimum surface structure based on the riblet drag reduction mechanism.

- Develop an in-house code to predict the drag-reduction performance of full-scale ship covered with a drag-reduction coating

Little work has been done to analyse the method of deriving the optimum size of a specific drag-reduction surface, hypothetically coated over a target ship. A three-step procedure, which is based on the similarity law scaling method and precursor numerical simulations, is proposed in this work to calculate the optimum coating size. Concerning the convenience of practical use, general charts are provided as an example to help a naval architect quickly confirm the rough range of optimum coating size. In addition, due to the existence of ship speed distribution in the real world, the drag-reduction performance of two representative coating surfaces is presented based on the statistics of some case ship types.

6.4 Restrictions and Imperfections

Inevitably, restrictions and imperfections of this Ph.D. work do exist. They are concluded and summarized hereby.

- Insufficient work on the investigation of the fine-scale secondary flow structure

Although the use of engineering turbulence model has been proven to provide a relatively good estimate of riblet drag-reduction performance with less computational cost, it does not dip deep inside the fine-scale secondary flow structure in the near wall region. The mathematical method could be used to post-process the DNS results to obtain higher-order statistics such as skewness, flatness, which could reflect the coherent motions in the near wall region. Moreover, the quadrant-splitting technique could be used to post-process the DNS results to see how the vortical structure is affected by the riblet structure and get some more insights of the drag-reduction mechanism.

- The imperfection of riblet drag-reduction performance when rib spacing (s^+) is significantly larger than the optimum value

As shown in Chapter 4, the validation test of v-groove riblet test indicates that the estimated DR% decreases slower compared to the experimental results. Despite the imperfection of the current CFD model, it is still an option to deduce the drag-reduction property of microscale surfaces since a relatively accurate result could be obtained when s^+ is not much bigger than the optimum value.

It is essential to point out that in Chapter 5, the drag-reduction performance calculated by the current CFD model is used as input, but the problem of inaccurate prediction in the latter s^+ or h^+ range has been avoided by only using the relation between optimum h^+ and ΔU^+ that could be accurately predicted with the current CFD model. Later research on the overall performance of specific drag-reduction coating is carried out by calculating the empiric formula between h^+ and ΔU^+ suggested by the Aupoix, Pailhas et al. (2012).

- Determination of ΔU^+

For the developed mode proposed in Chapter 5, one of its significance is that it could simplify the traditional full-scale ship performance estimation process by employing the numerically calculated results of the drag-reduction coating. The impact of the drag-reduction coating on the turbulent boundary layer is reflected by the relation between h^+ and ΔU^+, which cannot be derived directly in the internal channel flow as explained in Section 5.2. As a result, an alternative method (Eq.58) is used in this work to derive the relationship. However, this formula is actually used to derive the relationship for the external turbulent flow over flat plates. Fortunately, the value of ΔU^+ calculated by the formula falls between the summarized experimental ranges of ΔU^+. Although the alternative method is robust enough to derive the relation between h^+ and $\Delta U^+$from the numerical results, a more appropriate method is needed for a more accurate derivation.

- Fouling-control performance of new design surface

It is important to indicate that the fouling-control property of the new design surface is only studied by comparing wall shear stress between new surface and smooth surface. As the new surface is currently unavailable to be manufactured, there is no relevant experimental work on the fouling-control investigations.

6.5 Future Work

According to the conclusions of the current study and discovered restrictions and imperfections of the Ph.D. work, suggestions for the future work are given in this section.

- DNS or LES simulation of turbulent channel flow covered with new design surface to investigate the effect of surface topography on the near wall coherent motions (low-speed streak, ejections, sweeps, and vortical structures) by applying a quadrant-splitting technique or mathematical methods to post-process instantaneous results.
- Since the current commercial code might not be robust enough to obtain an accurate estimate of riblet drag-reduction performance in the latter part of the s^+ range, future work is needed to improve the results.
- A more appropriate method is needed to derive the relation between h^+ and ΔU^+ for the internal channel flow instead of Eq.58 (originally used for external flow over flat plates) that is currently employed,
- The fouling-control property of the new design surface needs to be examined. Since the microstructure of the new surface is enlarged compared to the Sharklet AF^{TM} product, the surface ability to repel marine organisms is questionable. However, the cleanness requirement for ship surface is much lower than the medical product, which makes it possible for our design surface to become dual functional.
- It has been demonstrated by many researchers that a lower number of marine bacteria and diatoms is attached to low energy surface compared to high energy

surface and the adhesion strength of micro-fouler on low energy surface is also weaker than high-energy surface which forms the basis for Foul Release Coatings (FRC). The feasibility of modifying existing commercialized FRC for new design surface can be a promising solution for practical application. Moreover, combining different length scales on the new design surface may well function effectively as a universal fouling-control approach to prevent the colonization of marine organisms of different length scales.

- The possibility to make the new design surface silicone-based could be assessed in the future. If silicone material could be well incorporated into the drag-reduction coating, the surface will become so slippery that no weed or mollusc can get a grip on the hull. As a result, the future study could focus on the fouling-control performance of the new silicone-based surface, structural strength, and maturity of the manufacturing technique. The limitations of the current research work and future research are highlighted.
- Experimental work of the new design surface should be conducted in the future to give the exact scenario in the real world. Attempts to print the new design surface have been made but it is currently not possible due to the unavailability of printing capability within the author's reach in terms of cost and capability. However, current research work has paved the way to produce such surface physically in the future.

6.6 Conclusions

The study is motivated by the concern of increasingly stringent legislative frameworks aiming to inhibit the negative environmental impact caused by the shipping industry, particularly extravagant diesel exhaust and wide use of toxic biocide-based anti-fouling systems. The new surface pattern, inspired by the unique structure of dermal denticles discovered on shark skin, is created by combining two surface technologies: riblet and Sharklet AF^{TM} and is expected to improve energy efficiency by reducing ship's frictional resistance and preventing the attachment of marine biofouling in an environmentally benign approach.

Computational Fluid Dynamics (CFD) method is the main approach used in this research to investigate the drag-reduction performance of the new surface pattern. The specific Realizable K-Epsilon two-layer turbulence model is employed due to less computational time (less mesh), lower computational cost (fewer core hours) than Direct Numerical Simulation (DNS) and acceptable accuracy of results which is validated by a case study of symmetric v-groove riblet surface. The results of validation case study indicate the impact of surface topography on the near-wall turbulent boundary layer is correctly modelled by examining key parameters, such as skin friction, mean velocity profile, and turbulent kinetic energy against representative published results.

The drag-reduction performance of new surface pattern is confirmed by both a direct observation of smaller skin friction over the new surface pattern than the plane surface and an upward shift of non-dimensionalized U^+ in the plot of the mean velocity profile. Three parameters of interest: flow velocity, rib height, and rib spacing are considered for a parametric study along with the discussion of possible drag-reduction mechanism and optimum design criteria. To investigate the impact of riblet discontinuity of new surface pattern, the unique discontinuous feature of the new surface pattern is compared with spaced v-groove riblet and verified to slightly improve drag-reduction performance.

To predict the impact of riblet coating surface on full-scale ship which cannot be easily realized by CFD method due to the astronomical number of mesh, the similarity law scaling method is adjusted and written into in-house code by the author because it is believed that the drag-reduction study for a full-scale ship can serve as a good guideline for naval architects to understand the impact of riblet coating surface on ship's frictional resistance, fuel consumption, etc. In practical, suitable riblet coating size is a parameter to be determined because it helps to maximize riblet coating's drag reduction performance and thus the three-step procedure is proposed to practically find the optimum riblet coating size. Moreover, general charts can be established to make it easier for a naval architect to confirm the rough range of optimum coating size concerning various ship lengths, service speeds, and riblet coating types. The impact of the riblet coating surface on the full-scale ship is further investigated by considering real-world case ship types and relevant speed distribution, the financial benefit of using riblet coating surface is successfully estimated.

The conclusions on the work performed within this thesis can be concluded that

- Proposed hybrid surface pattern has a superior drag-reduction performance to the traditional symmetric v-groove riblet as a larger value of drag-reduction percentage of 8.53% and 3.7% are respectively discovered for the channel flow and ship study.

- Proposed hybrid surface pattern thickens the buffer layer and effectively inhibits the near-wall turbulent activities. The existence of geometry discontinuity does not weaken the proposed surface’s drag-reduction performance, as a small drag-reduction improvement is discovered when compared to the trapezoidal riblet surface.

- Proposed hybrid surface pattern has the potential to possess fouling-control performance concerning the specific surface pattern, species-specific length-scale, and violent turbulent activities above the surface. However, only wall shear stress comparison between the wall shear stress of new surface and smooth surface is conducted. Currently, no experimental work has been done to prove that the new design surface possesses fouling-control property.

- Proposed hybrid surface pattern exhibits larger wall shear stress near the tip region and thus is more likely to resist the colonization of micro-fouler. Current length scale of the new surface may well inhibit the colonization of relatively larger marine organisms such as tubeworm larva and barnacle cypris larva.

- Proposed hybrid surface pattern would be a promising ship coating due to its environment-friendly working mechanism and the capability to reduce fuel cost, for example, almost 0.6-0.8 million dollars can be saved for a Post Panamax Plus Vessel operated in 2008.

- Proposed three-step procedure and general riblet coating charts are useful guidelines for a naval architect to derive the suitable riblet coating size.

- The RANS turbulence model, RKE 2L, is a good engineering approach to predict the proposed surface's drag-reduction performance when s^+ is no bigger than the optimum value (normal 15-20 wall units). It is believed that this range of s^+ would be sufficient to test the benefits of any proposed surfaces for a ship.

- For engineering applications of any proposed surface, DNS offers far more information than any engineer needs and is too expensive to be employed and therefore is not recommended to be used as a design tool.

To sum up, the author believes that the shark skin inspired micro-patterned surface would pave a basement for the road to new innovative energy efficient approaches for the shipping industry.

Reference

AMBIO. (2010). "Adcanced nanostructured surfaces for the control of biofouling." from https://cordis.europa.eu/project/rcn/74846_en.html.

Anselmet, F., L. Fulachier, E. Coustols and J. Cousteix (1986). "Flow visualizations and laser measurements in a turbulent boundary layer on a riblet surface." Presented at European Meeting on turbulent drag reduction by passive means conference.

Archambeau, F., N. Mechitoua and M. Sakiz (2004). "Code_saturne: a finite volume code for the computation of turbulent incompressible flows - industrial applications." Int. J. Fin. 1.

Aupoix, B., G. Pailhas and R. Houdeville (2012). "Towards a general strategy to model riblet effects." AIAA Journal 50(No.3).

Bacher, E. V. and C. R. Smith (1985). "A combined visualization-anemometry study of the turbulent drag reducing mechanisms of triangular micro-groove surface modifications." AIAA Journal Vol. 85: pp. 05-48.

Bacher, E. V. and C. R. Smith (1985). "Turbulent boundary layer modification by surface riblets." AIAA Shear Flow Control Conference Vol. 85: pp. 05 - 48.

Banerjee, I., R. C. Pangule and R. S. Kane (2011). "Antifouling Coatings: Recent Developments in the Design of Surfaces That Prevent Fouling by Proteins, Bacteria, and Marine Organisms." Advanced Materials 23(6): 690-718.

Banks, C., O. Turan, A. Incecik, G. Theotokatos, S. Izkan, C. Shewell and X. Tian (2013). Understanding ship operation profiles with an aim to improve energy efficiency ship operations. Low Carbon Shipping Conference. London.

Baum, C., W. Meyer, R. Stelzer, L.-G. Fleischer and D. Siebers (2002). "Average nanorough skin surface of the pilot whale (Globicephala melas, Delphinidae): considerations on the self-cleaning abilities based on nanoroughness." Marine Biology 140(3): 653-657.

Beauchamp, C. H. and R. B. Philips (1988). Riblet and polymer drag reduction on an axismmetric body. Symposium on Hydrodynamic Performance Enhancement for Marine Applications. Newport, RI.

Bechert, D. W. (1985). "On the drag reduction of the shark skin." AIAA Journal Vol. 85(pp. 05-46).

Bechert, D. W. and M. Bartenwerfer (1989). "The viscous flow on surfaces with longitudinal ribs."

Bechert, D. W., M. Bruse, W. Hage, J. G. T. V. D. Hoeven and G. Hoppe (1997). "Experiments on drag-reducing surfaces and their optimization with an adjustable geometry."

Benhalilou, M., F. Anselmet, J. Liandrat and L. Fulachier (1991). "Experimental and numerical investigation of a turbulent boundary layer over riblets." In Proc. 8th Symp. on turbulent shear flows: 18.15.11-18.15.16.

Bers, A. V. and M. Wahl (2004). "The Influence of Natural Surface Microtopographies on Fouling." Biofouling 20(1): 43-51.

Bixler, G. D., A. Theiss, B. Bhushan and S. C. Lee (2014). "Anti-fouling properties of microstructured surfaces bio-inspired by rice leaves and butterfly wings." Journal of Colloid and Interface Science 419: 114-133.

Callow, J. A. and M. E. Callow (2011). "Trends in the development of environmentally friendly fouling-resistant marine coatings." Nature Communications 2: 244.

Callow, M. E. and J. A. Callow (2000). "Substratum location and zoospore behaviour in the fouling alga Enteromorpha." Biofouling 15(1-3): 49-56.

Carman, M. L., T. G. Estes, A. W. Feinberg, J. F. Schumacher, W. Wilkerson, L. H. Wilson, M. E. Callow, J. A. Callow and A. B. Brennan (2006). "Engineered antifouling microtopographies – correlating wettability with cell attachment." Biofouling 22(1): 11-21.

Cayman. (2015). "Airbus engineers explore shakskin properties for aircraft bodies."

CD-ADAPCO (2017). "User Guide STAR-CCM+, Version 12.06."

Chambers, L. D., K. R. Stokes, F. C. Walsh and R. J. K. Wood (2006). "Modern approaches to marine antifouling coatings." Surface and Coatings Technology 201(6): 3642-3652.

Charnley, M., M. Textor and C. Acikgoz (2011). "Designed polymer structures with antifouling–antimicrobial properties." Reactive and Functional Polymers 71(3): 329-334.

Chen, H., X. Zhang, L. Ma, D. Che, D. Zhang and T. S. Sudarshan (2014). "Investigation on large-area fabrication of vivid shark skin with superior surface functions." Applied Surface Science 316: 124-131.

Chien, K.-Y. (1982). "Predictions of Channel and Boundary-Layer Flows with a Low-Reynolds-Number Turbulence Model." AIAA Journal 20.

Choi, H., P. Moin and J. Kim (1993). "Direct numerical simulation of turbulent flow over riblets." Journal of Fluid Mechanics Vol. 255: pp. 503 - 539.

Choi, K.-S. (1989). "Near-Wall structure of a turbulent boundary layer with riblets." Journal of Fluid Mechanics Vol. 208: pp. 417 - 458.

Choi, K.-S., G. E. Gadd, H. H. Pearcey, A. M. Savill and S. Svensson (1989). "Tests of drag-reducing polymer coated on a riblet surface." Applied Scientific Research Vol. 46: pp. 209 - 216.

Chu, D., R. Henderson and G. Karniadakis (1992). "Parallel spectral-element-fourier simulation of turbulent flow over riblet-mounted surfaces." Theoret. Comput. Fluid Dynamics 3: 219 - 229.

Chu, D. and G. Karniadakis (1993). "A direct numerical simulation of laminar and turbulent flow over riblet-mounted surfaces." J. Fluid Mech. 250: 1 - 42.

Chung, K. K., J. F. Schumacher, E. M. Sampson, R. A. Burne, P. J. Antonelli and A. B. Brennan (2007). "Impact of engineered surface microtopography on biofilm formation of Staphylococcus aureus." Biointerphases 2(2): 89-94.

Coustols, E., C. Gleyzes, V. Schmitt and P. Berrue (1988). Experimental study of reduction of turbulent friction by means of striated walls, nasa

Damodaran, V. B. and N. S. Murthy (2016). "Bio-inspired strategies for designing antifouling biomaterials." Biomaterials Research 20(1): 18.

Dean, B. and B. Bhushan (2010). "Shark-skin surfaces for fluid-drag reduction in turbulent flow: a review." Phil. Trans. R. Soc. A 368: 4775-4806.

Dean, B. R. (1978). "Reynolds number dependence of skin friction and other bulk flow variables in two-dimensional rectangular duct flow." J. Fluids Eng: 215-223.

Deardorff, J. W. (1970). "A numerical study of three-dimensional turbulent channel flow at large Reynolds numbers." J. Fluids Mech 41: 453 - 480.

Demirel, Y. K. (2015). Modelling the roughness effects of marine coatings and biofouling on ship frictional resistance. PhD, University of Strathclyde.

Demirel, Y. K., M. Khorasanchi, O. Turan and A. Incecik (2014). "A CFD model for the frictional resistance prediction of antifouling coatings." Ocean Engineering 89: 21-31.

Demirel, Y. K., O. Turan and A. Incecik (2017). "Predicting the effect of biofouling on ship resistance using CFD." Applied Ocean Research 62: 100-118.

Djenidi, L. and R. A. Antonia (1992). A turbulent low Reynolds number k-epsilon model for riblet flows. 11th Australian Fluid Mechanics Conference. University of Tasmania, Hobart, Australia.

Djenidi, L. and R. A. Antonia (1993). "Riblet flow calculation with a low Reynolds number k-epsilon model." Applied Scientific Research Vol. 50: pp: 267 - 282.

Djenidi, L., L. C. Squire and A. M. Savill (1991). "High resolution conformal mesh computations for V,U or L groove riblets in laminar and turbulent boundary layers." Fluid Mechanics and Its applications Vol. 6: pp. 65-92.

EEA. (2016). "Premature deaths attributable to air pollution." from https://www.eea.europa.eu/media/newsreleases/many-europeans-still-exposed-to-air-pollution-2015/premature-deaths-attributable-to-air-pollution.

El-Samni, O. A., H. H. Chun and H. S. Yoon (2007). "Drag reduction of turbulent flow over thin rectangular riblets." International Journal of Engineering Science 45: 436 - 454.

Endresen, O. (2008). The environmental impacts of increased international maritime shipping. Global forum on transport and environment in a globalising world, Guadalajara, Mexico.

Enyutin, G. V., Y. A. Lashkov, N. V. Samoilova, I. V. Fadeev and E. A. Shumilkina (1987). "Experimental investigation of the effect of longitudinal riblets on the friction drag of a flat plate." Fluid Dynamics 22(2): 284-289.

EPA (2003). "Control of Emissions From New Marine Compression-Ignition Engines at or Above 30 Liters Per Cylinder." US Environmental Protection Agency. Final rule. Federal Register 68(FR 9751).

Ferziger, J. H. and M. Peric (2002). "Computational Methods for Fluid Dynamics."

Fortuna, G. and T. J. Hanratty (1972). "The Influence of Drag-Reducing Polymers on Turbulence in the Viscous Sublayer." Journal of Fluid Mechanics 53: 575-586.

Froude, W. (1872). "Experiments on the surface-friction experienced by a plae moving through water." British Associattion for the Advancement of Science.

Froude, W. (1874). "Report to the Lords Commisioners of the admiralty on Experiments for the Determination of the Frictional Resistance of Water on a Surface, Under Various Conditions, Performed at Chelston Cross, Under the Authority of Their Lordships." 44th Report by the British Association for the Advancement of Science.

Gallagher, J. A. and A. S. W. Thomas (1984). "Turbulent boundary layer characteristics over streamwise grooves " AIAA Journal Vol. 84: pp. 21 - 85.

Ganguli, R., V. Mehrotra and B. Dunn (2009). Bio Inspired Living Skins for Fouling Mitigation.

Gebers, F. (1919). "Das Aehnlichkeitsgesetz bei im Wasser geradlining fortbewegter Platten " Schiffbau 22.

George, S. (2016). "Marin emissions: The IMO says 2020, where do you stand?" A Yokogawa Company.

Goldstein, D. B., R. Handler and L. Sirovich (1995). "Direct numerical simulation of turbulent flow over a modelled riblet covered surface." Journal of Fluid Mechanics Vol. 302: pp. 333 - 376.

Goldstein, D. B. and T. C. Tuan (1998). "Secondary flow induced by riblets."

Granville, P. S. (1958). "The frictional resistance and turbulent boundary layer of rough surfaces." Navy department David taylor model basin Report 1024.

Grass, A. J. (1971). "Structural features of turbulent flow over smooth and rough boundaries." J. Fluid Mech. 50.

Guo, R. and F. Zhou (2013). Superhydrophobic Surfaces for Drag Reduction. Encyclopedia of Tribology. Q. J. Wang and Y.-W. Chung. Boston, MA, Springer US: 3380-3387.

Hama, F. (1956). "Some current problems in turbulent shear flows." Symposium on Naval Hydrodynamics.

Hinze, J. O. (1975). "Turbulence " McGraw-Hill.

Hooshmand, A. (1985). "An Experimental Investigation of the Influence of a Drag Reducing, Longitudinally Aligned, Triangular Riblet Surface on the Velocity and Streamwise Vorticity Fields of a Zero-Pressure Gradient Turbulent Boundary Layer." Ph.D. DIssertation, University of Maryland, College Park, MD.

Hooshmand, D., R. Youngs and J. M. Wallace (1983). "An experimental study of changes in the structure of a turbulent boundary layer due to surface geometry changes " AIAA Journal Vol. 83: pp. 02-30.

Horsten, B. J. C. (2005). "A numerical study on laminar and turbulent flow over sharp and blunt sawtooth riblets." Delft University of Technology.

ICS. (2018). "Shipping and World Trade." International Chamber of Shipping, from http://www.ics-shipping.org/shipping-facts/shipping-and-world-trade.

IMO. (2002). "Focus on IMO: Antifouling systems." from http://www.imo.org/en/OurWork/Environment/Anti-foulingSystems/Pages/Default.aspx.

IMO (2012). "2012 Guidelines for the development of a Ship Energy Efficiency Management Plan (SEEMP)." Annex 9, Resolution MEPC.213(63).

IMO (2014). "Third IMO Greenhouse Gas Study 2014." International Maritime Organisation.

IMO. (2018). "Our Work - Marine Environment." from http://www.imo.org/en/OurWork/.

Jimenez, J. and P. Moin (1991). "The minimal flow unit in near-wall turbulence." Journal of Fluid Mechanics 225: 213-240.

Johnson, C. S. (1970). "Some Hydrodynamic Measurements on Sharks." Scipps Institution of Oceanograpy, Lajolla, CA NUC TP-189.

Kempf, G. (1929). "Results obtained in measuring frictional resistance." Trans INA 79: 109-119.

Kesel, A. and R. Liedert (2007). Learning from Nature: Non-Toxic Biofouling Control by Shark Skin Effect.

Khan, M. M. S. (1986). "A numerical investigation of the drag reduction by riblet surfaces " AIAA Journal Vol. 86: pp. 11-27.

Kiil, S., C. E. Weinell, M. S. Pedersen and K. Dam-Johansen (2001). "Analysis of Self-Polishing Antifouling Paints Using Rotary Experiments and Mathematical Modeling." Industrial & Engineering Chemistry Research 40(18): 3906-3920.

Kim, H. T., S. J. Kline and W. C. Reynolds (1971). "The Production of Turbulence Near a Smooth Wall in a Turbulent Boundary Layer." Fluid Mechanics 50: 133-160.

Kim, J., P. Moin and R. Moser (1987). "Turbulence statistics in fully developed channel flow at low Reynolds number." Journal of Fluid Mechanics Vol. 177.

Kirschner, C. M. and A. B. Brennan (2012). "Bio-Inspired Antifouling Strategies." Annual Review of Materials Research 42(1): 211-229.

Klebanoff, P. S. (1954). "Characteristics of turbulence in a boundary layer with zero pressure gradient." NACA TN 3178.

Kline, S. J., W. C. Reynolds, F. A. Schraub and P. W. Runstadler (1967). "The structure of turbulent boundary layers." Fluid Mechanics 30(741-773).

Kline, S. J. and P. W. Runstadler (1959). "Some preliminary results of visual studies of the flow model of the wall layers of the turbulent boundary layer." Journal of Applied Mechanics: pp. 166 - 170.

Kolmogorov, A. (1941). "The local structure of turbulence in incompressible viscous fluids at very large Reynolds numbers." Doklady AN SSSR 30: 299-303.

Kramer, M. (1937). "Device for Reducing the Frictional Resistance." German Patent No.669897.

Kramer, M. (1961). "The Dolphin's Secret." Naval Engineers Journal 73(1): 103-108.

Kugel, A., S. Stafslien and B. J. Chisholm (2011). "Antimicrobial coatings produced by “tethering” biocides to the coating matrix: A comprehensive review." Progress in Organic Coatings 72(3): 222-252.

Lang, A., P. Motta, P. Hidalgo and M. Westcott (2008). "Bristled shark skin: a microgeometry for boundary layer control ?" Bioinspiration & Biomimetics 3.

Laufer, J. (1953). "The structure of turbulence in fully developed pipe flow." NACA Report 1174.

Launder, B. E. and S. Li (1993). "On the prediction of riblet performance with engineering turbulence models." Applied Scientific Research Vol. 50 pp: 283 - 298.

Launder, B. E. and B. I. Sharma (1974). "Application of the energy-dissipation model of turbulence to the calculation of flow near a spinning disc." Letters in Heat and Mass Transfer.

Launder, B. E. and D. P. Tselepidakis (1990). "Contribution to the Secon-Moment Modelling of Sublayer Turbulent Transport." In Near-Wall Turbulence, S.J. Kline and N.H. Afgan, eds., Hemisphere, New York, 818-833.

Li, S.-P. (1992). "PhD Thesis." Faculty of Technology, University of Manchester.

Liu, K., C. Christodoulou, O. Riccius and J. D. D. (1990). "Drag reduction in pipes lined with riblets." AIAA Journal 28(10).

Long, C. J., J. F. Schumacher, P. A. C. Robinson, J. A. Finlay, M. E. Callow, J. A. Callow and A. B. Brennan (2010). "A model that predicts the attachment behavior of Ulva linza zoospores on surface topography." Biofouling 26(4): 411-419.

Magin, C., S. Cooper and A. Brennan (2010). "Non-toxic antifouling strategies." Materialstoday 13(4): 36-44.

Martin, R. (2018) "ARCHIE WeSt Training."

Martin, S. G. (2013). "Fluid flow modelling of biomimetic structures."

Mohsen Jahanmiri and A. Bahraini (2015). "Large eddy simulation of turbulent drag reduction by V-shaped riblets." International Journal of Latest Research in Science and Technology Vol. 4(Issue 1): pp: 42 - 46.

Moin, P. and J. Kim (1982). "Numerical investigation of turbulent channel flow." J. Fluid Mech. 118: 341 - 377.

Moin, P., W. C. Reynolds and J. H. Ferziger (1978). "Large eddy simulation of incompressible turbulent channel flow." Dept Mech. Engng, Stanford University, Rep. TF-12.

Nikuradse, J. (1950). "Laws of flow in rough pipes." NACA TM1291.

Oliveira, D. and L. Granhag (2016). "Matching Forces Applied in Underwater Hull Cleaning with Adhesion Strength of Marine Organisms." Journal of Marine Science and Engineering 4(4): 66.

Olmer, N., B. Comer, B. Roy, X. Mao and D. Rutherford (2017). "Greenhouse gas emissions from global shipping, 2013–2015." The International Council on Clean Transportation (ICCT).

Olsen, S. M., L. T. Pedersen, M. H. Laursen, S. Kiil and K. Dam-Johansen (2007). "Enzyme-based antifouling coatings: a review." Biofouling 23(5): 369-383.

Pablo, E. D. (2013). "Analysis of the shear stress distributions on two ship hull form." Technical University of Denmark, Nordic Master in Maritime Engineering.

Papanikolaou, A. (2014). Ship Design - Methodologies of Preliminary Design.

Peng, Y. L., C. G. Lin and L. Wang (2009). "The Preliminary Study on Antifouling Mechanism of Shark Skin." Advanced Materials Research 79-82: 977-980.

Perlin, M., D. R. Dowling and S. L. Ceccio (2016). Freeman Scholar Review: Passive and Active Skin Friction Drag Reduction in Turbulent Boundary Layers.

Pope, S. B. (2000). "Turbulent flows." Cambridge University Press.

Prandtl, L. (1921). "Ergebnisse der Aerodynamischen Versuchsanstalt zu Goettingen." Abhandlungen aus dem Aerodynmischen Institut, Aachen.

Prandtl, L. (1927). "Ergebnisse der Aerodynamischen Versuchsanstalt zu Goettingen, III Lieferung."

Prandtl, L. (1932). "Ergebnisse der Aerodynamischen Versuchsanstalt zu Goettingen, IV Lieferung."

Pu, X., G. Li and H. Huang (2016). "Preparation, anti-biofouling and drag-reduction properties of a biomimetic shark skin surface." Biology Open.

Pulles, C. J. A. (1988). "Drag reduction of turbulent boundary layer by means of grooved surfaces." Ph.D. Thesis, Eindhov University of Technology, The Netherlands.

Raschi, W. and J. Elsom (1986). "Comments on the Structure and Development of the Drag Reduction Type Placoid Scale." Proceedings of the Second International Conference on Indo-Pacific Fishes: 408-424.

Raschi, W. and J. A. Musick (1984). "Hydrodynamic Aspects of Shark Scales." Virgina Inst. of Marine Science, Rept. SRAMSOE 272: 1-82.

Reidy, L. W. (1987). "Flat plate drag reduction in a water tunnel using riblets." Naval Ocean Systems Center with the Independent Research Program.

Reif, W.-E. (1978). "Protective and hydrodynamic function of the dermal skeleton of elamolranshs." Neues Hahrbuch fuer Geologie und Palaeontologie Vol. 157: pp. 133 - 141.

Reif, W.-E. (1982). "Morphogenesis and functions of the squamation in sharks." Neues Hahrbuch fuer Geologie und Palaeontologie Vol. 164: pp. 172 - 183.

Reif, W.-E. and A. Dinkelacker (1982). "Hydrodynamics of the squamation in fast swimming sharks." Neues Hahrbuch fuer Geologie und Palaeontologie Vol. 164: pp. 184 - 187.

Robinson, S. K. (1991). "The kinematics of turbulent boundary layer structure." NASA Technical Memorandum 103859.

Saeedipour, M., S. Schneiderbauer, S. Pirker and S. Bozorgi (2014). Numerical simulation of turbulent liquid jet breakup using a sub-grid criterion with industrial application. ILASS - Europe 2014, 26th Annual Conference on Liquid Atomization and Spray Systems. Bremen, Germany.

Savill, A. M. (1986). "Effects of turbulent boundary layer structure of longitudinal riblets alone and in combination with outer layer devices." Paper presented at the fourth international symposium on flow visualization, Paris.

Sawyer, W. G. and K. G. Winter (1987). "An investigation of the effect on turbulent skin friction of surfaces with streamwise grooves." Paper presented at the turbulent drag reduction by passive means conference.

Scardino, A. J., E. Harvey and R. De Nys (2006). "Testing attachment point theory: diatom attachment on microtextured polyimide biomimics." Biofouling 22(1): 55-60.

Schoenherr, K. E. (1932). "Resistance of flat surfaces moving through a fluid." Transaction of SNAME 40: 279-313.

Schumacher, J. F., N. Aldred, M. E. Callow, J. A. Finlay, J. A. Callow, A. S. Clare and A. B. Brennan (2007). "Species-specific engineered antifouling topographies: correlations between the settlement of algal zoospores and barnacle cyprids." Biofouling 23(5): 307-317.

Schumacher, J. F., C. J. Long, M. E. Callow, J. A. Finlay, J. A. Callow and A. B. Brennan (2008). "Engineered Nanoforce Gradients for Inhibition of Settlement (Attachment) of Swimming Algal Spores." Langmuir 24(9): 4931-4937.

Schumann, U. (1975). "Subgrid scale model for finite difference simulations of turbulent flows in plane channels and annuli." J. Comp. Phys. 18: 376 - 404.

Sharklet. (2018). "Inspired by Nature." from https://www.sharklet.com/our-technology/technology-overview/.

Tezdogan, T., Y. K. Demirel, P. Kellett, M. Khorasanchi, A. Incecik and O. Turan (2015). "Full-scale unsteady RANS CFD simulations of ship behaviour and performance in head seas due to slow steaming." Ocean Engineering 97: 186-206.

Toms, B. A. (1949). "Some observations on the flow of linear polymer solutions through straight tubes at large Reynolds numbers." Proc. of the International Congress on Rheology: 135-141.

UNCTAD (2018). "Review of maritime transport 2018." United Nations Conference on Trade and Development.

USNA. (2018). "Resistance and powering of ships." from www.usna.edu/NAME.

Von Karman, T. (1930). "Mechanical similitude and turbulence." Tech. Mem. NACA 5: 58-76.

Wallace, J. M. (1983). " Experimental studies of the structural changes of the turbulent boundary layer due to surface geometry changes " Paper presented at the Drag Reduction Symposium, National Academy of Sciences, Washington, DC.

Walsh, M. J. (1980). "Drag Characteristics of V-groove and Transverse Curvature Riblets." AIAA Journal.

Walsh, M. J. (1982). "Turbulent Boundary Layer Drag Reduction Using Riblets."

Walsh, M. J. (1983). "Riblets as a Viscous Drag Reduction Technique." AIAA Journal 21.

Walsh, M. J. (1990). "Viscous drag reduction in boundary layers." AIAA Journal Vol. 123: pp. 203-261.

Walsh, M. J. and A. M. Lindemann (1984). "Optimization and application of riblets for turbulent drag reduction." AIAA Journal 84.

Walsh, M. J. and L. M. Weinstein (1979). "Drag and heat transfer characteristics of small longitudinally ribbed surface." AIAA Journal 17(7).

Webb, P. W. (1975). "Hydrodynamics and energetics of fish propulsion." Bull. Fish. Res. Bd. Can. 190: 1-159.

Wilkinson S. P. and B. S. Lazos (1988). "Direct drag and hot-wire measurements on thin-element riblet arrays." Turbulence management and relaminarization: Symposium: pp: 121 - 131.

Won, S. (2013). "What is the mystery of turbulence?".

Yulia Peet, Pierre Sagaut and Y. Charron (2007). "Towards large eddy simulations of turbulent drag reduction using sinusoidal riblets."

Research Output

The following publications were generated throughout the timespan of PhD studies related to this thesis.

Journal paper (SCI)

1. **Zhang, Y.**, Turan, O. (2019) CFD investigation on the drag-reduction performance of a new micro-patterned surface, Ocean Engineering, in preparation
2. **Zhang, Y.**, Turan, O. (2019) Predicting the effect of coating on ship resistance, Ocean Engineering, in preparation
3. Demirel, Y. K., Uzun D., **Zhang, Y.**, Fang, H.C., Day, A., Turan, O., 2017. Effect of barnacle fouling on ship resistance and powering. Biofouling, 33(10): 819-834.

Conference papers:

1. **Zhang, Y.**, Turan, O. (2018) CFD investigation on the drag-reduction performance of a new micro-patterned surface. The 4th International Symposium on Ocean Science and Technology. Glasgow: University of Strathclyde.
2. **Zhang, Y.**, Turan, O. (2017) Numerical investigation of shark skin inspired riblet drag-reduction structure. The 27th International Ocean and Polar Engineering Conference. San Francisco, California, USA, International Society of Offshore and Polar Engineers: 7.
3. Uzun, D., **Zhang, Y.**, Demirel, Y. K., & Turan, O. (2017) Experimental determination of added resistance due to barnacle fouling on ships by using 3D printed barnacles. The 5th International Conference on Advanced Model Measurement Technology for the Maritime Industry (AMT'17) (pp. 262-277). Glasgow: University of Strathclyde.